Gas Turbine Laboratory
Department of Aeronautics and Astronautics
Massachusetts Institute of Technology
Cambridge, MA 02139-4307

A Final Technical Report

for research supported under NASA Grant #NAG3-2051

entitled

THREE-DIMENSIONAL AERODYNAMIC INSTABILITIES IN MULTI-STAGE AXIAL COMPRESSORS

submitted to

NASA Glenn Research Center
21000 Brookpark Avenue
Cleveland, OH 44135

Attn: Kenneth L. Suder, Ph.D., Program Manager

INVESTIGATORS: Choon S. Tan, Ph.D.
Senior Research Engineer

Yifang Gong, Ph.D.
Graduate Research Assistant

March 2001

EXCUTIVE SUMMARY

This document constitutes a final report on NASA GRC Grant No. NAG3-2051. It consists of two parts. Part I documents the work and results on " A Computational Model for Rotating Stall and Inlet Distortions in Multistage Compressors" which was Y. Gong's doctoral dissertation. A computational model for simulating axial compressor stall inception and development via disturbances with length scales on the order of several (typically about three) blade pitches have been developed and this was described in Part I of the report. The model was designed for multi-stage compressors in which stall is initiated by these ``short wavelength" disturbances, also referred to as spikes. The inception process described is fundamentally nonlinear, in contrast to the essentially linear behavior seen in so-called ``modal stall inception". Each blade-row was represented by a body force distribution evaluated in real time using the blade-row characteristics and local flow conditions. The model was able to capture the following experimentally observed phenomena: (1) development of rotating stall via short wavelength disturbances, (2) formation and evolution of localized short wavelength stall cells in the first stage of a mismatched compressor, (3) the switch from long to short wavelength stall inception resulting from the re-staggering of the inlet guide vane, (4) the occurrence of rotating stall inception on the negatively sloped portion of the compressor characteristic. Parametric investigations indicated that (1) short wavelength disturbances were supported by the rotor blade row, (2) the disturbance strength was attenuated within the stators, and (3) the reduction of inter-blade row gaps can suppress the growth of short wavelength disturbances. It is argued that each local component group (rotor plus neighboring stators) has its own instability point (i.e. conditions at which disturbances are sustained) for short wavelength disturbances, with the instability point for the compressor set by the most unstable component group. However there remain two issues that need to be re-examined. First the use of the computational model for simulating axial compressor instability requires the specification of compressor pressure rise characteristics including the portion of the characteristics to the left of the peak of pressure rise characteristics. This is the portion of the characteristics that one would measure if the compressor were prevented from stall for operating points past the peak. As such this information is not readily available. Thus it would be of engineering

interest to assess the sensitivity of the stall inception process and its subsequent development to the portion of the pressure rise characteristics that is to the left of the peak. Second only a rudimentary procedure used for representing each blade-row as a body force distribution that was evaluated in real time using the blade-row characteristics and local flow conditions. Thus there is also a need to develop a procedure whereby the body force representation of a blade row can be implemented directly using the best available CFD solution of isolated single blade passage. Part II of the report addresses two issues and the initial development of a rational procedure for obtaining a body force representation of blade row.

THREE-DIMENSIONAL AERODYNAMIC INSTABILITIES IN MULTISTAGE AXIAL COMPRESSORS

Part I: A Computational Model for Rotating Stall and Inlet Distortions in Multistage Compressors

Abstract

This thesis presents the conceptualization and development of a computational model for describing three-dimensional non-linear disturbances associated with instability and inlet distortion in multistage compressors. Specifically, the model is aimed at simulating the non-linear aspects of short wavelength stall inception, part span stall cells, and compressor response to three-dimensional inlet distortions. The computed results demonstrated the first-of-a-kind capability for simulating short wavelength stall inception in multistage compressors.

The adequacy of the model is demonstrated by its application to reproduce the following phenomena: (1) response of a compressor to a square-wave total pressure inlet distortion; (2) behavior of long wavelength small amplitude disturbances in compressors; (3) short wavelength stall inception in a multistage compressor and the occurrence of rotating stall inception on the negatively sloped portion of the compressor characteristic; (4) progressive stalling behavior in the first stage in a mismatched multistage compressor; (5) change of stall inception type (from modal to spike and vice versa) due to IGV stagger angle variation, and "unique rotor tip incidence" at these points where the compressor stalls through short wavelength disturbances. The model has been applied to determine the parametric dependence of instability inception behavior in terms of amplitude and spatial distribution of initial disturbance, and intra-blade-row gaps. It is found that reducing the inter-blade row gaps suppresses the growth of short wavelength disturbances. It is also concluded from these parametric investigations that each local component group (rotor and its two adjacent stators) has its own instability point (i.e. conditions at which disturbances are sustained) for short wavelength disturbances, with the instability point for the compressor set by the most unstable component group.

For completeness, the methodology has been extended to describe finite amplitude disturbances in high-speed compressors. Results are presented for the response of a transonic compressor subjected to inlet distortions.

Contents

List of Figures

List of Tables

Chapter 1

Introduction

1.1 Introduction

Compressor instability is a major limiting factor on gas turbine engine operating range, performance, and reliability. The instability, either in a form known as rotating stall or surge, occurs at an operating point with low mass flow and high pressure rise. To avoid such instabilities, the compressor (and hence the engine) has to operate at an operating point corresponding to lower pressure ratio so that an adequate stall margin is maintained (Fig. 1.1). The stall margin can be considerably reduced in operating environments for which the inlet conditions are non-uniform.

Recent experimental data [9, 60] have elucidated the importance of three-dimensional and non-linear aspects of compressor flow instability behavior which are beyond the scope of current flow models. The work described in this thesis constitutes a research which addresses these aspects. The effort is focused first on developing a computational model to delineate compressor instabilities in multistage compressor under uniform as well as non-uniform flow situations, followed by its preliminary applications to establish causal links between instability behavior and compressor design characteristics.

In this chapter, phenomena associated with compressor instability, including short wavelength stall inception in multistage compressors [9], are reviewed. This is then followed by a review of the current modeling capability. The objectives and

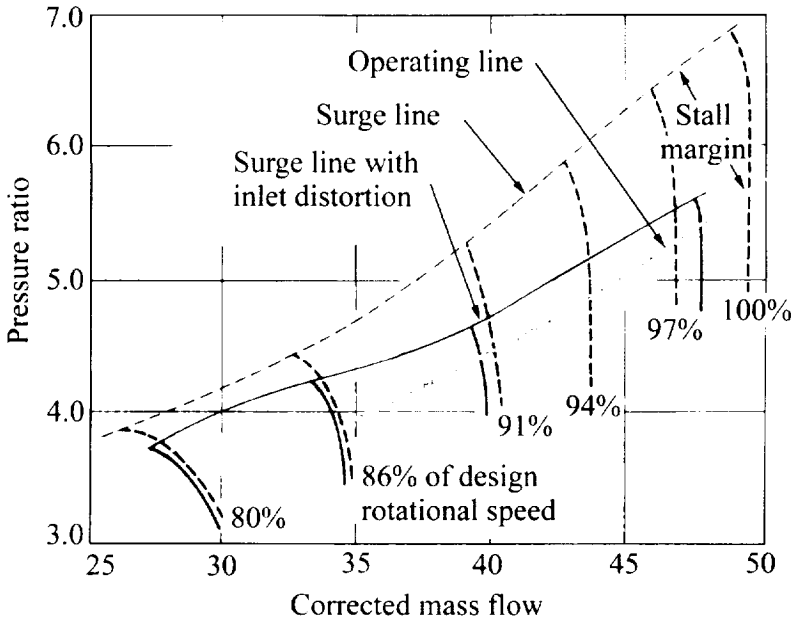

Figure 1.1: Compressor performance map and the effects of inlet distortions [57].

scope of the thesis are described, followed by a concise delineation of the contributions.

1.2 Overview of Compressor Instabilities

1.2.1 Types of compressor instability in axial compressors

Three types of instability behavior have been observed at compressor operating points beyond the surge line (Fig. 1.2), which are progressive stall, 'abrupt' stall, and surge.

With progressive stall, there is a gradual deterioration of pressure rise. This happens for example when a multistage compressor is operated at a speed below the design speed. The flow field associated with this type of instability is illustrated in Fig. 1.3(a) which shows several part-span stall cells rotating around the annulus. This flow pattern usually occurs in one or several stages in a multistage compressor.

'Abrupt' stall shows a sudden drop of pressure rise at the compressor surge line, with the formation of a full span stall cell (Fig. 1.3(b)). The stall cell has an axial

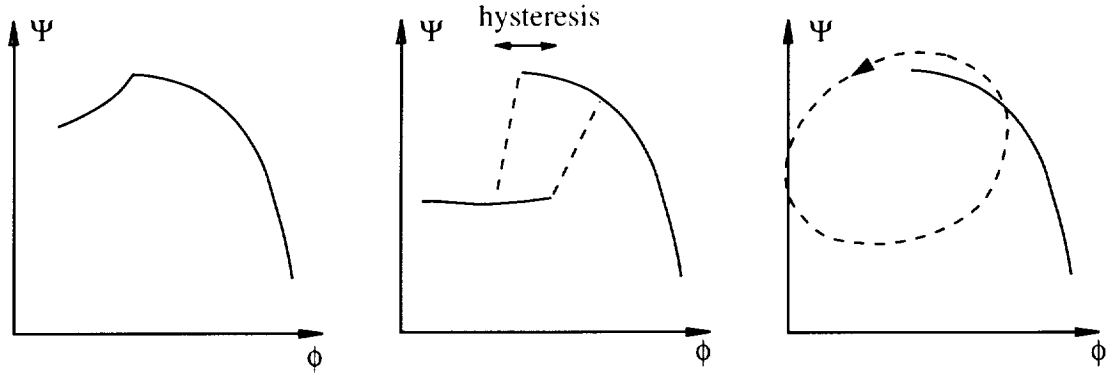

a) progressive stall b) 'abrupt' stall c) surge

Figure 1.2: Three types of compressor instability characterized in terms of the respective pressure rise characteristics.

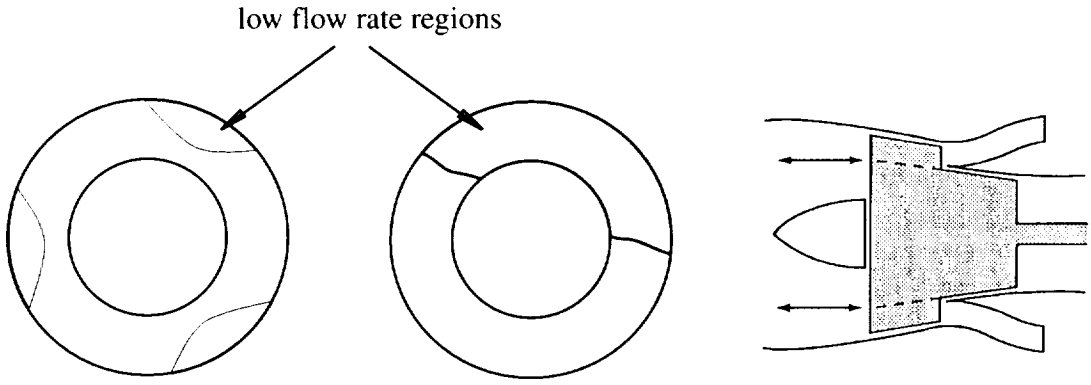

a) part span stall cells b) full span stall cell c) surge

Figure 1.3: Three typical instability patterns in compression systems.

extent that encompasses the whole compressor; this explains the large drop of pressure rise (in contrast to the situation in the part-span stall cell pattern). To recover from this type of stall pattern, the throttle has to be moved to a position corresponding to a flow coefficient (or corrected mass flow) much larger than that at which the compressor would stall upon throttle closing. This effect is usually referred to as hysteresis, shown in Fig. 1.2(b).

Surge is a one-dimensional flow oscillation through the whole engine (Fig. 1.3(c)). During an engine surge, a flame can often be seen at the intake and exhaust as the combustion moves forward and backward from the combustor.

1.2.2 Onset of instability

Predicting the condition at which instability will occur in a compressor requires an understanding of the flow processes leading to the onset of the instability. The phenomena described in the previous subsection are the final forms of instability. And it is important to distinguish the final form from the onset of instability. The transition from initial disturbance to final stall or surge can usefully be divided into three stages (1) inception; (2) development; and (3) final flow pattern. The inception stage is the period when disturbances start to grow (flow becomes unstable). It defines the operating point and conditions for which instability occurs. In practice, the disturbances will take a finite amount of time (ranging from a few to several hundred rotor revolutions) to grow into final stall or surge, so that the inception stage can be viewed as the early development of the unstable flow.

For some compressors, the inception stage consists of the linear growth (extending up to several hundred rotor revolutions) of disturbances of infinitesimal amplitude, while in others the inception stage only extends over one to two rotor revolutions after its detection. The inception stage is the major focus of the instability modeling and prediction.

The development stage, which includes all the processes after the inception stage before the final flow pattern to be reached, is usually of less importance. It is often the case that one final form of instability in one compressor could be the pre-stage of

the final form in another compressor. For example, rotating stall might cause surge in some compressors, as noted by Greitzer [26]:

> The global (system) instability is a basically one-dimensional phenomenon, involving on overall, annulus averaged, compressor performance curve. For typical volumes, lengths, and throttle characteristics this must generally be slightly positive sloped for system instability to occur. We have also seen that the axisymmetric flow through a compressor can be unstable to two- (or three-) dimensional infinitesimal disturbances, and that this local instability marks the inception of rotating stall. However, the onset of this rotating stall is very often associated with a precipitous drop in the overall ("one-dimensional") pressure-rise mass-flow curve of compressor performance. In other words, the inception of rotating stall can lead to a situation where the instantaneous compressor operating point is on a steeply positively sloped part of the characteristic, with a consequent violation of the dynamic and/or the static instability criteria.

In this sense, part span stall could be the pre-stage of full span rotating stall. This aspect will further be elaborated in Section 5.6.

1.2.3 Two Major Stall Inception Types

Two major inception types have been experimentally identified: modal waves, and spikes. Modal waves are exponentially growing long wavelength (length scale comparable to the annulus) small amplitude disturbances. The rotating speed of this type of disturbance is in the range between 20% to 50% of rotor speed. Figure 1.4 shows velocity traces during the transition process from small amplitude pre-stall waves (modal waves) to the fully developed stall pattern. Modal waves penetrate the whole compressor in the axial direction, so they can be detected by sensors at any locations at the inlet, exit, or within the compressor. Usually, this type of stall inception occurs at a point near the peak of the characteristic. This type of inception can be well described by linear stability theory. The theory developed by Moore and Greitzer [51]

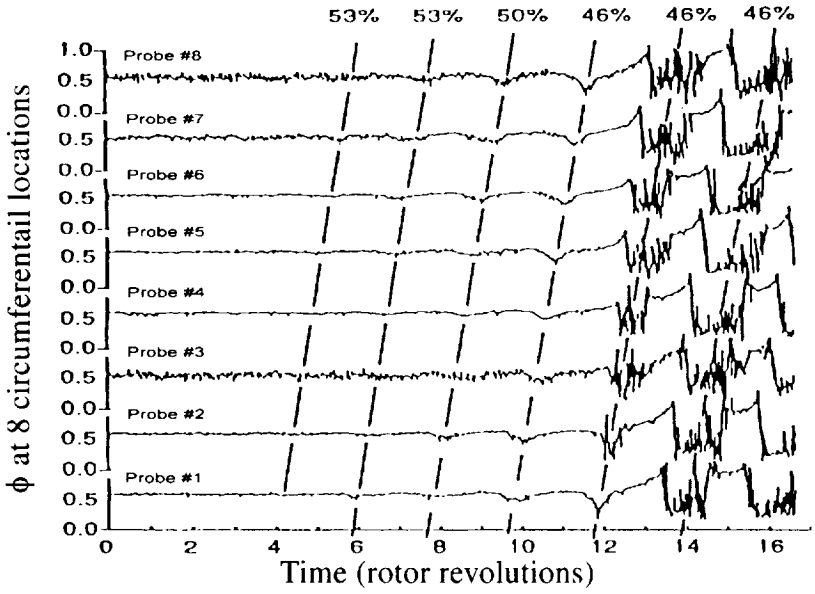

Figure 1.4: Velocity traces of eight sensors on the annulus show a typical stall inception through modal waves [45].

predicted the pre-stall modal wave before measurements were taken [49, 23].

The other inception mechanism is the growth of localized non-linear short wavelength (with length scale of several blade pitches) disturbances [9], often referred to as "spikes". This type of stall inception is referred to as "short wavelength stall inception". Figure 1.5 shows velocity traces during a compressor stalling through short wavelength disturbances. The inception starts as one or several spike-shaped finite amplitude disturbances within the tip region of a particular stage. Usually, the disturbance develops into a large full span stall cell within three to five rotor revolutions. The initial rotating speed of this type of disturbances is around 70% of rotor speed, substantially higher than that for the typical modal wave speed. No existing model has been demonstrated to be capable of describing this type of phenomenon. The lack of this capability motivates this research project.

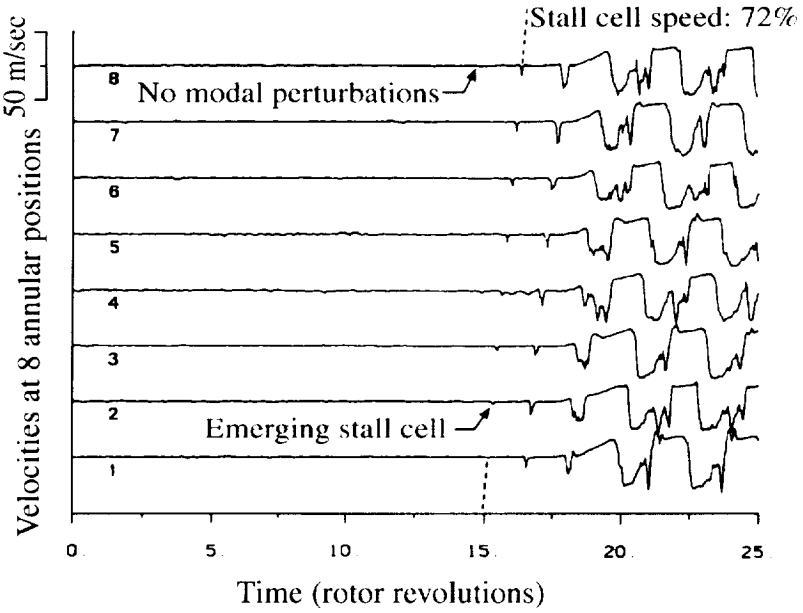

Figure 1.5: Velocity traces of eight sensors on the annulus show the compressor stall inception through short wavelength disturbances (spikes) [9].

1.3 Experimental Observations on Short Wavelength Stall Inception

The experimental observations associated with short wavelength stall inception are summarized in this section.

1.3.1 Features of Short Wavelength Stall Inception

Short wavelength stall inception first was identified by Day [9], but it has since been observed in many compressors [11, 17]. So far, the phenomena have only been roughly defined in a descriptive manner. From experimental observations [9, 11, 17, 60], a short wavelength type of stall inception is initiated by one or several disturbances which are localized in the tip region of a specific stage in a multistage compressor. Its circumferential width is about 2-3 blade pitches, with a high rotating speed (70% rotor speed), as well as a high growth rate (it takes 3-5 rotor revolutions from emerging of initial disturbance to forming a large stall cell) relative to the modal wave type of

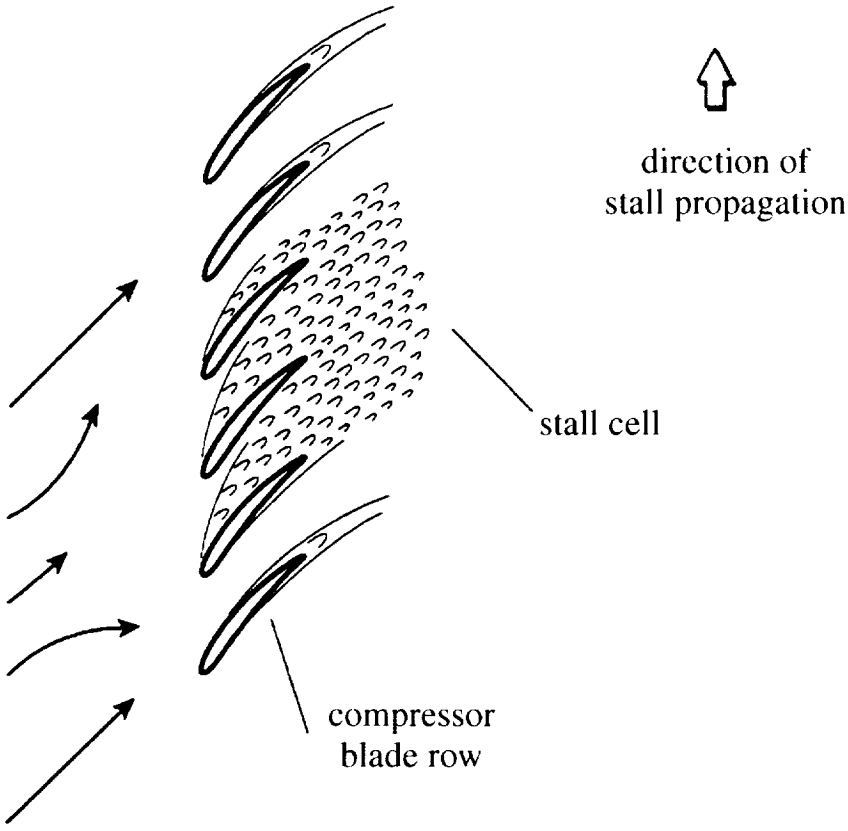

Figure 1.6: Emmons's rotating stall cell propagation mechanism.

stall inception.

Day conjectured that the inception is initiated by blade passage events (analogous to the argument offered by Emmons [15] and shown in Fig.1.6).

1.3.2 Experiments on Compressor Response to Rotating Inlet Distortions

Longley et al [44] investigated the effects of rotating inlet distortions on compressor stability in several compressors, and found that there are two types of compressor response (measured in terms of the stall margin vs. rotating speed of the distortion): one shows a single resonance peak corresponding to a large decrement in stall margin when inlet distortion is rotating at around 0.4 rotor speed in the direction of rotor

rotation (Fig. 1.7(a)); the other shows two resonance peaks at 0.3 rotor speed as well as at 0.75 rotor speed (Fig. 1.7(b)). The compressors which show one resonance peak stall through modal waves while the other exhibit the spike type of stall inception. Thus the respective characteristic response of the compressor corresponds to two types of observed stall inception mechanisms which have different impact on stall margin due to rotating inlet disturbances.

1.3.3 Relation Between Local Stall Cells in Mismatched Compressor and Stall Inception through Short Wavelength Scale Disturbances

An interesting experiment has been conducted on a mismatched four-stage low speed compressor with the rotors in the latter three stages deliberately re-staggered away from stall [60]. The type of stall inception of the compressor in a matched build (i.e. four identical stage configuration) was spike type.

Measurements show that upon reducing the flow coefficient, the first stage still stalls at about the same flow coefficient as in the matched build (Fig. 1.8). The pressure rise then reduces gradually as the flow coefficient is decreased, similar to the progressive stall characteristic shown in Fig. 1.2(a). The stall cells are localized to the first stage. It is hypothesized that the influence of downstream stable stages limits the extent of stall cell.

The extent of these stall cells has the same order as that of spikes associated with the short wavelength stall inception. The rotational speed is the same as that of spikes. The similarity between the local stall cells, which are in its equilibrium state, and the spikes, which are in transition, indicates a link between the two phenomena. Therefore, the resulting knowledge from examining these local stall cells can be of utility in assessing the observations on short wavelength stall inception.

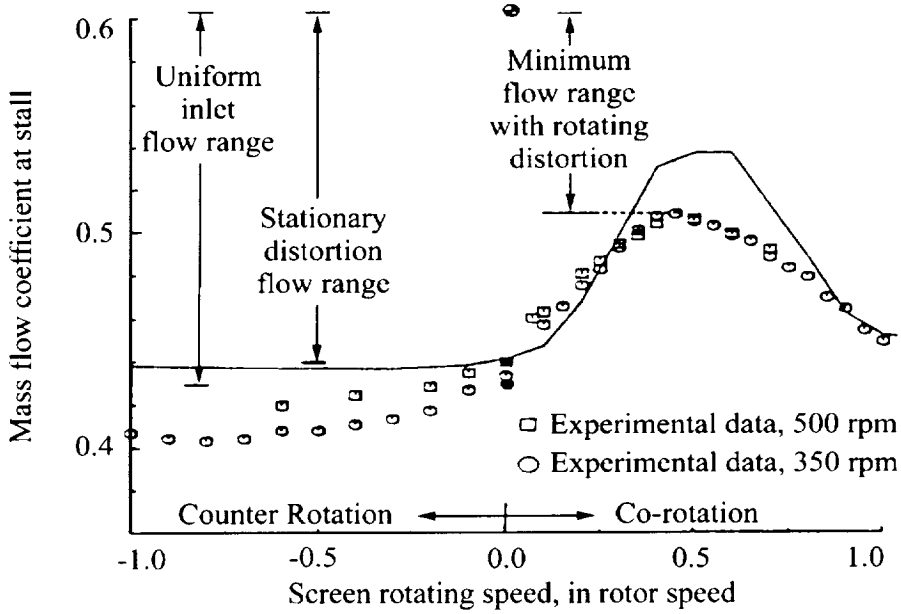

(a) Single resonance peak

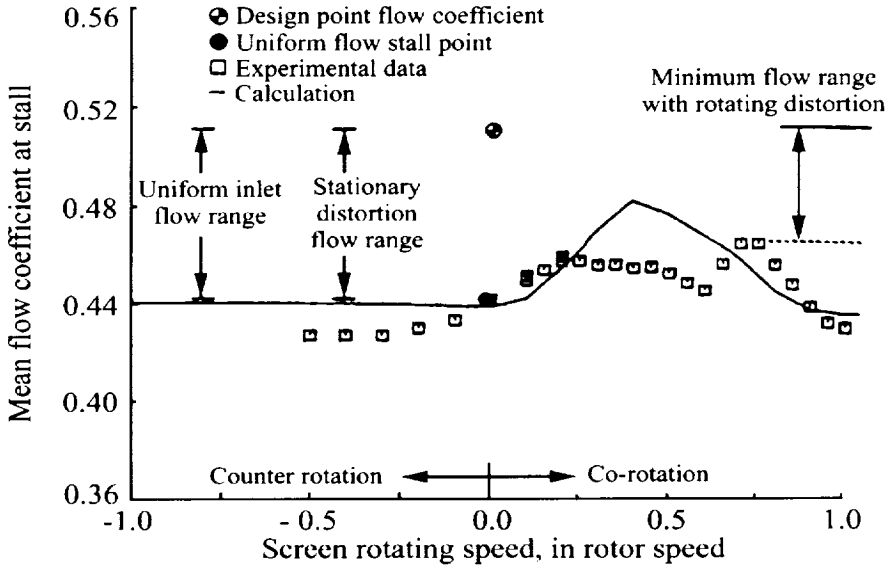

(b) Two resonance peaks

Figure 1.7: Two types of compressor resonance response to rotating inlet distortions.

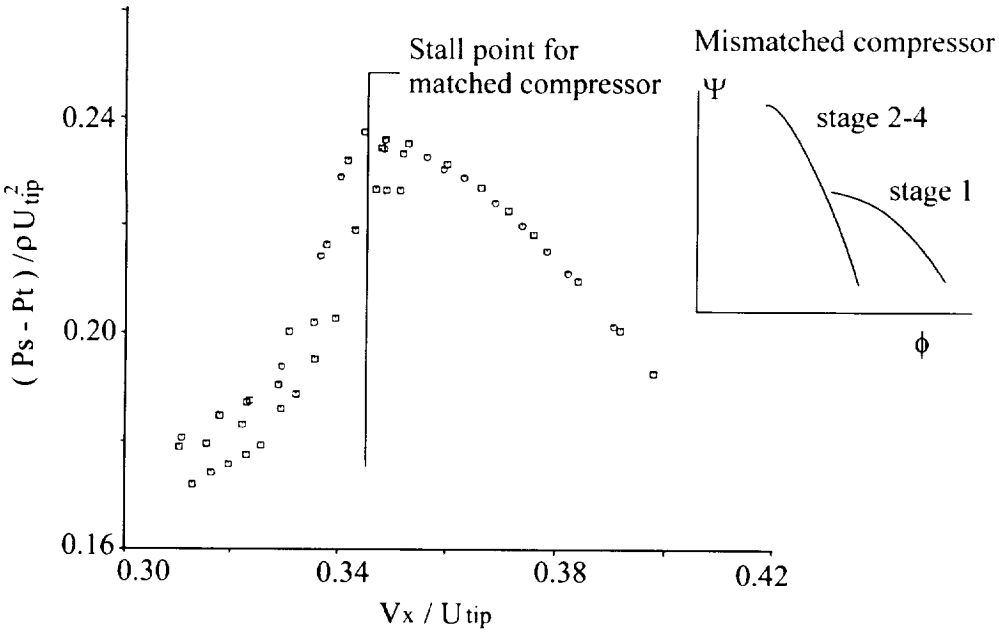

Figure 1.8: First stage pressure rise characteristic of the GE mismatched compressor [60].

1.3.4 Existence of Short Length Disturbances Prior to Stall Point

Using a correlation method to analyze the measurements during the stall inception of the GE compressor, Park [56] found that spike-shaped disturbances existed prior to stall. He observed the short wavelength disturbances hundreds of rotor revolutions before the actual stalling event occurs (Fig. 1.9). These disturbances were seen to form and decay until stalling of the compressor takes place (Fig. 1.10 and Fig. 1.11). The frequency of the forming-decaying activity increased as the instability was approached through throttle closing.

One implication of his work is that the short wavelength stall inception can be initiated by existing localized non-linear disturbances. This finding is not in accord with linear theory, which is based on the growth of infinitesimal disturbances.

Park also sought the best sensor location for the detection of short wavelength stall inception. He found that static pressure sensors at the first rotor exit showed the

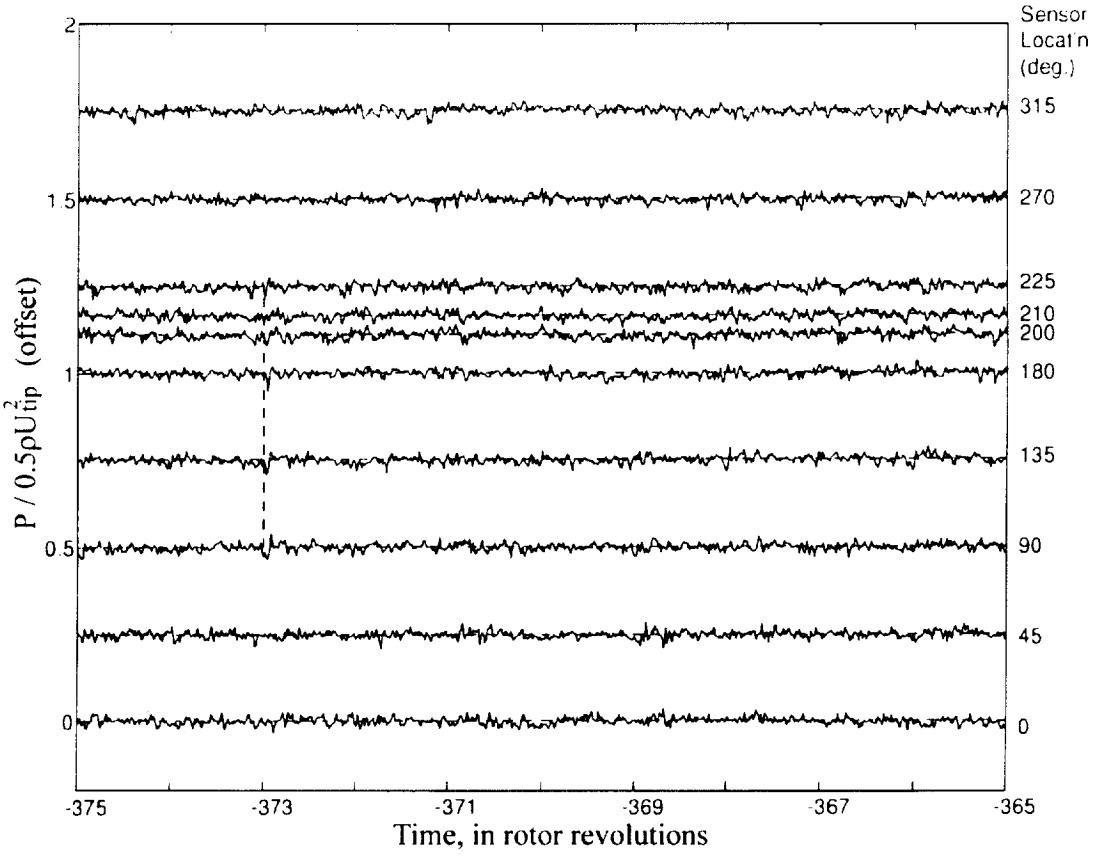

Figure 1.9: Spike disturbances form and decay before stall (at time = 0). The pressure traces, from sensors at different circumferential positions at the first rotor exit, are shifted relative to first trace so that disturbances traveling at 71% of rotor speed line up vertically. Guide lines identify propagating spikes. [56]

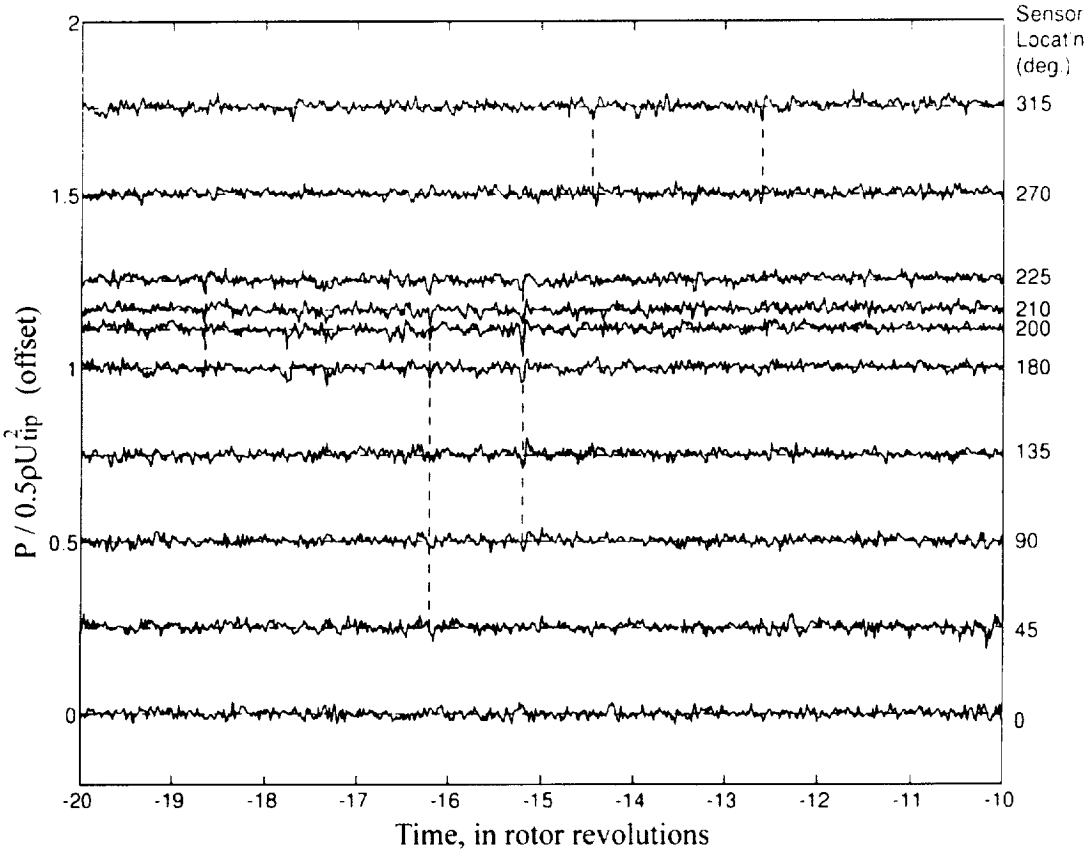

Figure 1.10: Spike disturbances form and decay near stall (at time = 0). The pressure traces, from sensors at different circumferential positions at the first rotor exit, are shifted relative to first trace so that disturbances traveling at 71% of rotor speed line up vertically. Guide lines identify propagating spikes. [56]

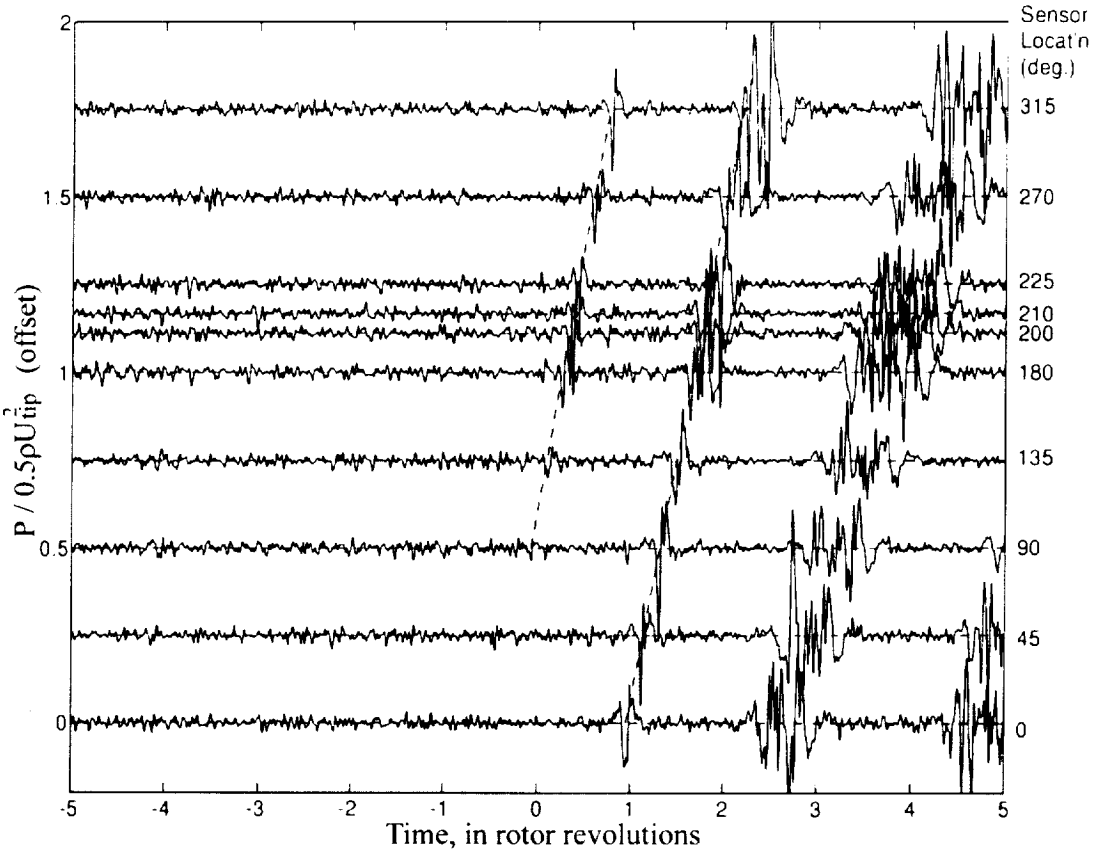

Figure 1.11: Rotating stall is triggered as one spike grows and forms a large stall cell.[56]

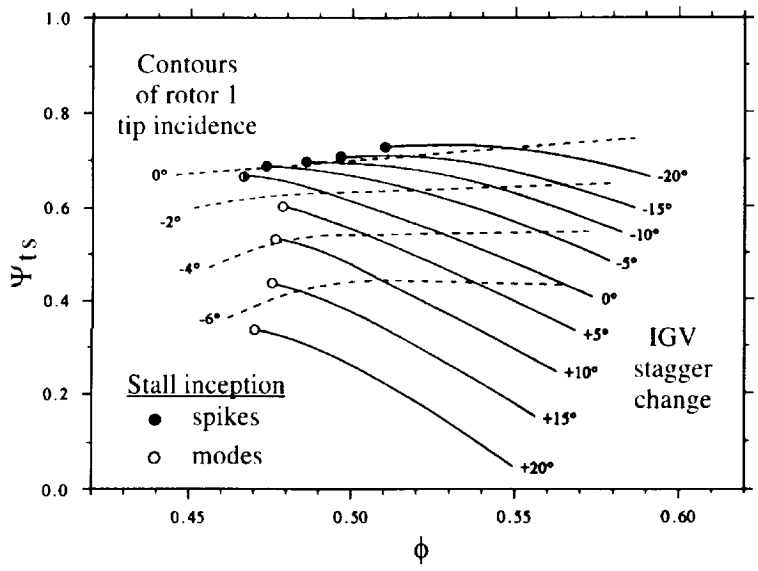

Figure 1.12: Effects of IGV stagger and the "unique rotor tip incidence" [5].

earliest and strongest signals. This observation suggests that the initial spike-shaped disturbance assume the largest amplitude at the rotor exit.

1.3.5 An Investigation of the Conditions Under Which Short Wavelength Stall Inception Occurs

From experimental observations, Camp and Day [4, 5] concluded that the spike-type stall inception occurs at a "unique rotor tip incidence" (Fig. 1.12). They examined a specific compressor with different IGV stagger angles and found that the stall points line up on a constant rotor tip incidence line whenever the compressor shows spike as its stall inception mechanism. The stall inception mechanism could be switched between modal type and spike-type for the same rotor and stator but with different IGV stagger. The overall trend is that when the first rotor is highly loaded (higher pressure rise for the given flow coefficient), the compressor tends to show spike-type inception, otherwise it shows the modal type of stall inception. These experiments suggest that the first-stage rotor is the key component responsible for the spike-type stall inception.

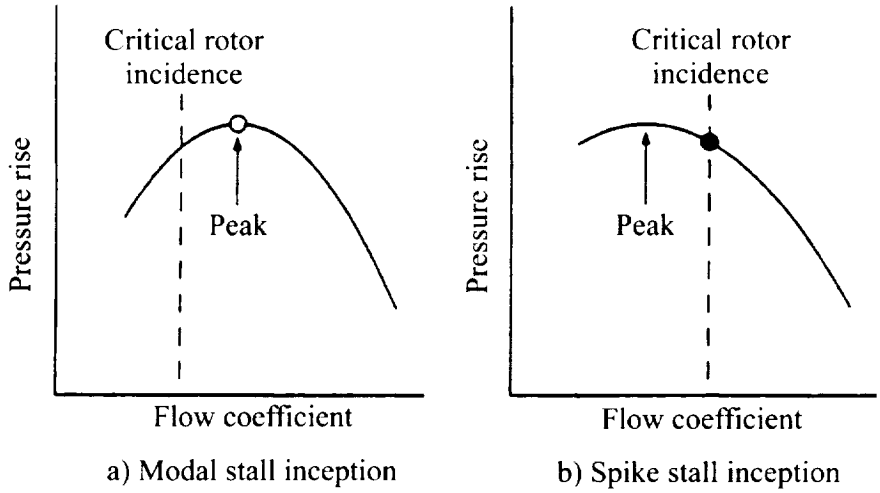

Figure 1.13: A model for determining the stall inception type of a compressor [5].

Based on their observation, Camp and Day proposed a "unique rotor tip incidence" as a short wavelength stall criterion (Fig. 1.13). When this incidence is reached before the peak of the compressor characteristic, the compressor will stall through short wavelength disturbances; otherwise the compressor will stall at the peak pressure rise and show modal waves as its stall inception type.

1.3.6 A Summary of Short Wavelength Stall Inception

From experimental observations, one can conclude that short wavelength stall inception is an important type of stall inception. Based on the observations, an approximate flow pattern around a short wavelength disturbance can be deduced. Figure 1.14 illustrates the shape of a short wavelength disturbance on the (x, r) plane, and (x, θ) plane in the tip region and the resulting flow field associated with the presence of the low flow region. The sketch illustrates several features that are essential for any proposed flow model development:

1. Flow redistribution within the gap of the stage where the short wavelength disturbance is initially located (the implication is that a lumped compressor model cannot resolve this type of disturbances).

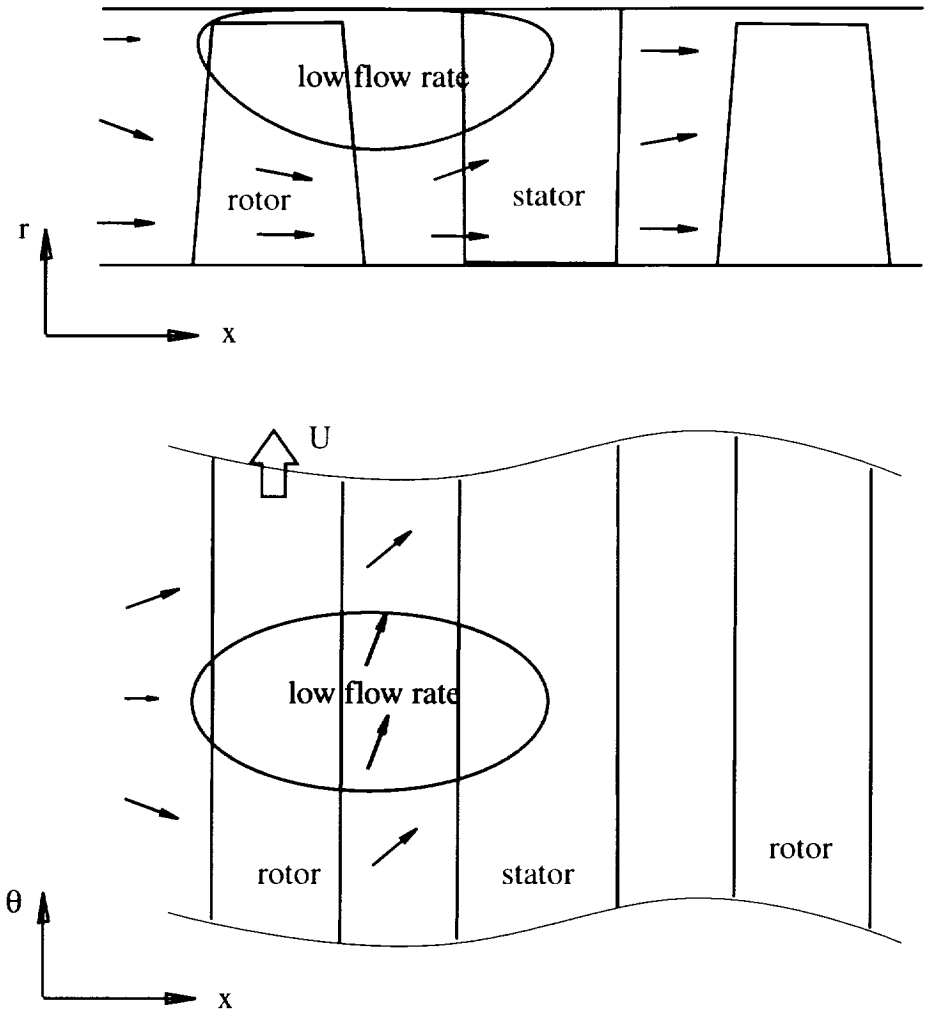

Figure 1.14: A sketch of flow around a short wavelength disturbance.

2. Flow redistribution within a blade row. So the flow at the leading edge of a blade passage can be significantly different from that in the rear part of the blade passage. This implies that a description based on the actuator disk concept cannot represent the flow field around such a short wavelength disturbance.

1.4 A Review of Current Modeling Capability

There are two central issues of rotating stall prediction: rotating speed and instability point, but from the practical point of view, only the instability point is of real con-

cern. Of engineering value is the ability to establish a causal link between instability behavior and compressor design characteristic.

1.4.1 Stall Propagation Mechanism

The first rotating stall model was the analysis and physical description proposed by Emmons [15] (see also Iura and Rannie [36].) Figure 1.6 shows the mechanism of stall propagation. Due to the flow redistribution upstream of a stall cell, a high incidence angle appears in the flow region ahead of the stall cell moving direction, while in the flow region behind the stall cell, the incidence angle is reduced. Therefore, at one side, flow redistribution causes the blades to stall, while at the other, blade loading is reduced, so the blade will get out of stall. Although the sketch only shows one of several possible stall propagation mechanisms, the idea is so intuitive that it is widely accepted by both academic and industrial communities.

Cumpsty and Greitzer [7] used the balance between acceleration in the rotor, stator, and upstream and downstream ducts to argue that the rotating speed of stall cell is determined as the speed at which the unsteady inertial effects in rotors are balanced by the unsteady inertial effects in stationary components. Their model predicted well the measured speed of rotating stall cells. The results suggest that although the flow redistribution idea is intuitive, the key mechanism for propagation is due to the inertial effects in blade rows and ducts. Later, Longley [43] showed that the flow redistribution effects do contribute to the rotating speed of stall cells.

1.4.2 Zero Slope of Characteristic as An Instability Criterion

The most well-known instability criterion, which states that the instability will occur at the zero-slope point (peak) of the characteristic, was proposed by Dunham [14]. He found that at the zero slope of total-to-static pressure rise characteristic, the compressor flow field is neutrally stable (i.e. disturbances do not decay).

A static stability argument for the criterion can be illustrated in Fig. 1.15. If a compressor is operated in the negatively sloped region, for a small amplitude distur-

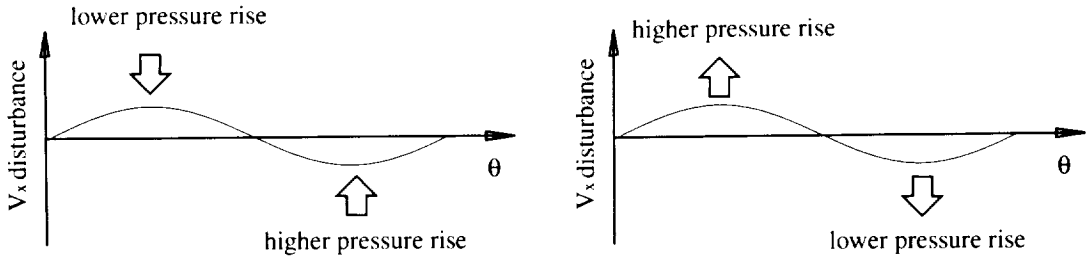

a) A disturbance is suppressed by the compressor in negatively sloped characteristic region

b) A disturbance is amplified by the compressor in positively sloped characteristic region

Figure 1.15: Influence of slope of compressor pressure rise characteristic on stability of disturbances.

bance superimposed on an axisymmetric flow field, the higher flow coefficient region gets lower pressure rise (axial force), while the lower flow coefficient region gets higher pressure rise. Therefore the flow in the higher flow rate region is decelerated and the flow in the lower flow rate region accelerated, thus the disturbance is suppressed. However, if a compressor is operated in the positively sloped region, a disturbance will be amplified, leading to instability. One point to be noted in Dunham's model is that it does not involve the rotating aspect of disturbances. This might indicate that the key mechanism of instability is separated from the mechanism of rotation. It has been shown by some later models [6, 55] that the rotating aspect of a stall cell alters the instability point only slightly.

1.4.3 Moore-Greitzer Theory

Moore [50] modeled a compressor using a lumped compressor representation with a postulated axisymmetric pressure rise characteristic. His model was able to produce the right trends of rotating speed of stall cells for different number of stages, and also the zero-slope criterion of total-to-static pressure rise characteristic as the neutral stability point. The model was subsequently extended to predict compressor performance and instability with inlet distortions [35].

Although most of the work and development of Moore-Greitzer's model has been for linear cases, the model itself is not limited to small amplitude disturbances. For ex-

ample, an inlet distortion can be viewed as a stationary large amplitude disturbance. Mathematically, general non-linear disturbances are very difficult to be treated analytically; however modern CFD methods can be used to simulate the evolution of any type of disturbances in the system. Longley [45] and Hendricks et al [32] used this idea to simulate instability behavior in high-speed compressors. Escuret and Garnier [17] extended the method to three-dimensional cases.

1.4.4 Three-dimensional and Non-linear Methods

Some rotating stall phenomena, like part-span stall and short wavelength stall inception, are three-dimensional and non-linear in nature. Some early efforts [67] to capture the former did not show much positive results mostly due to the lack of computational resources. Recently, several CFD methods have been used to simulate compressor instability [31, 34]. One advantage of these methods is that they can relate the blade passage events to the instability. Hoying et al [34], based on the computational results, found that the tip vortex movement could cause local flow field breakdown which subsequently causes a stall cell in a single blade row. One uncertainty of these calculations is that they are performed on a single rotor blade row, since no data are available on short wavelength stall inception in a single rotor. Although CFD can play a potential role for implementing computation to provide information on instability behavior that is difficult to measure in a laboratory/test rig, such simulations are still beyond the presently available computational resources for multistage axial compressors.

There is another class of methods that uses both modeling and CFD technique to model the flow in a compression system. These methods could handle three-dimensional nonlinear flow phenomena in a practical manner and require reasonable amount of computational resources. These methods have been demonstrated to be able to compute steady three-dimensional inlet distortion cases [3], long wavelength disturbances in a three-dimensional compressor [17] and disturbances in two-dimensional high-speed compressors [32]. Conceptually this type of model is able to handle non-linear three-dimensional disturbances (e.g. spikes) in a compressor,

however no effort/calculations have been made to demonstrate this.

In summary, current modeling capability has been successful for the modal type disturbances, but no model describes the spike type of stall inception. The desire to understand the short wavelength disturbances in a compression system and the lack of the capability to model these types of three-dimensional non-linear disturbances in a compressor motivate the current research project.

1.5 Scope of the thesis

The goals of the research project are:

- to develop a methodology for describing unsteady three-dimensional disturbances associated with flow instability phenomena in a compression system;
- to assess the methodology for predicting both linear long wavelength and non-linear short wavelength disturbances;
- to assess the effects of design parameters on the type of stall inception and the instability point.
- to demonstrate the usability of the methodology for high-speed compressors in situations with general type of inlet distortions.

Some specific questions of engineering interest are:

1. What is the simplest model capable of describing the short wavelength disturbances?
2. What are the key design characteristics which affect the instability point and its inception type?
3. When does a compressor exhibit short wavelength stall inception?
4. What are the capabilities of the developed methodology?

The thesis is organized as follows: Chapter 2 presents the development of the computational model; Chapter 3 presents an assessment of the model against known results; Chapter 4 describes a limited parametric study to reveal the impact of some relevant design parameters; Chapter 5 discusses the implication of the results; Chapter 6 extends the model to high-speed compressors with inlet distortions; Chapter 7 presents a summary and conclusions. The Appendix describes a way of developing a body force representation for blade-rows based on experimental measurements for high-speed compressors.

1.6 Contributions

The key contributions of the present thesis are:

1. A well assessed three-dimensional non-linear compressor model has been developed. The model includes a major improvement upon other three-dimensional compressor models, which is that the flow redistribution within blade rows is properly addressed. The model has been demonstrated to be capable of simulating rotating stall initiated by short wavelength disturbances. To the author's knowledge, this is the first-of-a-kind capability that has been demonstrated by a model. The methodology also has been used to model flow field in a high-speed compressor with distorted inlet stagnation pressure and temperature distortions. The methodology has the potential of describing a wide variety of disturbances in compressors, including part-span stall, three-dimensional dynamic inlet distortions, non-uniformity caused by downstream components, non-uniform loading around the annulus (e.g. due to non-uniform tip clearances, or imperfection due to manufacturing).

2. Key features of the stall inception process through short wavelength disturbances have been reproduced by the model. Parametric studies have been conducted to explore the mechanism of this type of stall inception. Several findings are deduced from the computed results:

- The growth of finite amplitude short wavelength disturbances (length scale of several blade pitches) can be sufficiently modeled by a smeared-out (infinite number of blades assumption) model. The ingredients of the model are three-dimensional, non-linear, and row by row representation of compressor response to finite amplitude disturbances.
- Localized disturbances of sufficient amplitude are required to initiate the short wavelength route to rotating stall. In other words, the phenomena are essentially non-linear.
- The computations show instability occurring on the negatively sloped part of the overall compressor characteristic, in agreement with experimental measurements. This is in direct contrast to the predictions of the modal type of analyses in which the instability will occur at the peak of the characteristic.
- Closing the rotor-stator gaps around the rotor in which short wavelength disturbances occur suppresses the growth of these, thereby improving compressor stability.

3. A concept, *component group*, is deduced from the computation results. The growth or decay of short wavelength disturbances in a rotor is determined by the design characteristics of the isolated *component group* consisting of the rotor and its neighboring stators. The concept is deduced from the computed results based on the model. The component group concept is then used to explain why the short wavelength stall inception often starts in the first rotor. This is because the component group (IGV-rotor-stator, or rotor-stator) involving the first rotor is quite different from the component group (stator-rotor-stator) in the rest of the compressor even though each stage has exactly the same geometry and similar flow field. Therefore the first rotor has less (or none) stabilizing influence from its upstream component. Each component group in a compressor has its own instability point, and thus the point at which stall occurs (i.e. propagating asymmetrical disturbances do not decay) via the short

wavelength route is set by the most unstable component group where large amplitude disturbances are present.

4. The methodology has been extended to model non-linear three-dimensional disturbances in high-speed compressors. Preliminary results show that the model is able to represent the compressor response to non-linear unsteady disturbances.

Chapter 2

Development of A Computational Model

A non-linear three-dimensional computational model will be developed in this chapter. The model is aimed at simulating three-dimensional finite amplitude disturbances such as inlet distortions, short wavelength stall inception processes, and part-span stall cells, which are encountered by compressors. In the model development, the short wavelength stall inception process is considered as a focus (and a major application) of the model.

2.1 General consideration of the model

2.1.1 Desired Model Features

Based on observations of short wavelength stall inception, it was decided to develop a model which could describe the general three-dimensional non-linear, short and long wavelength disturbances in a multistage compressor on a quantitative level. The model should at the very least include the following:

1. A non-linear three-dimensional flow field which includes

    - flow redistribution between blade rows;

- flow redistribution in each blade;

2. The response of blade rows to general three-dimensional non-linear disturbances;

2.1.2 Simplifications of the Model

To make the model practicable in terms of currently available computational resources, (i.e. to avoid the need to resolve the flow structure in each individual blade passage), the following simplifications are made.

1. Infinite number of blades assumption. There are two considerations that should be noted: (i) the phenomena of smallest length scale under consideration has a length scale of several blade pitches, so that the present assumption is marginal in being adequate to capture the key physics of these disturbances; (ii) the resolution of flow field in every blade passage is not computationally feasible with currently available computational resources. The adequacy will thus be assessed and justified a posteriori.

2. A local pressure rise characteristic in every small portion of a blade passage can be defined. This aspect of the model is different from the other two-dimensional and three-dimensional models [50, 45, 17], which assume that blade row (compressor) performance is essentially set by the inlet conditions. It is essential for a blade row to respond in a local manner, since flow redistribution is expected within a blade row. This treatment is consistent with the infinite number of blades assumption, and is thus good for a blade passage of high solidity.

The model is first developed for incompressible flow, and then extended to compressible flow situations in Chapter 6.

2.1.3 Preliminary Justification of The Infinite Number of Blade Assumption

The infinite number of blades assumption (which appears marginal for determining flow behavior associated with spikes) is also supported by the following observations:

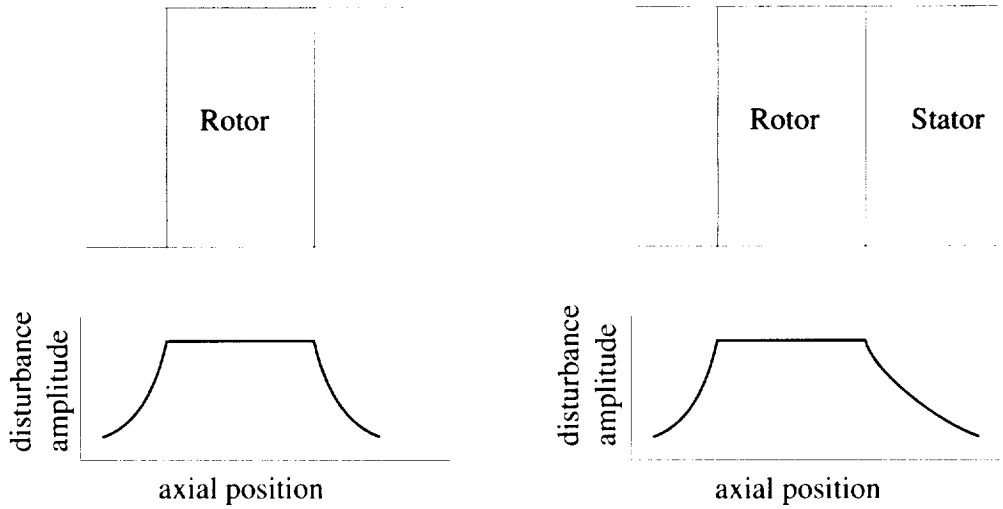

Figure 2.1: The localized disturbance around a rotor blade row. The decay rate of the disturbance can be affected by the downstream stator.

(1) the shape of a spike is relatively stable (it does not vary as it moves at a speed different from the blade speed); (2) its rotating speed is within the range that could be estimated using the inertia balance involving fluid in rotor, stator, and duct.

The General Electric E^3 compressor (Silkowski,1992) is taken as an example to estimate the rotating speed of a spike using the inertia balance concept. Experimental observations indicate that the disturbance is located in a rotor blade row. The amplitude of the disturbance in the rotor is roughly constant, and decays in both the upstream and downstream regions (as shown in Fig. 2.1). The dominant circumferential wave number, n_{cir}, is 20, since the width of a spike is about 1/20 annulus and the behavior of one local stall cell and several (up to twelve) cells are similar. The dominant radial wave number, n_{rad}, is estimated as one. Following Hynes & Greitzer [35], the inertia of rotor, λ, can be calculated using

$$\lambda = b_x / r \cos^2 \gamma$$

for the GE E^3 compressor, as 0.23. The inertia of fluid in the blade free region can

be estimated using

$$\mu = \frac{1}{\sqrt{n_{cir}^2 + (\frac{\pi}{span} n_{rad})^2}}$$

and that in the downstream stator can be estimated using

$$\mu = \frac{1}{\cos\gamma} \frac{1}{\frac{\pi}{span} n_{rad}}$$

The flow inertia for the blade-free region of the GE compressor is 0.036, and that for a stator is 0.069. The rotating speed of this disturbance can now be estimated using

$$\omega = \frac{\lambda}{\mu_{upstream} + \mu_{downstream} + \lambda} \omega_{rotor}$$

The blade-free downstream case gives a rotating speed of 0.76 rotor speed, and the zero rotor-stator gap case gives a rotating speed of 0.69. Both values are reasonably close to the measured value of 0.71.

The flow in each infinitesimal blade passage can be reasonably assumed to be axisymmetric, and the effects of a blade row can be modeled by a body force field [46, 33]. It might be helpful to look at the current level of modeling by comparing it with other types of modeling. Figure 2.2 illustrates models with different levels of complexity. The removal of the blade passage event makes the model of practical value in terms of implementation, while inclusion of the three-dimensionality enables the model to deal with three-dimensional disturbances.

The rest of the chapter is devoted to discussing detailed modeling issues which include (1) governing equations for each component in a compression system; (2) body force formulation for a blade row; (3) implementation of the model for short wavelength disturbances.

2.2 Modeling of A Compression System

A compression system, as illustrated in Fig. 2.3, consists of an inlet duct, an exit duct, blade rows, gaps between blade rows, a plenum, and a throttle. Each component will

a) Three-dimensional N-S solver
Pro: able to solve flow structure within and outside of blade passage, therefore to link rotating stall with blade passage events,
Con: need of demanding computational power makes the method impractical based on present computational resources.

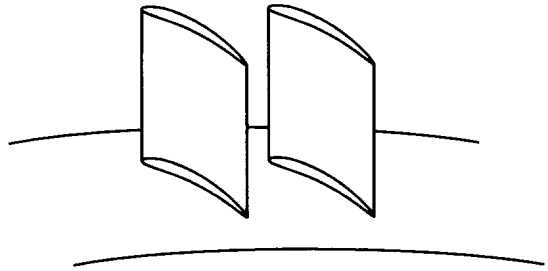

b) Three-dimensional locally axisymmetric Euler solver with body force, the current model.
Pro: able to solve flow structure which is larger than blade pitch; computationally feasible;
Con: cannot link blade passage events to stall inception;

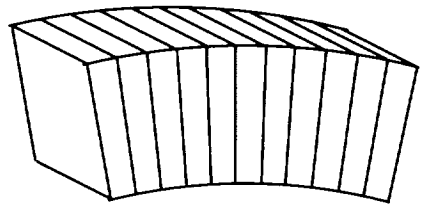

c) Two-dimensional actuator duct
Pro: model can be formulated into an eigenvalue problem
Con: two-dimensional flow only

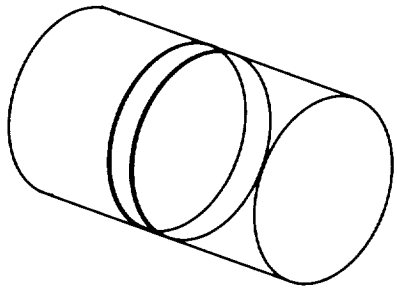

d) Two-dimensional actuator disk theory (Moore & Greitzer model)
Pro: adequate to describe two-dimensional long wavelength disturbances, able to be formulated into an eigenvalue problem
Con: two-dimensional incompressible only

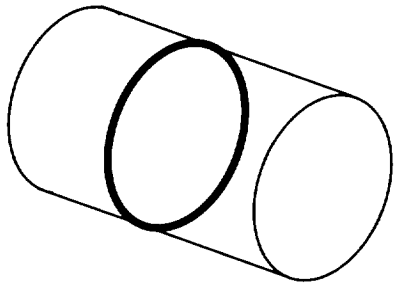

Figure 2.2: The comparison of the complexity of the current model (b) with other models.

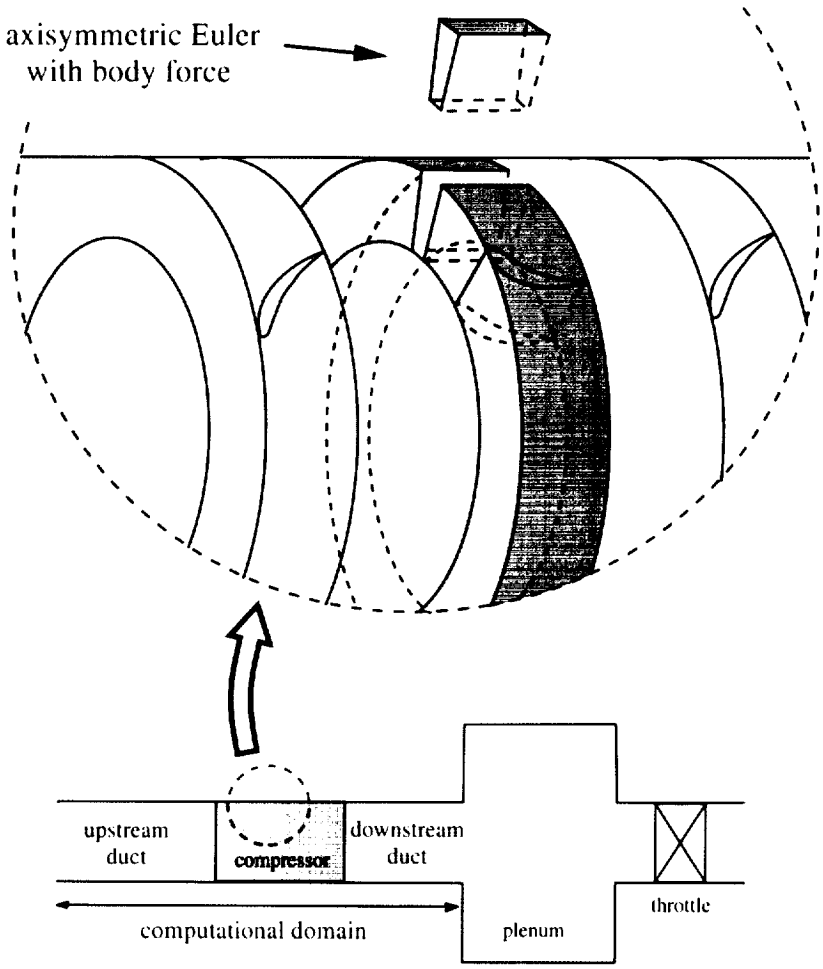

Figure 2.3: Illustration of a compression system and the blade row modeling

be described in the following.

2.2.1 Flow in Ducts

Flow in the inlet duct, exit duct, and gaps is described by the unsteady three-dimensional incompressible inviscid Euler equations. The conservative form of the

set of governing equation can be written as

$$\frac{\partial}{\partial t}\begin{bmatrix} 0 \\ rV_x \\ rV_\theta \\ rV_r \end{bmatrix} + \frac{\partial}{\partial x}\begin{bmatrix} rV_x \\ rV_x^2 + rP/\rho \\ rV_xV_\theta \\ rV_xV_r \end{bmatrix} + \frac{\partial}{\partial \theta}\begin{bmatrix} V_\theta \\ V_xV_\theta \\ V_\theta^2 + P/\rho \\ V_\theta V_r \end{bmatrix}$$

$$+\frac{\partial}{\partial r}\begin{bmatrix} rV_r \\ rV_xV_r \\ rV_\theta V_r \\ rV_r^2 + rP/\rho \end{bmatrix} = \begin{bmatrix} 0 \\ 0 \\ V_\theta V_r \\ V_\theta^2 + P/\rho \end{bmatrix} \tag{2.1}$$

2.2.2 Flow in Blade-rows

Since the number of blades is infinite (or the length scale of flow events is much larger than a blade pitch), the flow at each circumferential position (or at each infinitesimal blade passage) can be regarded as axisymmetric flow in a coordinate frame fixed to the blade row. The pressure rise and flow turning due to blades can thus be simulated by a body force field. Due to presence of the blades, the flow fields between any two blade passages can be different, therefore a three-dimensional flow field in a blade row can be composed of an infinite number of axisymmetric flow fields. The idea is illustrated in Fig. 2.3. The governing equations in the absolute frame can be written as the following form:

$$(\frac{\partial}{\partial t}+\Omega\frac{\partial}{\partial\theta})\begin{bmatrix}0\\ rV_x\\ rV_\theta\\ rV_r\end{bmatrix}+\frac{\partial}{\partial x}\begin{bmatrix}rV_r\\ rV_x^2+rP/\rho\\ rV_xV_\theta\\ rV_xV_r\end{bmatrix}+\frac{\partial}{\partial r}\begin{bmatrix}rV_x\\ rV_xV_r\\ rV_\theta V_r\\ rV_r^2+rP/\rho\end{bmatrix}$$

$$=\begin{bmatrix}0\\ F_x\\ V_\theta V_r+F_\theta\\ V_\theta^2+P/\rho+F_r\end{bmatrix} \tag{2.2}$$

where

$$(F_x,F_\theta,F_r)=\mathbf{F}(\mathbf{V}(x,\theta,r),x,r) \tag{2.3}$$

The equation set is derived through the following steps:

1. Transform Equation 2.1 into the blade row relative frame (i.e., the rotating frame for the rotor) using

$$\left.\frac{\partial}{\partial t}\right|_{stationary}=\left.(\frac{\partial}{\partial t}-\Omega\frac{\partial}{\partial\theta})\right|_{blade\ row} \tag{2.4}$$

2. Remove all $\partial/\partial\theta$ terms in the equation set;

3. Tranform the equation back to the stationary frame using

$$\left.\frac{\partial}{\partial t}\right|_{blade\ row}=\left.(\frac{\partial}{\partial t}+\Omega\frac{\partial}{\partial\theta})\right|_{stationary} \tag{2.5}$$

The first two steps are to obtain the axisymmetric flow equation set in the frame which fixed on the blade row. The equation set is then transformed to the stationary frame.

The operator $\partial/\partial t + \Omega\, \partial/\partial\theta$ in Eq. 2.2 is the result of the transformation of $\partial/\partial t$ from the relative frame to the stationary frame. The $\Omega\, \partial/\partial\theta$ represents the effects of a flow field which moves with the rotor and is viewed from the stationary frame. In the momentum equations, the corresponding terms are referred to as the inertia terms [50, 51, 35]. A significant feature of the current body force representation (Eq. 2.3) is that it is a function of local flow properties. This is essential to model short wavelength disturbances in compressors where flow redistribution occurs in a blade row in the presence of these disturbances. The details on the formulation of this type of body force is presented in a separate section in this chapter.

2.2.3 Plenum and Throttle

Following the treatment by Greitzer for a one-dimensional model (Greitzer, 1975), the fluid in the plenum is considered as uniform and isentropic. The dynamics of the plenum can be described by the following equation

$$\frac{dP}{dt} = \frac{\gamma\, P}{\rho\, V_{plenum}}(m_c - m_t) \tag{2.6}$$

where m_c is the mass flow rate from the compressor and m_t the mass flow rate through the throttle, and V_{plenum} the volume of the plenum.

The throttle pressure drop is given as

$$\frac{P - P_{ambient}}{\rho U^2} = K_t \phi^2 \tag{2.7}$$

Since the plenum has little effect on the early development of short wavelength disturbances, the plenum volume can be set to zero and it is done so here. Thus the governing equation for plenum and throttle becomes

$$\frac{P_{exit} - P_{ambient}}{\rho U^2} = K_t \phi^2 \tag{2.8}$$

where P_{exit} is the static pressure at the exit of the computation domain.

2.3 Construction of A Force Field Within Blade Rows

The requirements on the body force field are

- in steady axisymmetric condition, the body force should be capable of reproducing the required pressure rise and flow turning;
- the body force should be capable of responding to the flow disturbances for both the steady situations (e.g. inlet distortions) and unsteady flow situations.

The body force field is formulated from the following given the compressor characteristics.

- Pressure rise characteristic $\Psi(\phi, r)$ in each blade row;
- Exit relative flow angle $\beta_{exit}(r)$;
- Blade metal angle (or nominal angle along which the flow is expected to follow) distribution $\beta_{metal}(x, r)$

Sometimes not all of the required data are available, and thus some extrapolation is inevitable.

It should be noted that the way of constructing a body force field is not unique, nor is the body force itself for the given requirements and available data. The principles of construction of a body force field will be illustrated through a real compressor which is used as a test bed by the model.

The available data of the GE compressor are listed in the following:

- Compressor configuration and its geometry (end walls, blade rows, etc.).
- Blade row inlet and exit metal angles (or nominal flow angles) which will be . used to form the body force which turns the flow.
- Stage total-to-static pressure rise.

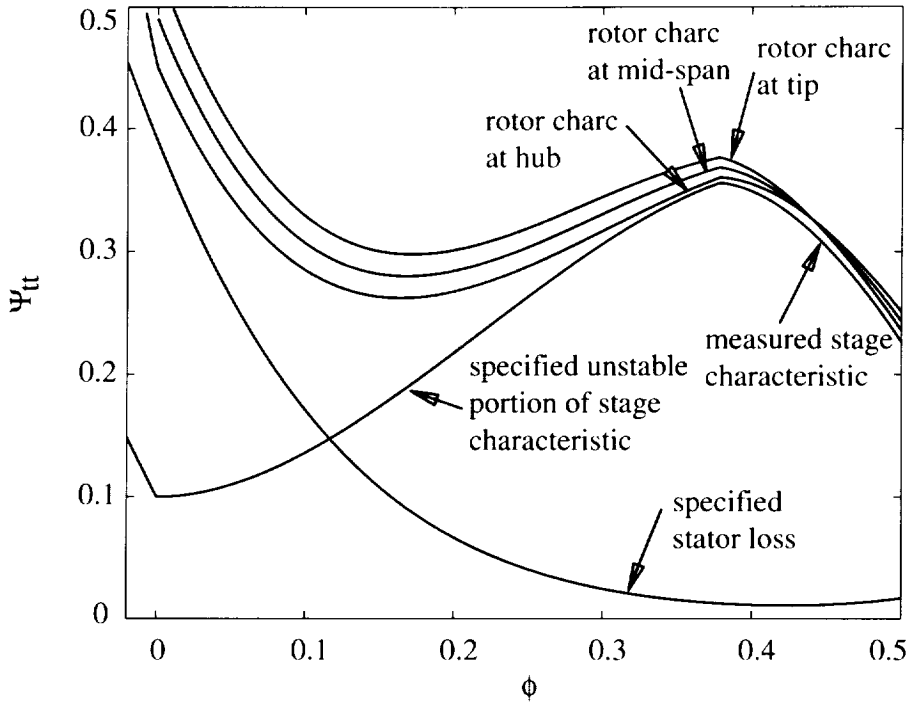

Figure 2.4: The characteristics of the rotor and stator of the first stage are constructed. Only the right-to-the-peak portion of the stage characteristic is measured.

- Exit flow angle profiles at several operating points.

From the input data, the body force can be formulated through the following steps:

Step 1: Formulation of the full range of blade row characteristics

The goal of this step is to determine the total-to-total pressure rise characteristics for each blade row in the whole operating range. More precisely, we are looking for the pressure rise characteristics in the following form:

$$\Psi_{tt} = \Psi_{tt}(\phi, r)$$

for each blade row.

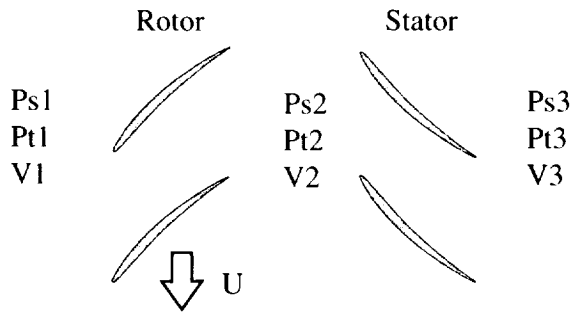

Figure 2.5: Notations of total, static pressure, and velocity at the rotor inlet, rotor-stator gap, and stator exit.

The measured pressure rise characteristic is total-to-static pressure rise characteristic on the stable side. First, a total-to-static pressure rise characteristic in the whole flow range will be constructed. The pressure rise at zero flow coefficient is determined following Day's measured data in low speed rigs [8], and the reverse flow characteristic is a steep straight line where the associated slope is determined from the model of Koff and Greitzer [39]. Connecting the zero-flow-coefficient point and stall point gives the stage pressure rise characteristic in the whole flow coefficient range.

The blade row characteristic can be obtained by assuming a stator loss characteristic. Near the design operating point, the loss is small (could be roughly estimated from compressor efficiency). It is reasonable to state that the total-to-total pressure loss of the stator at zero-flow-coefficient is 0.5. This can be obtained through the following argument. Near zero flow coefficient point, the static pressures at the rotor inlet, rotor-stator gap, and the stator exit (Fig. 2.5) are the same, since the flow in the rotor and stator is at rest. The velocity at the rotor inlet and stator is zero, and the velocity in the gap is the wheel speed of the rotor. Thus we have:

$$P_{s1} = P_{s2} = P_{s3}$$

and

$$V_1 = V_3 = 0$$

$$V_2 = U$$

The notations used here are illustrated in Fig. 2.5. Therefore, the total-to-total pressure rise across the stage, rotor and stator are

$$\frac{P_{t3} - P_{t1}}{\rho U^2} = 0$$

and

$$\frac{P_{t2} - P_{t1}}{\rho U^2} = 0.5$$

$$\frac{P_{t3} - P_{t2}}{\rho U^2} = -0.5$$

The above argument is based on two-dimensional steady flow analysis. The small pressure rise produced by a real compressor at zero-flow-coefficient has to be attributed to the unsteadiness and three-dimensionality of the real flow. Connecting the loss at design flow coefficient and loss at zero flow coefficient gives the whole range of stator loss characteristic. The rotor total-to-total pressure rise is the sum of the stage pressure rise and stator loss.

So far, the overall total-to-total pressure rise characteristics of the rotor and stator have been obtained. The final sub-step is to find the radial variation of the pressure rise. The measurements from the GE four-stage compressor show that the axial velocity profile is kept roughly uniform up to near the stall point. This fact will be used to estimate the radial variation in the static pressure profile using the simple radial equilibrium equation. And the total pressure rise profile along the radial direction can be calculated from the static pressure profile and the velocity profile. At the design point, the flow is assumed to be near a free-vortex pattern, so the total pressure rise characteristics for different radial positions approximately go into one point. The pressure rise at other operating points is estimated using interpolation or extrapolation based on the mean pressure rise characteristic and the radial variation at the design point and a point near the peak.

Step 2: Determination of a streamline pattern through a blade row

This step is required so that flow equations can be applied along streamlines. During this step, the continuity is the only guideline that can be used. For the GE compressor, which is a high hub-to-tip ratio compressor, it is assumed that all streamlines are approximately in the axial direction in the full flow range, since measurements show that the velocity profiles are kept roughly uniform up to a point near stall. This approximation will be used in the next step to formulate the body force for the GE compressor.

Step 3: Determination of body force along each stream line

The goal of this step is to transform the pressure rise across a blade row to a body force field which can be used in the computational model.

It is reasonable to set F_r to zero, since the blade span is roughly in the radial direction.

The blade row characteristic is described by two pieces of information: the total pressure rise and the flow turning. It is therefore desirable to have two pieces of body force which can produce two pieces of blade row characteristic separately. In other words, the body force can conveniently be split into two parts:

$$\mathbf{F} = \mathbf{F}_{P_t} + \mathbf{F}_{turning} \tag{2.9}$$

Such a formulation is possible because the streamlines in the meridional plane are all parallel and in the axial direction (for the GE compressor). The following will show that it is possible to have an axial body force which only produces total pressure rise and the rest of the body force turns the flow.

The total pressure rise rate along the axial direction can be written as

$$\frac{dP_t}{dx} = \frac{dP}{dx} + V_x \frac{dV_x}{dx} + V_\theta \frac{dV_\theta}{dx}$$

Since V_x is constant (to satisfy the continuity condition), the above expression can be written as

$$\begin{aligned}\frac{dP_t}{dx} &= \frac{dP}{dx} + V_\theta \frac{dV_\theta}{dx} \\ &= \frac{dP}{dx} + \tan\beta V_x \frac{dV_\theta}{dx}\end{aligned}$$

Applying the momentum equations give the following equations:

$$\begin{aligned}F_x &= \frac{1}{\rho}\frac{dP}{dx} \\ F_\theta &= \frac{1}{\rho} V_x \frac{dV_\theta}{dx}\end{aligned} \tag{2.10}$$

One can now define

$$F_{P_t,x} = \frac{1}{\rho}\frac{dP_t}{dx} \tag{2.11}$$

Equation 2.11 states that only an axial body force is needed to produce total pressure change. Since $F_{P_t,\theta} = 0$, $\mathbf{F}_{P_t}$ thus does not cause any flow turning. The remaining part of body force only produces flow turning, and can be written as

$$\begin{aligned}F_{turning,x} &= -\tan\beta\ F_\theta \\ F_{turning,\theta} &= F_\theta\end{aligned}$$

Indeed, the above part of body force is normal to the flow direction, therefore it will not affect total pressure. The total body force can now be expressed as

$$\begin{aligned}F_x &= F_{P_t,x} + F_{turning,x} \\ F_\theta &= F_{turning,\theta} \\ F_r &= 0\end{aligned} \tag{2.12}$$

The advantage of using this kind of formulation is that two parts of the body force directly correspond to the available measurements, pressure rise characteristic and turning.

The details of calculating the each piece of body force from the given blade row

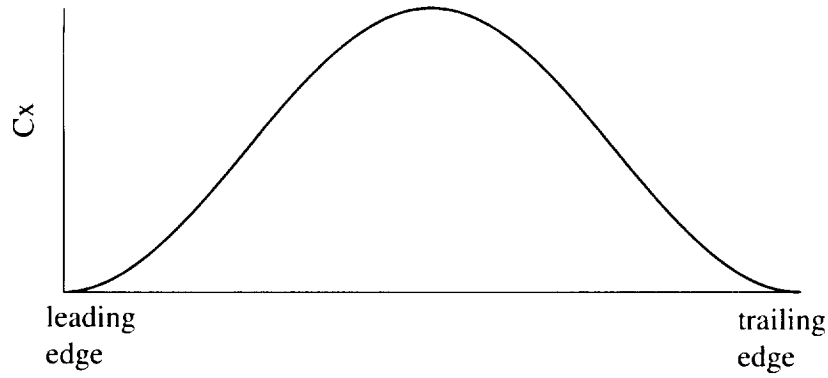

Figure 2.6: The C_x distribution from leading edge to trailing edge.

characteristics will be described as follows. $F_{P_t,x}$ must satisfy the following equation:

$$\Delta P_t = \rho \int_{leading\ edge}^{trailing\ edge} F_{P_t,x} dx \tag{2.13}$$

The $F_{Pt,x}$ distribution from leading edge to trailing edge can be obtained by assuming a distribution function $C_x(x)$ which satisfies

$$f_x \int_{leading\ edge}^{trailing\ edge} C_x(x) dx = \Delta P_t \tag{2.14}$$

where f_x is only a function of ϕ and r (i.e. $F_{x,\ P_t} = f_x C(x)$). The $C_x(x)$ used in the GE compressor is shown in Fig. 2.6. The shape of C_x is chosen for the following computational reason: C_x becomes zero at the leading edge and trailing edge, so that the pressure rise at the leading edge and trailing edge has a smooth transition between blade region and blade-free region, therefore numerical oscillation is greatly reduced around these edges.

It is reasonable to assume a detect-correct type of formulation for $\mathbf{F}_{turning}$ which would continuously act to enforce the flow to be tangential to the blade metal angle (or a nominal flow angle).

$$F_{turning,\theta,} = C_\theta \rho (\tan \beta_{metal} - \tan \beta) V_x^2 \tag{2.15}$$

where C_θ is a constant that will be calibrated to give a measured exit flow angle at the

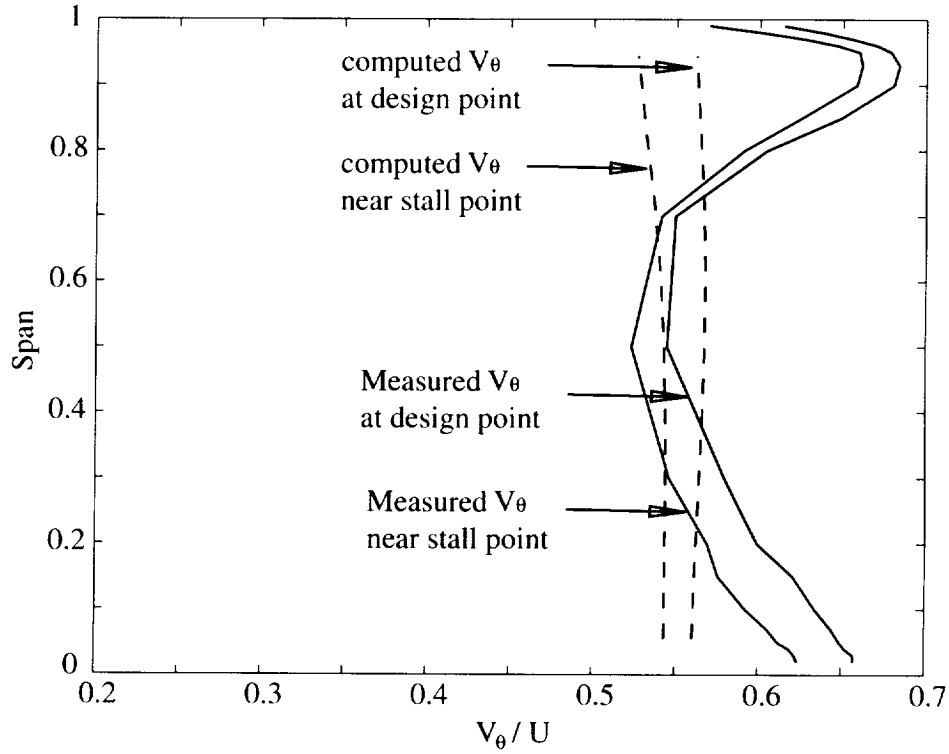

Figure 2.7: Computed V_θ profiles compared reasonably well with measured V_θ profiles at design and near stall flow coefficient.

design point. Once $F_{turning,\theta}$ is obtained, $F_{turning,x}$ can be determined from the fact that $\mathbf{F}_{turning}$ is orthogonal to $\mathbf{V}$. This type of body force worked reasonably well for the GE compressor. Fig. 2.7 shows the measured and computed tangential velocity profiles at the design and near stall flow coefficients of the GE compressor using the body force just described. The results show that the formulation can give not only the right flow angle at design point through calibration, but also a correct trend at an off-design point.

The procedure includes several assumptions. For example, a streamline pattern has to be assumed, and then the body force is calculated based on the assumed streamline. It is expected that the streamlines produced by the body force field will be different from those assumed. In some cases (like the high hub-to-tip ratio GE compressor) the difference is minimal; however, the difference could be quite large for a low hub-to-tip ratio fan since flow redistribution within a blade row can be considerable. In that case, the body force has to be modified based on the computed streamline pattern.

2.4 Implementation of the Model for Simulating the Short Wavelength Stall Inception

There are three issues to be discussed in this section.

- initial disturbances
- determination of stall point
- determination of stall inception type

These issues are unique for calculating a compressor instability point which is a key application of the model. These issues are discussed one by one next.

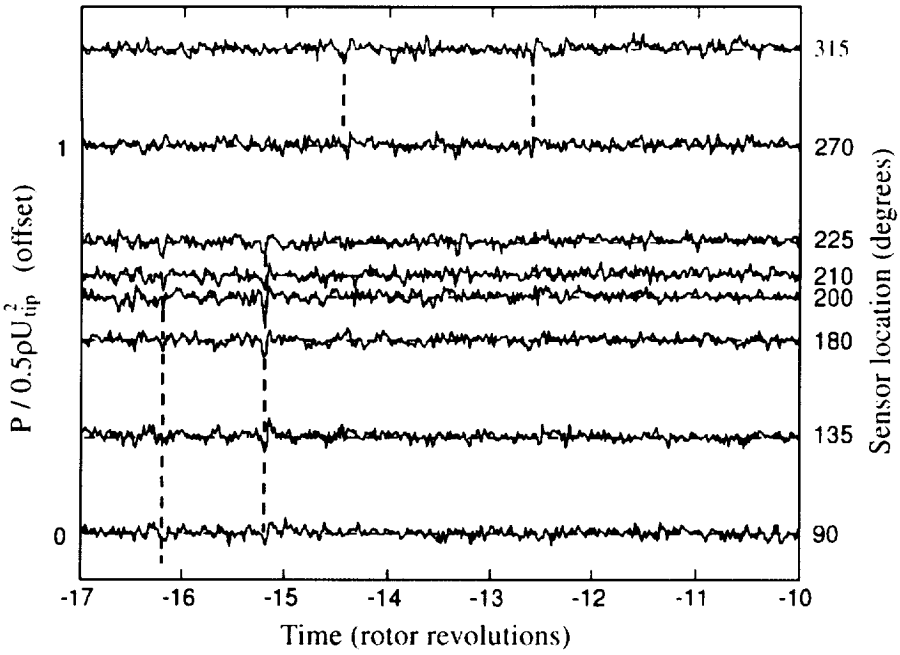

Figure 2.8: Experimental evidence of tip-spikes prior to the development of stall at time=0. The pressure traces, from sensors at different circumferential positions at the first rotor exit, are shifted relative to first trace so that disturbances traveling at 71% of rotor speed line up vertically. Guide lines identify propagating spikes. [56]

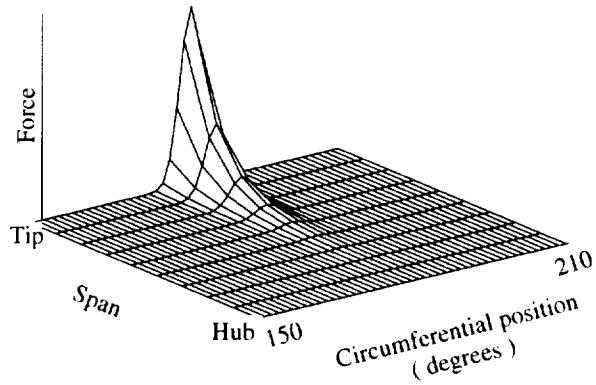

Figure 2.9: Axial body force impulse used to generate spike-shaped disturbances.

2.4.1 Disturbances

Any instabilities have to be initiated from background disturbances which would normally be absent in computations; therefore disturbances have to be part of the input to the computational model. It has been shown that large amplitude short length scale disturbances do exist in a compressor prior to stall [56], in addition to small amplitude, long wavelength disturbances. Therefore, both types of disturbances are used in the simulations. Long wavelength disturbances, extending through the whole compressor, are imposed as an initial condition. Their amplitudes are always less than 1% of the mean velocity. In the simulations performed later, this type of disturbance can be used to determine the long wavelength modal type stall point.

Short wave length flow disturbances are generated by imposing an axial force impulse in the tip region of a selected blade row. The shape of a typical force impulse is shown in Fig. 2.9, and the force impulse lasts for 0.1 rotor revolutions (the only consideration in choosing this value is it has to be much smaller than the time scale of stall inception.) This type of disturbances is used to excite short wavelength instability. For the baseline case, the amplitude of force impulse is equivalent to a 30% loss in the pressure rise within the local blade passage. The chosen value is rather arbitrary, and the effects of the amplitude will be examined in the parametric studies in Chapter 4.

2.4.2 Determination of The Stall Point

Once a disturbance is imposed on a steady flow field, its evolution determines if the compressor's flow field is stable. If the disturbance decays, then the flow in a compressor is stable, and a similar simulation at a lower flow coefficient will be performed. The stall point is determined by repeating the above simulation until a disturbance does not decay.

During each simulation, the throttle is fixed. Continuous changing of throttle is avoided because any numerically acceptable throttle change rate is much faster than that used in experiments.

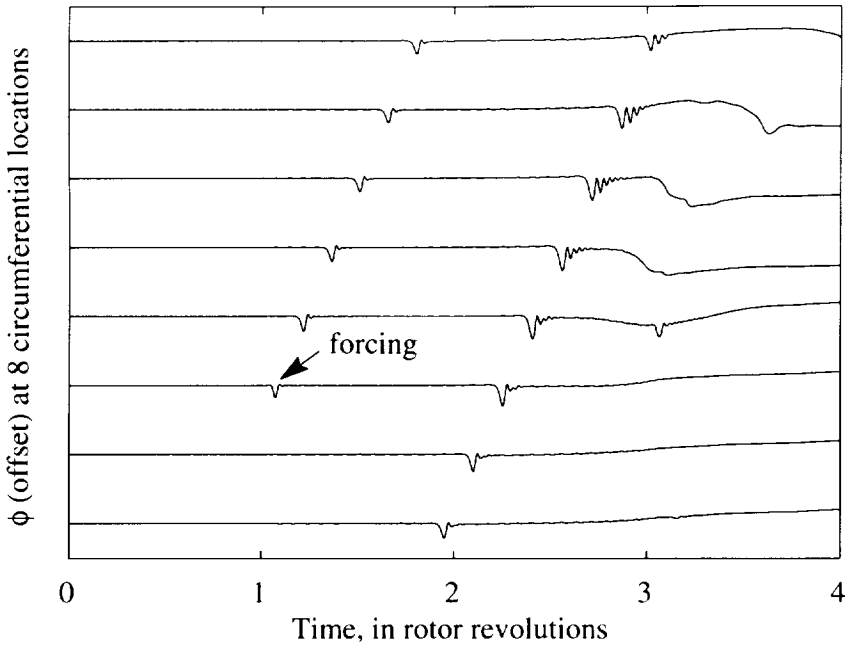

Figure 2.10: Computed ϕ traces when a compressor stalls through short wavelength disturbances.

2.4.3 Determination of The Stall Inception Type

The question to be answered is whether short wavelength stall inception can be distinguished from long wavelength stall inception. For the GE four-stage compressor, the two types of stall inception can be recognized by observing the development of disturbances.

Figure 2.10 shows a typical short wavelength stall inception process from a simulation. The spike-shaped disturbance is sustained and augmented after it is inserted, and then triggers a long wavelength stall cell. Figure 2.11 shows that the spectrum is flat at the beginning, and lasts for about one rotor revolution before the low harmonic contents take over.

In contrast, a modal-stall compressor (the GE compressor with its IGV stagger angle increased by 20 degrees) does not show short wavelength stall inception even if a spike-shaped disturbance is inserted. As shown in Fig. 2.12, a spike-shaped disturbance is suppressed almost immediately after it is inserted, and the compressor stalls through the long wavelength disturbances. The spectrum of disturbances, shown

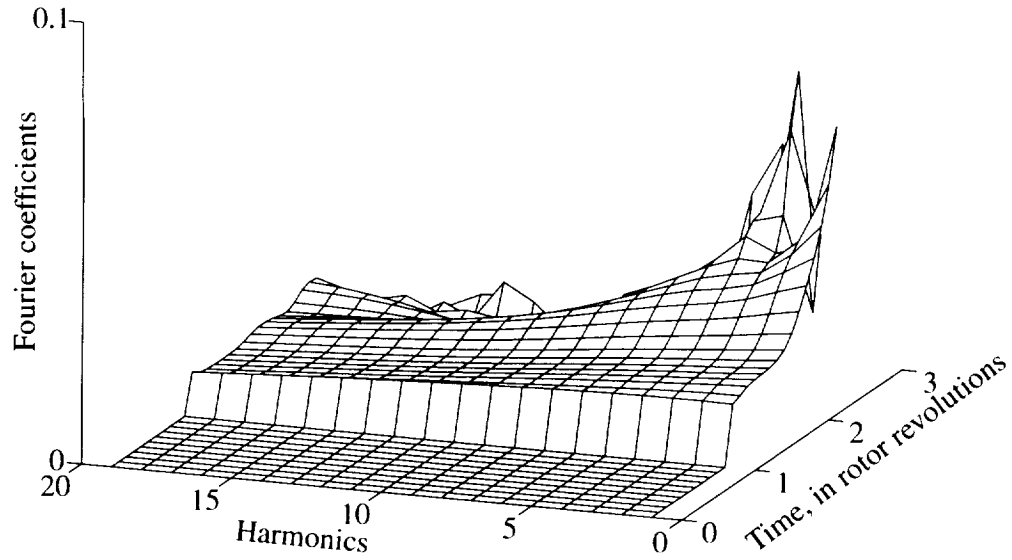

Figure 2.11: Evolution of Fourier coefficients of computed V_x shows a spike-shaped disturbance is sustained by the system, and causes the compressor to stall afterwards.

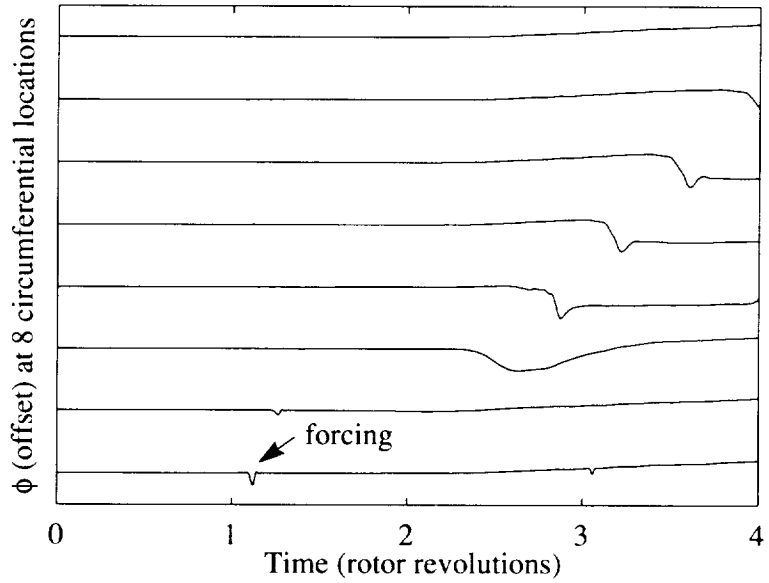

Figure 2.12: Computed V_x traces when a compressor stalls through long wavelength disturbances.

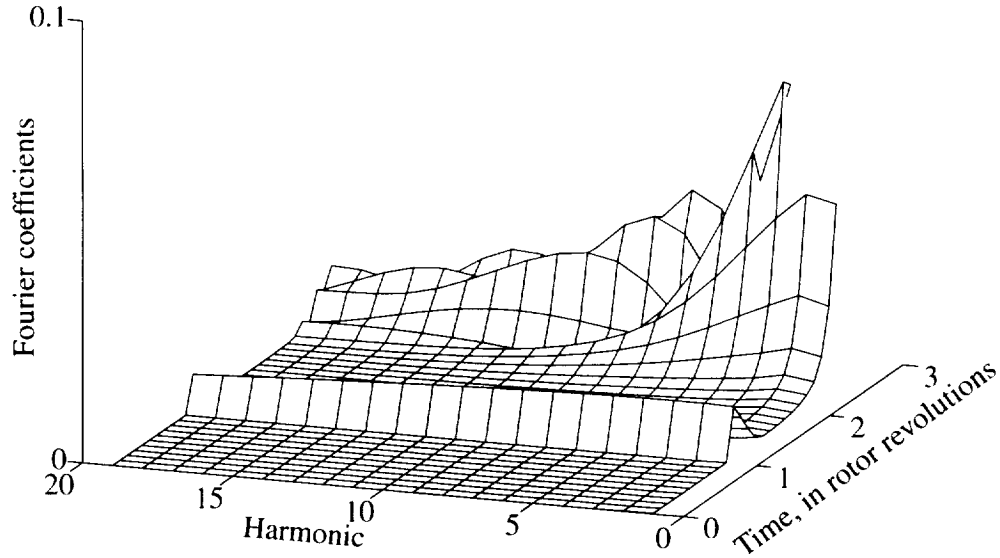

Figure 2.13: Evolution of Fourier coefficients of computed V_x shows a spike-shaped disturbance is suppressed after it is inserted into the system. The compressor stalls afterwards through long wavelength disturbances.

in Fig 2.13, shows that the flat spectrum disappears immediately after the force impulse stops. The ϕ traces (Fig. 2.12) and spectrum (Fig 2.13) do not show a typical modal stall inception which can be explained as a consequence of the nonlinear nature of the initial disturbance. The modal stall type is calculated by imposing a long wavelength disturbance into the compressor. As shown in Fig. 2.14, a clearly exponential growth of the first harmonic Fourier coefficient can be seen. The modal type of this compressor is confirmed by the observation that the compressor stalls at almost the same flow coefficient for either imposing spike-shaped disturbances or long wavelength of disturbances.

Therefore, the spike-shaped short wavelength disturbance can be used to determine the type of stall inception mechanism, as well as the stall flow coefficient of a compressor. In the rest of the thesis, the type of stall inception and stall flow coefficient is determined by observing the evolution of an inserted spike-shaped disturbance.

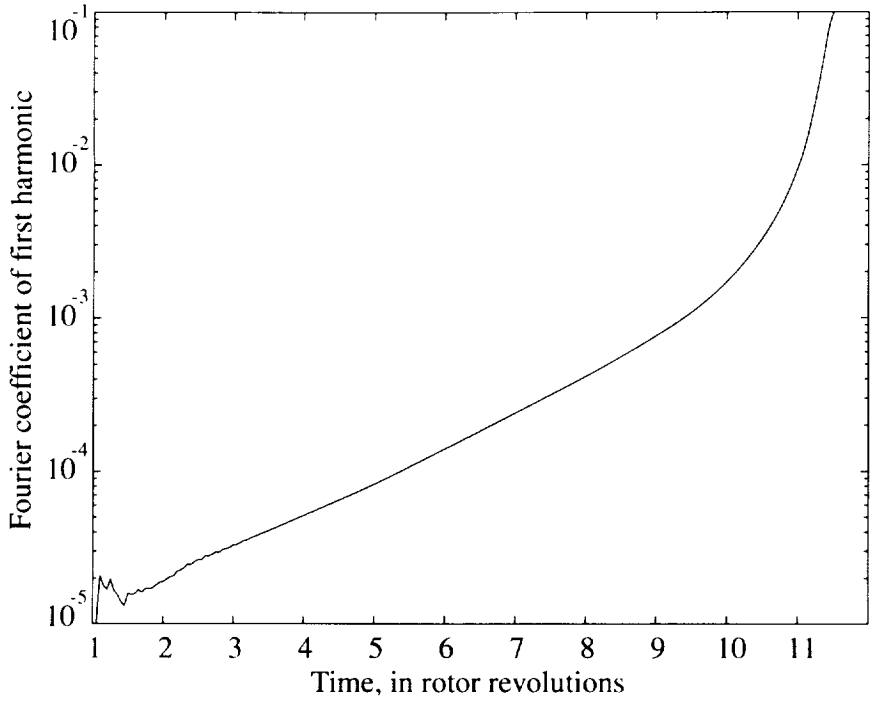

Figure 2.14: The compressor which does not support short wavelength disturbances shows a clear modal wave evolution of first harmonic.

2.5 Numerical method

The solution procedure for the governing equations for the compressor model is based on a standard finite volume for spatial discretization and the multi-stage Runge-Kutta method for time integration [38]. In order to use time marching for incompressible flow, a pseudo-compressible technique is used. The technique adds a $\frac{1}{c^2}\frac{\partial P}{\partial t}$ term into the mass conservation equation. The constant c is referred to as pseudo-speed of sound. To reflect the incompressible nature of the current problem, the pseudo-speed of sound, c, is kept at least ten times larger than the mean flow coefficient ϕ, so that the pressure wave speed is ten times more than the vortical disturbance propagation speed. In all the numerical experiments that have been implemented in this thesis, the influence of c on the computed results is negligible when c is taken to be larger than 10ϕ.

The flows within blade row and duct regions are compatible with one another in the computational domain. This will be elucidated in the following. Figure 2.15

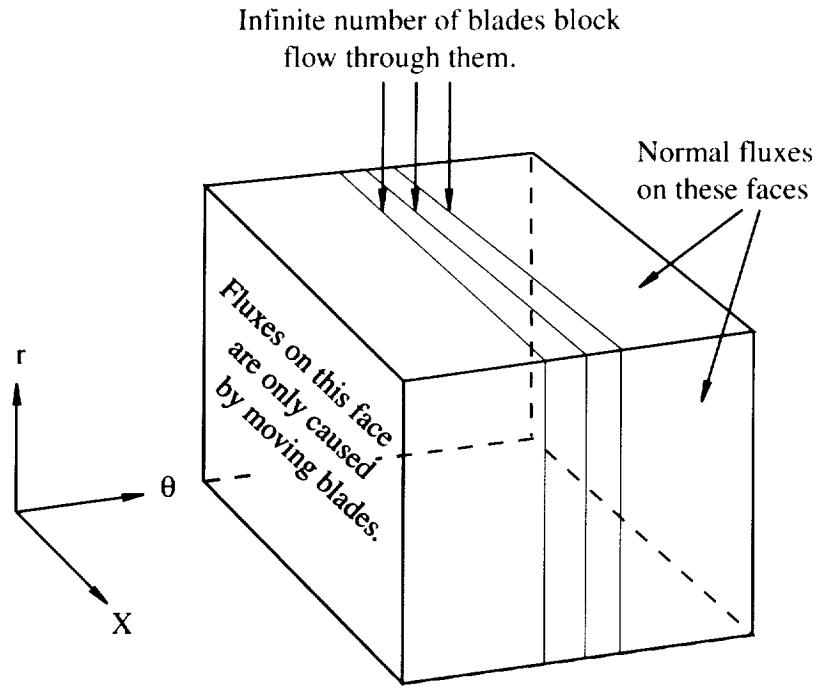

Figure 2.15: Illustration of fluxes evaluation around a cell in the blade row region

shows the fluxes through a computational cell in the blade row region. The role of blades is to block (or force) the fluxes through the constant θ face (in the shadowed area). More specifically, if the cell is in a stator blade row, there is no flux through that face, and if the cell is in a rotor blade row, the flux is evaluated using $\Omega \frac{\partial}{\partial \theta} U$. The term can be viewed as the mass and momentum that are forced into the cell by the moving blades. The fluxes on other faces can be evaluated in the way used by Jameson [38]. The interface between blade row region and duct region is the constant r (or $r = f(x)$) face; the fluxes on that face can be evaluated by the same method as is for the three-dimensional flow region. Thus coupling the two types of flow region will not cause any incompatibility problem.

The inlet and exit boundary conditions are standard one-dimensional linearized boundary conditions [19]. The exit static pressure of the computational domain is updated every iteration using the plenum-throttle equation.

2.6 Summary

A non-linear three-dimensional computational flow model for an axial compressor has been presented. The model emphasizes the three-dimensional unsteady response of blade row to general three-dimensional non-linear flow disturbances.

The implementation of stall simulation is discussed. It is found that a spike-shaped disturbance is necessary to initiate a short wavelength stall inception. Experimental observations show that this type of disturbances do exist prior to stall. Simulations also show that imposing a spike-shaped disturbance can be used to identify the types of stall inception by observing its development.

Chapter 3

Model Assessment

This chapter is focused on assessing the capability of the model developed in the previous chapter. The assessment consists of applying the model to the flow situations, which have either analytical solutions or experimental measurements. Specifically, the following flow situations are considered.

(1) Flow in a compressor with two-dimensional inlet distortion. Due to the response of the compressor to the inlet distortion, the distorted inlet flow is redistributed in the upstream duct. The response of a compressor to an inlet distortion is an ideal situation to assess the ability of the model to describe response of a compressor to finite amplitude disturbances. While the imposed distorted flow is steady, part of the response of the compressor associated with the rotor blade rows (which would perceive an unsteady flow in the rotor reference frame) would be unsteady. Thus this also provides an opportunity to assess the unsteady aspects of the model.

(2) Behavior of two-dimensional small amplitude disturbances in a compressor (linearized stability analysis of compressor response to two-dimensional infinitesimal disturbances): The phase speed and growth rate of this type of disturbances can be calculated by a linear analysis [35]. The model gives results that agree with the linear analysis for small amplitude disturbances.

(3) Behavior of a small amplitude first harmonic disturbance in a three-dimensional compressor (Linearized stability analysis of compressor response to three-dimensional infinitesimal disturbances): This example shows that the model can also produce an

equivalent behavior of a modal wave calculated using a three-dimensional actuator disk model [24].

(4) Short wavelength stall inception in a GE four-stage compressor: It will be shown that the model captures key features of the inception process and its subsequent development.

(5) Short wavelength local stall cells in a mismatched compressor: The situation consists of a "progressive" stall region, where the spike-shaped local stall cells are localized in the first stage and in an equilibrium state, therefore the example provides an opportunity to assess the model quantitatively and on a rigorous basis.

(6) "Unique rotor tip incidence" for short wavelength stall inception and switch of stall inception types: The recent experimental result of Camp and Day [5] shows that a compressor stalls through short wavelength disturbances at a "unique rotor tip incidence", and that the stall inception can switch from short wavelength type to the long wavelength type as the rotor loading is reduced.

3.1 Two-Dimensional Steady Flow Field with Inlet Distortion

The model is used to calculate the steady flow field around a compressor with an inlet distortion, and the result is compared with the theoretical model of Hynes and Greitzer [35]. A large inlet distortion can be considered as a finite amplitude disturbance, thus the example assesses the ability of the model to simulate the behavior of finite amplitude disturbance in a compression system. An inlet distortion calculation is a good preliminary case to assess a compressor model because (1) it is non-linear due to the large amplitude disturbance involved, (2) it involves flow unsteadiness since the steady inlet distortion is unsteady when viewed from the frame of rotor blade rows, (3) it is relatively easy to conduct a quantitative comparison since it is steady in the stationary frame.

The compressor used in this case is a two-dimensional compressor (i.e. a com-

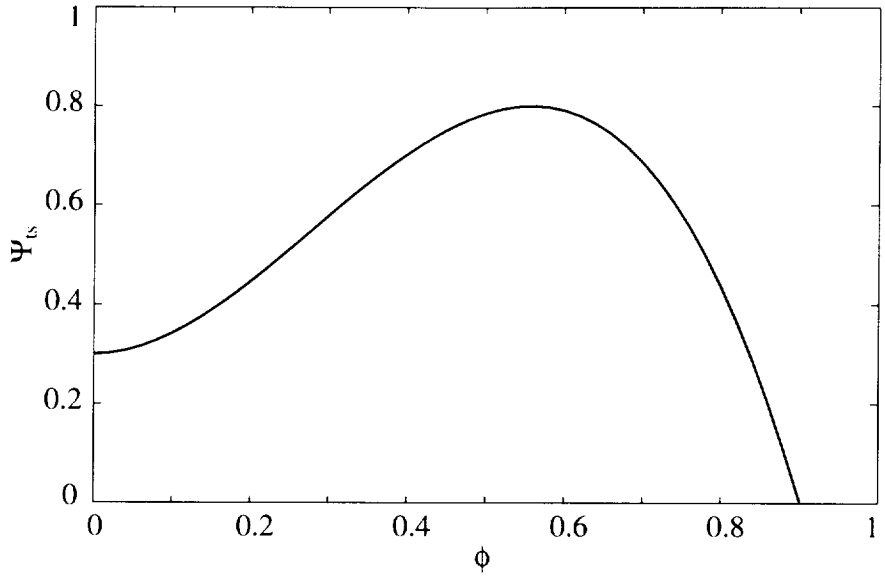

Figure 3.1: The total-to-static pressure rise characteristic used in Section 3.1 and Section 3.2.

pressor with a hub-to-tip ratio of near unity so that the blade span is zero) with a 180°-sector square wave total pressure distortion at a far upstream location. The pressure rise characteristic, shown in Fig. 3.1, is taken from Hynes and Greitzer's paper [35]. The total inertia parameter, μ, is 2.0, and the rotor inertia parameter, λ, is 1.0.

The current model is slightly modified to fit the hypothetical case. Specifically, only one cell is used in the radial direction, and the compressor is lumped and represented by one locally axisymmetric flow region with a body force field. The inlet distortion is represented by a specified total pressure distribution at a far upstream inlet boundary. The figure of merit is the ϕ profile at the compressor inlet face at a specific flow coefficient. The flow field, more specifically the contraction of the distorted flow region near the compressor front face, is illustrated by the total pressure contours (Fig.3.3) which are equivalent to streamlines in the upstream region of the compressor.

The ϕ profile is plotted in Fig. 3.2. There is an excellent match between the analytical result and computed result. The computed result shows that most of the

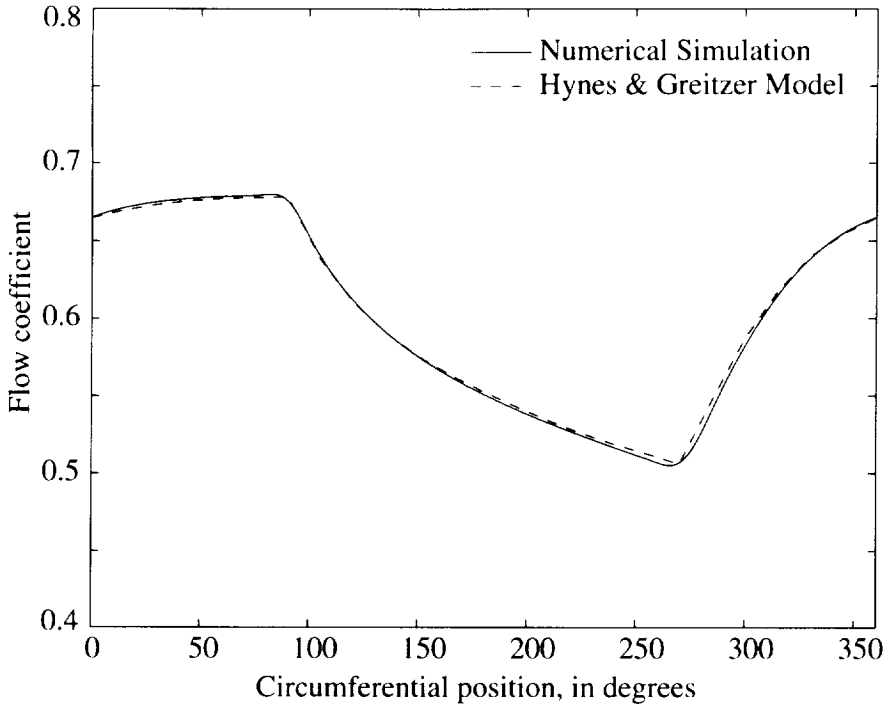

Figure 3.2: V_x distribution at compressor inlet face. The solid line is computed by the computational model, and the dash line the analytical model.

flow redistribution occurs near the compressor inlet. As shown in Fig. 3.4, the ϕ profile at the compressor inlet is noticeably different than the ϕ profile at the location just one cell (0.0016 radius or about 0.2 rotor chord) upstream of the rotor leading edge. The rapid change is associated with high decay rate in the high harmonic content of the response produced by the compressor.

The above computed behavior of the flow field can be used to explain the measurements in a real situation [59]. Figure 3.5 shows the measured ϕ profile in front of the SGV (Servo Guide Vane which is used to suppress pre-stall waves) of a three-stage compressor (Fig. 3.6). The SGV has a long chord and large blade pitch, so high harmonic content decays within the SGV region.

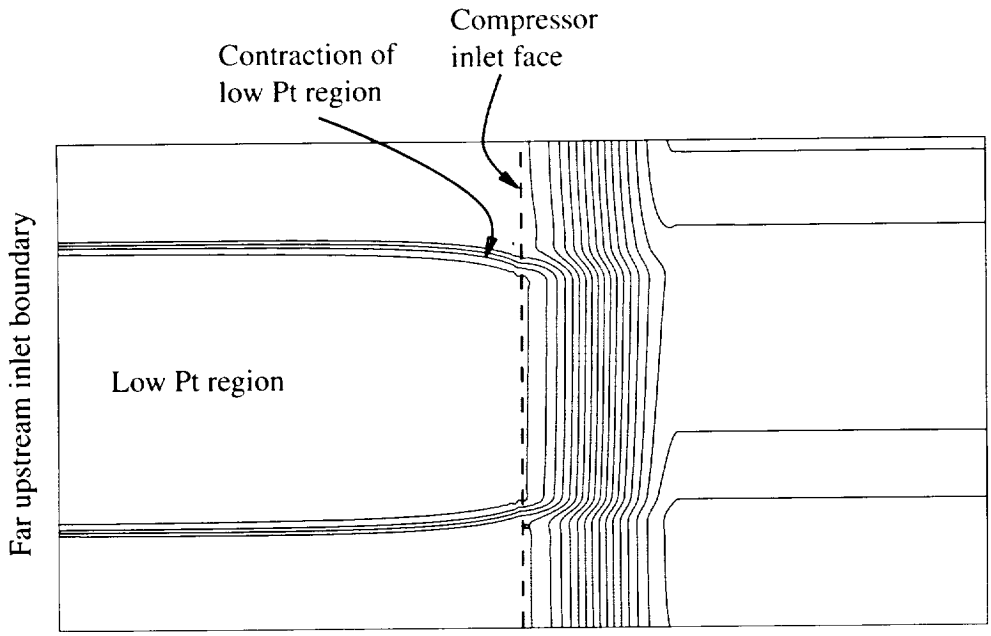

Figure 3.3: Flow redistribution is shown using P_t contours. The plot shows the low P_t region contracts when it reaches the compressor inlet face.

Table 3.1: A comparison between computed and theoretic growth rates and phase speeds of the first circumferential mode.

	Growth rate	Phase speed
Computational model	-0.26	0.27
Theoretic model	-0.26	0.27

3.2 Two-Dimensional Modal Wave

We next examine small amplitude disturbances in a two-dimensional compressor. The compressor is the same as the one taken from reference [35]. At each operating point, each mode has a growth rate and a phase speed predicted using the Moore-Greitzer analysis. The computation is set up in the same way as in the previous section. At a select operating point, a small amplitude first harmonic axial velocity disturbance is inserted into the system at t=0. The evolution of the harmonic determines its growth rate and phase speed, which are the key figures of merit in the comparison. The results from analysis and computation are listed in Table 3.1. The agreement is excellent.

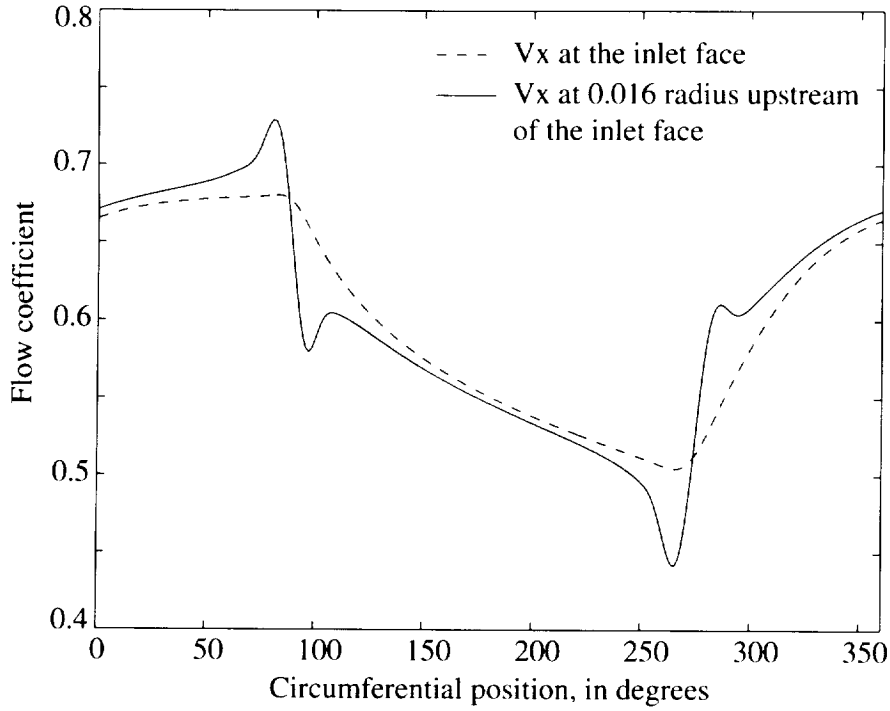

Figure 3.4: V_x distributions near the compressor inlet show strong flow redistribution.

3.3 Three-Dimensional Modal Wave

In this section, the growth rate and phase speed of a linear wave is calculated by the computational method and an analytical method. The analytical method, which was developed by Gordon [24], uses an actuator disk to represent a compressor. The stability calculation involves the solution of an eigenvalue problem formulated by subjecting the compressor steady flow to an infinitesimal flow disturbance (i.e., it is essentially the three-dimensional equivalent of the Moore-Greitzer model). The computational method is implemented by imposing a small amplitude first harmonic disturbance into the system. The growth rate and phase speed are obtained from the computed evolution of the disturbance. The compressor is similar to a single stage fan with a hub-to-tip ratio of 0.43. The pressure rise is one third of the previous compressor, its rotor inertia is 0.25, and total inertia 0.5. Table 3.2 shows the comparisons between the results calculated by computation and by analysis. The results

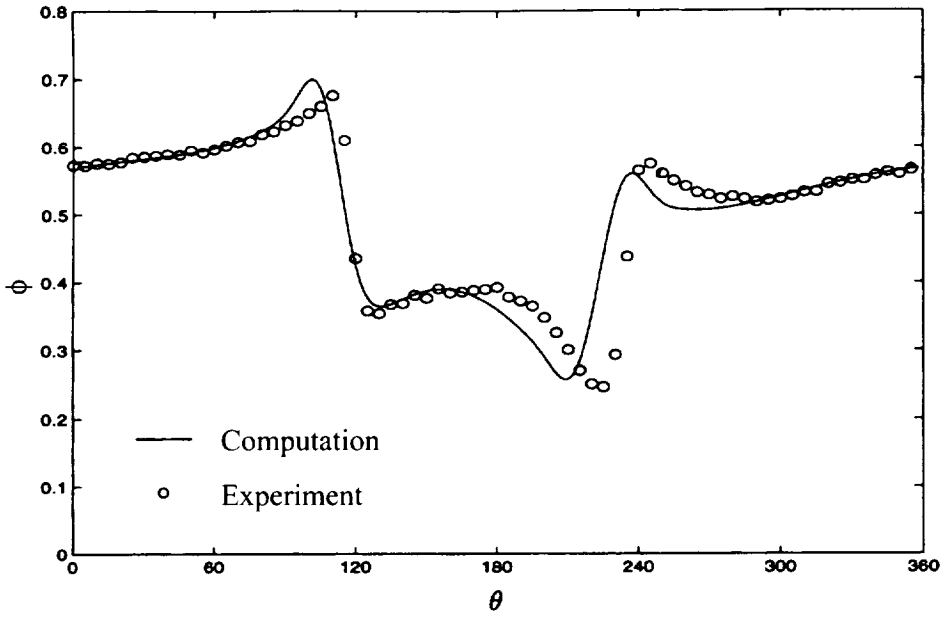

Figure 3.5: The ϕ profile measured from the MIT three-stage compressor is well predicted by the computational model. The sensor location is at a location upstream of the SVG.

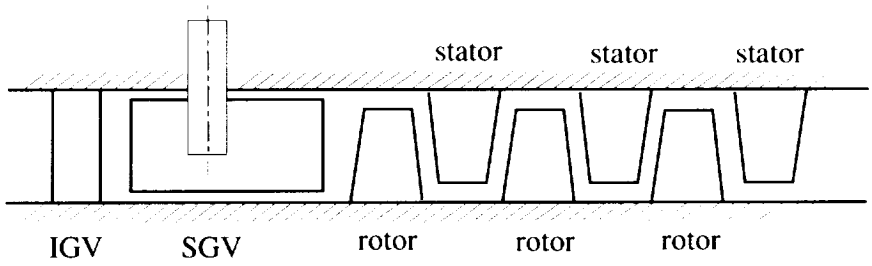

Figure 3.6: A schematic of MIT three-stage compressor with a Servo Guide Vane (SGV) between the IGV and first rotor.

Table 3.2: A comparison of growth rate and phase speed computed using the computational model and analytical model.

	Growth rate	Phase speed
Computational model	-0.11	0.1
Analytic model	-0.1	0.1

are again in good agreement. The phase speed (0.1 rotor speed) is relatively low for this compressor because this is a single stage compressor so that the rotor inertia, which drives the rotation of disturbances, is relatively small.

So far, the results show that the computational model for stall inception is equivalent to linearized eigenvalue analyses for small amplitude disturbances. However, the computational method shows little advantage in those situations where linearized stability analysis is applicable. The strength of the model lies in its ability to compute three-dimensional non-linear disturbances, and this aspect will next be demonstrated.

3.4 Simulation of Stall Inception of A General Electric Four-Stage Compressor, Matched Build

The short wavelength stall inception will be simulated in this section. The example presented represents a first-of-a-kind results on short wavelength stall phenomena in a multi-stage compressor. A General Electric four-stage compressor [71], which consistently shows short wavelength stall inception in the experiments, was chosen as a test case for the computational model. Design parameters of the compressor are listed in Table 3.3. The compressor consists of four identical stages with an IGV at the front.

In the computation, the compressor is represented by individual blade rows and gaps. The computation domain thus includes one IGV, four rotors, four stators, eight gaps, inlet and exit ducts, as shown in Fig. 3.7.

256 cells are used in the circumferential direction to ensure that a typical short wavelength disturbance is sufficiently resolved (by 10-14 cells). There are nine cells in

Table 3.3: The design parameters of General Electric four-stage compressor.

	IGV	Rotor	Stator
Number of blades	110	54	74
Axial chord (in mean radius)	0.10	0.086	0.10
Stagger angle (degrees)	10	50	40
Solidity at middle span	1.4	1.16	1.43
Hub-to-tip ratio	0.85	0.85	0.85

the radial direction, and over 200 in the axial direction. The overall number of cells is over half a million. The details of the mesh in the computational domain are listed in Table 3.4. Although the number of cells along the span appears relatively small, it is selected due to the following three reasons: (1) it yields a reasonable aspect ratio of cells on the $(\theta,\ r)$ plane, (2) it is enough to resolve the first two radial harmonics which should be sufficient for a part-span low velocity region at either tip or hub, (3) the use of much finer mesh (although it is useful to study grid independence of the results) would require an unreasonable amount of computational resources.

A formal grid independence study was not performed due to the limitation of the available computational resources. Calculations were performed for the same compressor with half the number of cells in circumferential direction. The phenomena are qualitatively comparable to the results using the final mesh. The mesh is considered sufficient based on the following reasons: (1) the results compared well with experimental observations, (2) the number of cells used to resolve the phenomena (short wavelength disturbances) is more than ten in all three dimensions.

The body force fields of rotor and stator are formed from the specified characteristics (Fig. 3.8), and nominal blade angle. The portion of the characteristic to the right of the peak is taken from the experimental measurements. The unstable portion (to the left of the peak) of the characteristic is specified based on the curve shape used in the two-dimensional compressor modeling [50, 35]. The details of the body force formulation have been discussed in Chapter 2.

Two types of initial disturbance are used in the simulation. One is a small amplitude long wavelength disturbance, the other a spike-shaped axial force impulse

Table 3.4: The computational mesh distribution used in the simulation of the GE four-stage compressor.

Total number of cells in axial direction	230 57 cells in the inlet duct 10 cells in the IGV 10 cells in the IGV-R1 gap 10 cells in each rotor 10 cells in each stator 4 cells in each rotor-stator gap 45 cells in the exit duct
Number of cells in the spanwise direction	9
Number of cells in the circumferential direction	256
Total number of cells	529,920

(see Fig. 2.9) that lasts for 0.1 rotor revolutions and has a magnitude corresponding to a loss in 30% of pressure rise of one blade passage in the tip region of the first rotor blade row.

The figures of merit for the model are the type of stall inception, the rotational speed of disturbance, and the transition time from the initiation of the disturbance to the formation of a large stall cell.

The simulation shows that the short wavelength stall inception can be initiated by a spike-shaped disturbance. The flow coefficient traces (Fig. 3.10), taken from the tip region of first rotor inlet, show that the disturbance is sustained, and the disturbance leads to compressor stall subsequently. The overall inception is similar to the measurements (Fig. 3.9). The spectrum of computed ϕ in the tip region of the first rotor inlet shows the same process (Fig. 3.11), during which the nearly flat Fourier coefficient distribution is sustained and followed by a subsequent growth of lower harmonic contents.

The different nature of the stall inception initiated by two types of disturbance is further confirmed by plotting the stall points on the characteristic (Fig. 3.12). The short wavelength stall inception occurs at a higher flow coefficient point where the slope is clearly negative, while the modal type stall inception occurs at a lower flow coefficient which is very close to the peak of the characteristic.

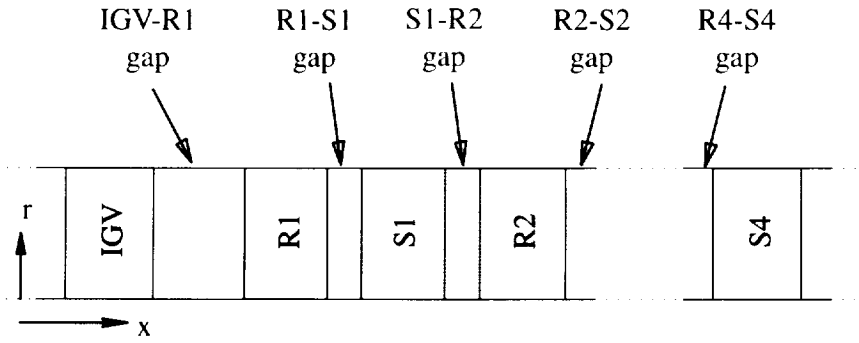

Figure 3.7: A scaled schematic of the GE compressor represented by nine blade rows and eight gaps.

Table 3.5: Comparison between computation and measurement

	Measurement	Computation
Stall Inception Mechanism	Spike	Spike
Rotating Speed of Spike	70-73%	83%
Rotating Speed of Large Stall Cell	45%	20%
Transition Time	about 3 revs	about 2.7 rev

A quantitative comparison shows that the stall inception initiated by spike-shaped disturbance has an initial disturbance rotating speed of 83% of rotor speed, and a transition time of about three rotor revolutions. These compare reasonably well with the experimental observation. Comparison with experimental observation is given in Table 3.5. The rotational speed of the stall cell drops as a large two-dimensional stall cell emerges. The computed rotational speed of the final large stall cell is about 20% which is less than half of the measured value of 45% rotor speed. The cause of the difference is not clear. It is suspected that the blade row characteristics at very low flow coefficient region (near zero flow coefficient) used in the computational have a large error. Since the flow coefficient within a large stall cell is around zero. However, inaccurate blade row characteristics are not expected to change the phenomena related to short wavelength stall inception. The effects of the shape of unstable part of blade row characteristics will be examined in Chapter 4.

Although the computation captures the overall features of short wavelength stall inception, the evolution towards a large stall cell is different from the experimental ob-

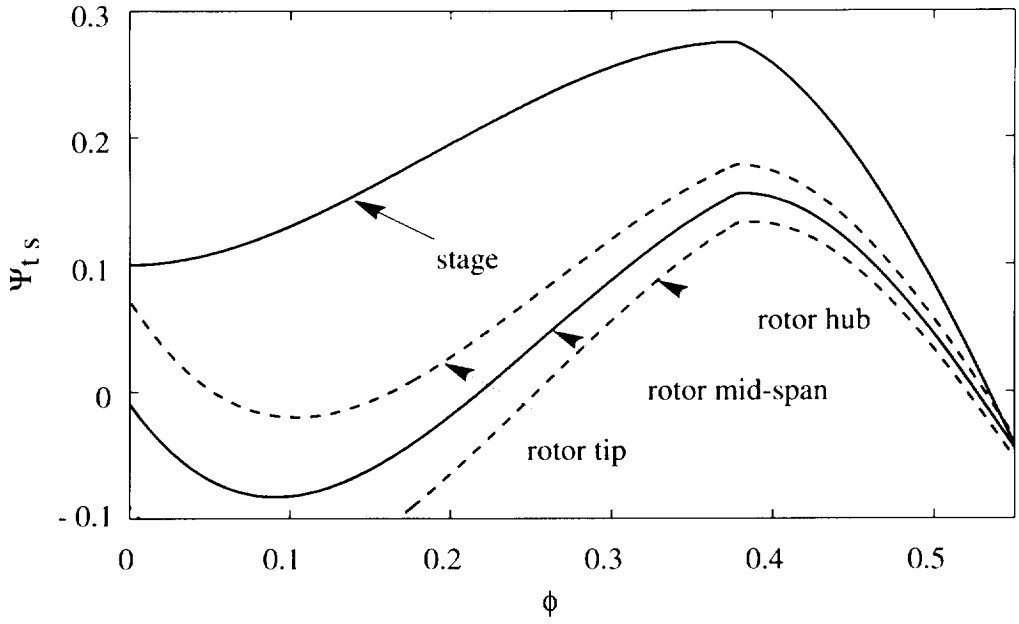

Figure 3.8: Stage characteristic of GE compressor.

servations. The simulation shows that a long wavelength disturbance trails the short wavelength disturbance, and becomes dominant after one to two rotor revolutions. Along with the growth of the long wavelength disturbance, the initially dominant spike-shaped disturbance dies out. The cause of this fast emerging long wavelength disturbance can be found through examining the disturbance development at different blade rows (Fig. 3.13). It appears that a long wavelength disturbance that is triggered by the short wavelength disturbance at the front stage, starts to grow in stage three after it attains a threshold amplitude. Since the long wavelength only appears in certain axial locations, it must have a three-dimensional structure. At between t=2.25 to 2.5 rotor revolutions, the non-linear three-dimensional disturbance (Fig. 3.13) located around the third stage develops rapidly in all directions, and within one rotor revolution it becomes a large two-dimensional stall cell. At this stage, it is difficult to assess the simulated results against the experimental data which now show a somewhat ambiguous behavior. The measured velocity traces indicate that the short wavelength disturbance leads the long wavelength, but it does not leave the long wavelength disturbance, instead, it becomes part of the final stall cell.

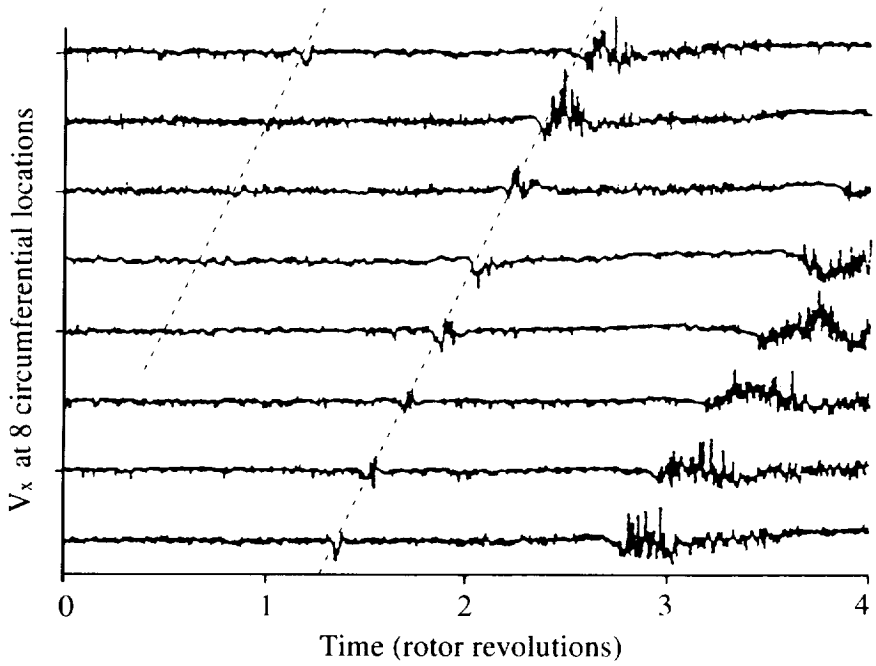

Figure 3.9: Measured tip ϕ traces at the inlet of first rotor for a compressor stalling via short wavelength route.

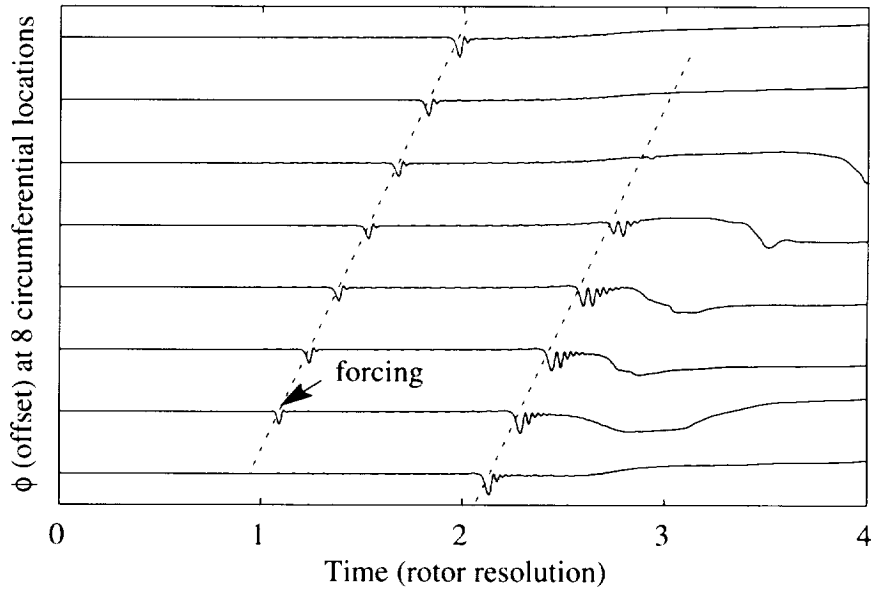

Figure 3.10: Calculated tip ϕ traces at inlet of first rotor

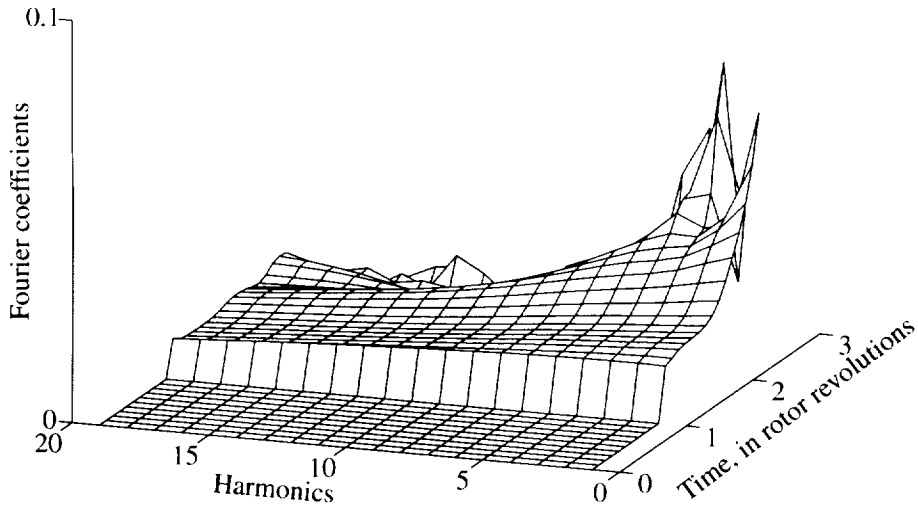

Figure 3.11: Evolution of first harmonic of V_x at tip of the first rotor inlet for small amplitude long wave length disturbance.

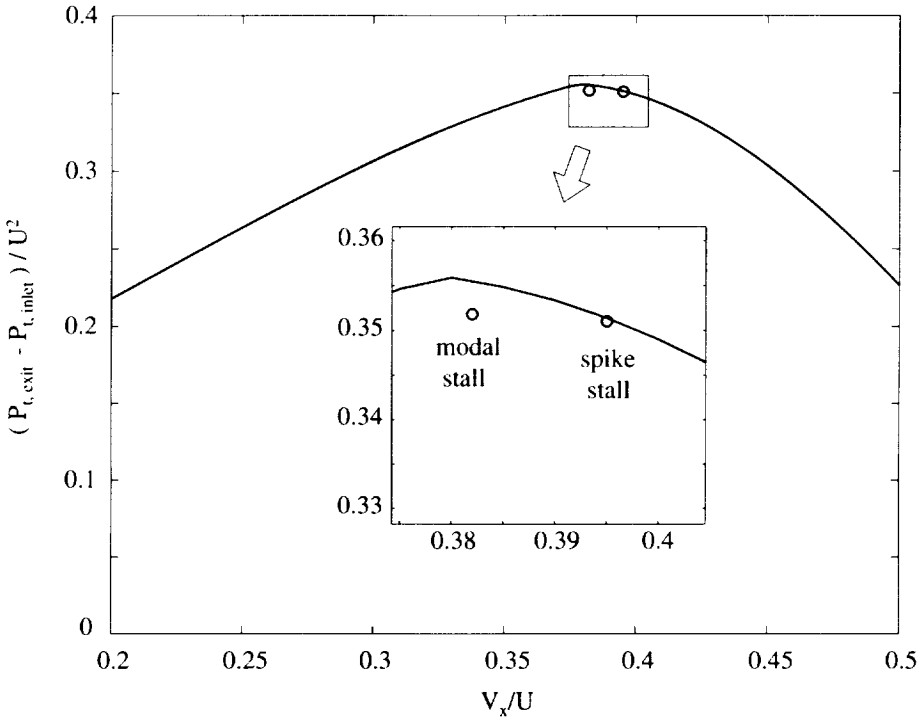

Figure 3.12: Two different stall points are calculated for spike-shaped and linear disturbances in the GE matched compressor.

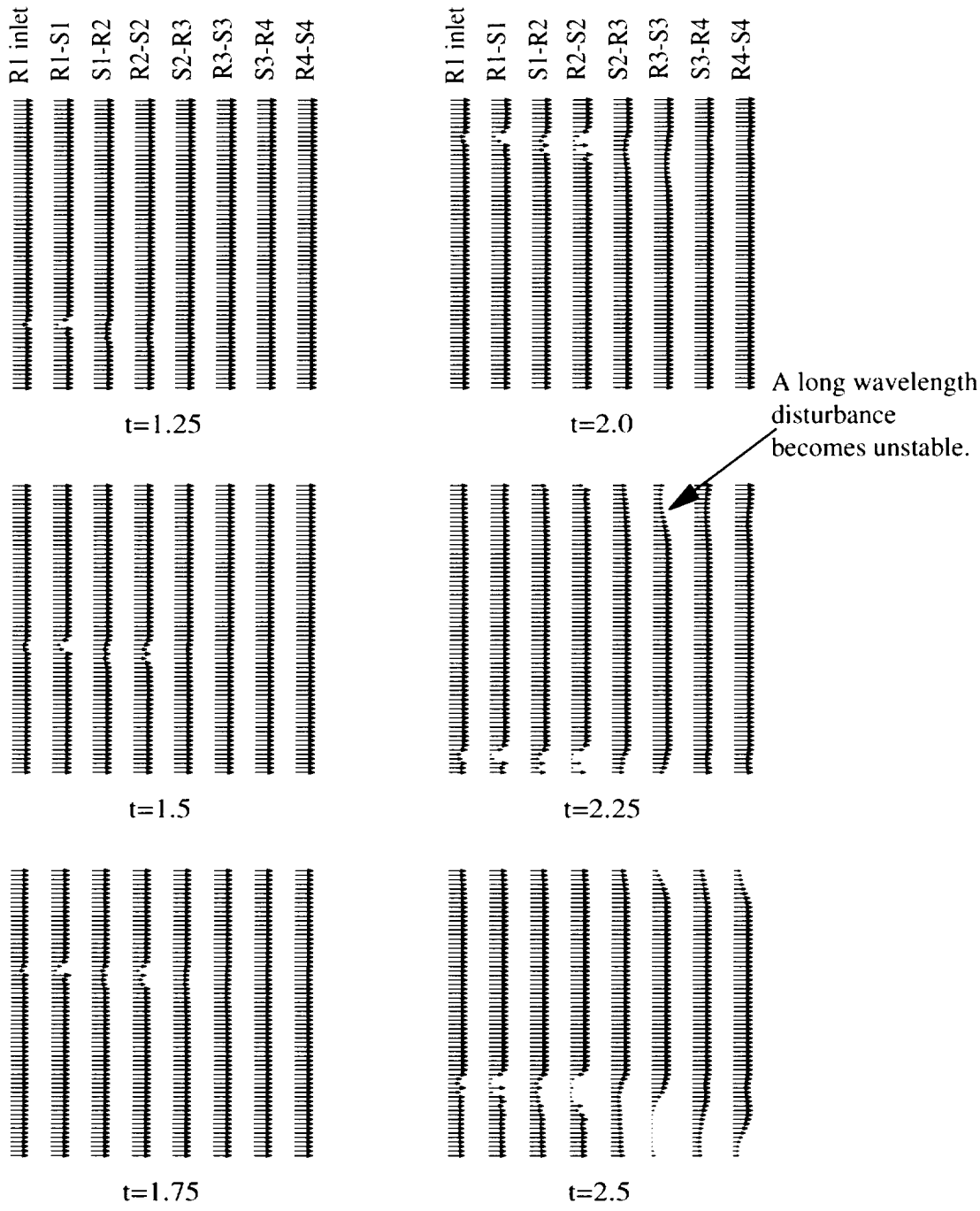

Figure 3.13: Tip Vx within eight gaps at six time instances during the development of the initial disturbance.

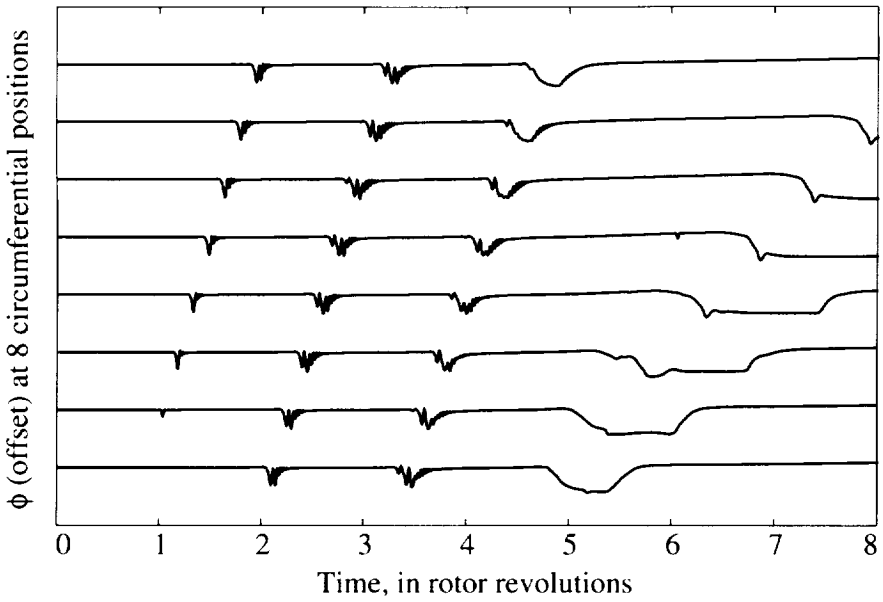

Figure 3.14: The computed tip ϕ traces from the rotor exit show the evolution of a spike-shaped disturbance. The compressor is a single-stage configuration of the GE compressor.

Since no data were taken from the rear stages in the experiment, and the data taken from the first stage cannot indicate any early development of three-dimensional long wavelength disturbances in the rear stages (due to a high decay rate in the upstream direction), it is unknown whether there is a long wavelength disturbance development prior to that of the first stage. In the simulation, the separation of the spike-shaped disturbance from an emerging long wavelength disturbance might be explained due to the relatively large differences between the rotating speed of spike-shaped disturbance (83%) and the rotating speed of long wavelength disturbance (about 20%). In the real compressor, the separation might not have happened before a large stall cell forms, because the difference of rotating speed between initial disturbance (70-73%) and final long wavelength disturbance (45%) is smaller.

The difference in the development of short wavelength disturbance during the emerging of large stall cell can be viewed only as a different route to the final stall cell. The nature of the instability is still due to the initial growth of short wavelength disturbances. The statement is supported by a numerical simulation for a single stage

configuration for the same stage in the GE compressor. The velocity traces are shown in Fig. 3.14, in which a spike-shaped disturbance clearly grows into a large stall cell. The different routes to the emergence of the large stall cell for the same stall inception mechanism will be further discussed in Chapter 5.

3.5 The GE Four-Stage Compressor, Mismatched Build

The experiment reported by Silkowski [60] shows that the growth of short wavelength disturbances can be prevented from developing into a full-span stall cell by mismatching the compressor. The compressor could operate without substantial deterioration in pressure rise, while one or several spike-shaped stall cells exist in the first stage. Each local stall cell could be viewed as a certain stage of a short wavelength disturbance during the evolution of compressor stall. This provides an opportunity to examine the behavior of short wavelength disturbances, since the flow situation is now stabilized in an equilibrium state.

The computational model was used to implement a simulation that reproduced the experimental observation, and the assessment of computed results against measured results can be on a quantitative basis. The case is ideal for assessing the current model since (1) the existence of an equilibrium state of the local stall cell pattern makes it possible to compare the structure of a spike-shaped stall cell between the results from the computation and measurements; (2) the progressive stalling characteristic provides an opportunity to assess the overall effects of local stall cells on the pressure rise characteristics.

The General Electric E^3 four-stage low-speed compressor, which has the same configuration and blading as the compressor in the previous section, was mismatched by re-staggering the rotors in stages two to four, so that the rear three stages have a lower peak pressure rise flow coefficient than does the first stage. Therefore, within a certain flow coefficient range, the first stage can operate in 'stall' while the rear

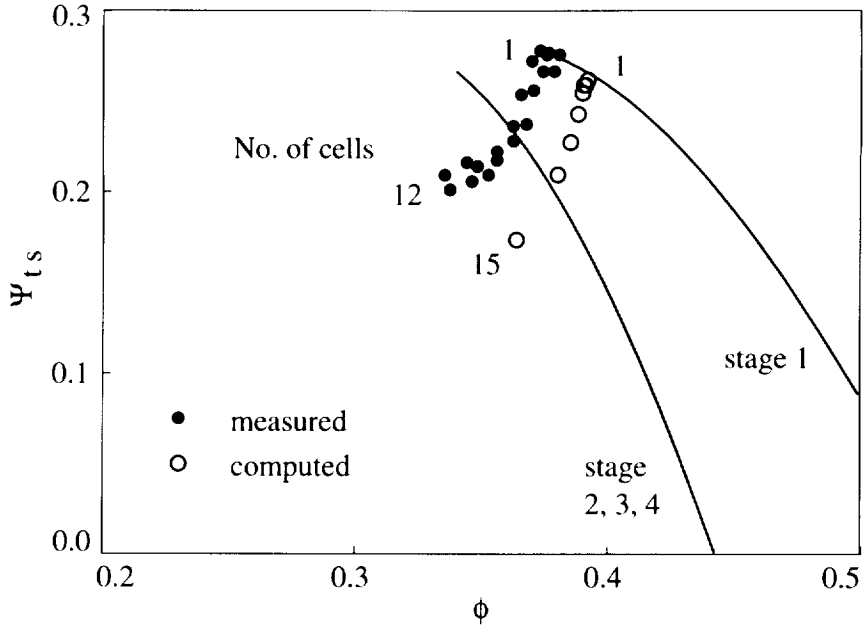

Figure 3.15: Measured and computed stage one characteristics for the GE mismatched compressor. Circles denote the progressive stall, which deviates from the axisymmetric characteristic (solid line).

stages are still well in their stable region. In this flow coefficient range, the first stage exhibits a gradual decrease in pressure rise with decreasing flow coefficient with no observable hysteresis (Fig. 1.8). This type of characteristic is often referred to as progressive stall. The number of local stall cells can vary according to the overall flow coefficient (or throttle opening). Each individual stall cell is characterized by its width (in terms of blade pitch) and the rotating speed, and these characteristics constitute the figure of merit in the assessment.

The setup of the computation is essentially the same as the case in the matched compressor situation (section 3.4). A spike-shaped disturbance (through a spike-shaped forcing lasting 0.1 rotor revolutions) is imposed in the tip region of the first rotor at a frequency of one per rotor revolution. Continuous inserting of the spike-shaped disturbance provides a source for local stall cells to be developed and sustained. The number of local cells sustained by the system depends on throttle position within the progressive stall region.

The features captured by the computational model are compared against those from experimental observation and are described below:

1. The progressiveness of the pressure rise characteristic is well captured by the model, as shown in Fig. 3.15. There is no hysteresis and the characteristic of the first stage is invariant with respect to the direction of the throttle movement. The number of stall cells varies according to the throttle position. The number of stall cells is observed in experiments to vary from one to twelve depending on the throttle position, while the computation has simulated a variation of one to fifteen for different throttle positions.

2. The size of a local stall cell is reflected in the ϕ trace. The computed width of a local stall cell, which is indicated by the ϕ trace at the first rotor inlet at the tip (Fig. 3.17) matches the measured width of a local stall cell (Fig. 3.16). The size of a computed stall cell is nearly fixed for different throttle positions, in agreement with the measurements.

3. The computed rotating speed of local stall cells (83% of rotor speed) is also comparable to the measured value of about 70% .

A summary of the comparison is given in Table 3.6.

Another observation is that the first stage stalls at nearly the same flow coefficient for both matched and mismatched arrangements. This suggests that the instability behavior in the first stage is the same for both the matched and mismatched compressors, and the presence of the downstream stages does not affect the instability of local events (i.e. when the length scale of the local stall cell does not extend beyond the physical confine of the first stage) in the first stage.

It is concluded that the model captures key experimental observations of the disturbances/local stall cells in the first stage of the GE mismatched compressor. The model captured not only the overall behavior of the stalling characteristic, but also the shape of individual local stall cells. The implication is that the behavior of short wavelength stall cells is not related to the discreteness of individual blade and detailed

flow structure in blade passages, even though the sources of initial disturbances are related to the blade passage events. In other words, the behavior, hence the development, of the short wavelength disturbances is determined by the system instead of a particular blade passage.

It is worthwhile to examine the flow structure around a local stall cell, which might explain some aspects of the behaviors of short wavelength disturbances. The three-dimensional flow structure of a local stall cell is shown in Figure 3.18. The plot reveals that the amplitude increases in the axial direction in the rotor, and decreases in the stator. The cell structure suggests the followings:

1. It is the rotor which is the most unstable component, while the stator exercises a stabilizing influence (since the disturbance amplitude decreases in the stator). The different roles played by the rotor and stator suggest that the size of a local stall cell is determined by the combined effects of the rotor and stator. For the single rotor configuration, a localized stall cell does not receive stabilizing influence from other components, so that the size will keep growing until it reaches the mass flow balance between the pressure rise produced by the rotor and the pressure drop of the throttle. Therefore it is expected that the stalling behavior of a single rotor configuration will be significantly different from that of a stage (or a multi-stage compressor).

2. The disturbance reaches its maximum amplitude in the rotor-stator gap. This observation is consistent with the conclusion made by Park [56] who found that the best sensor location for the detection of short wavelength stall inception is at the tip region of the rotor exit.

3. The downstream re-staggered stages have little effect on the instability of the first stage because the downstream blade rows see a highly damped disturbance.

The following two observations bear on the relation between the progressive stall characteristic and the varying number of localized stall cells.

1. The flow coefficient in the unstalled portion of the annulus is constant for different overall flow coefficients (before the local stall cells have filled up the whole

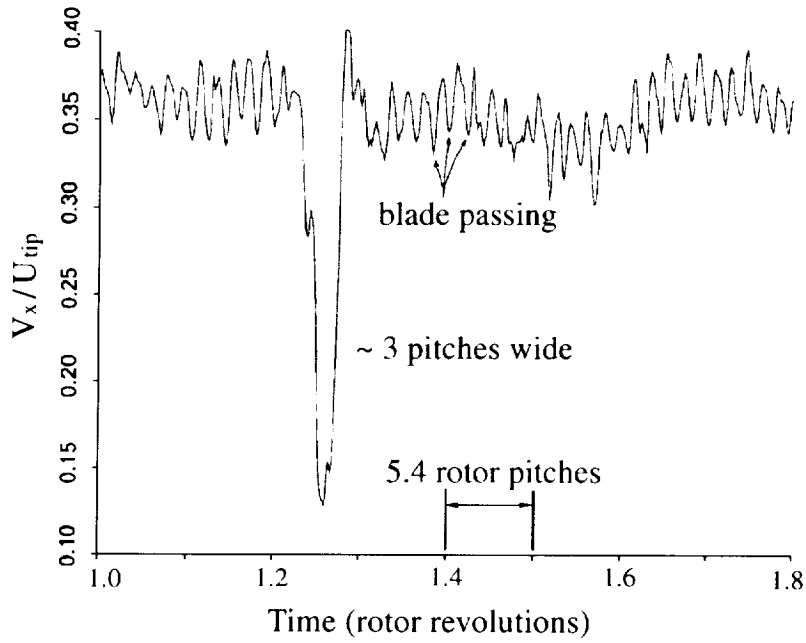

Figure 3.16: Measured velocity trace showing a localized stall cell [60].

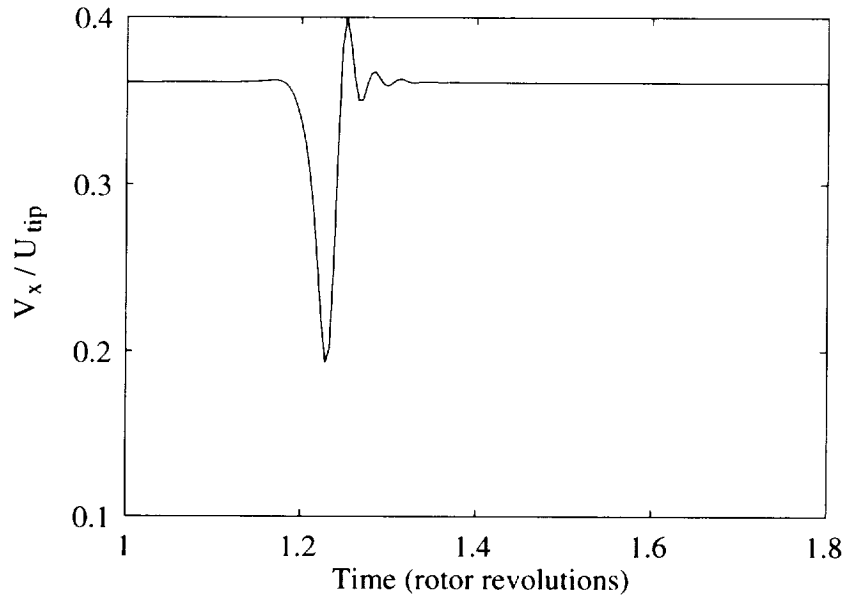

Figure 3.17: Computed velocity trace showing a localized stall cell.

Table 3.6: Summary of the comparison between computation and measurement

	Measurement	Computation
width of spike	2-3 pitches, 54 blades in rotor	1/20 annulus
rotating speed	70-73%	83%
progressive characteristic	yes	yes
Number of stall cells	1-12	1-15

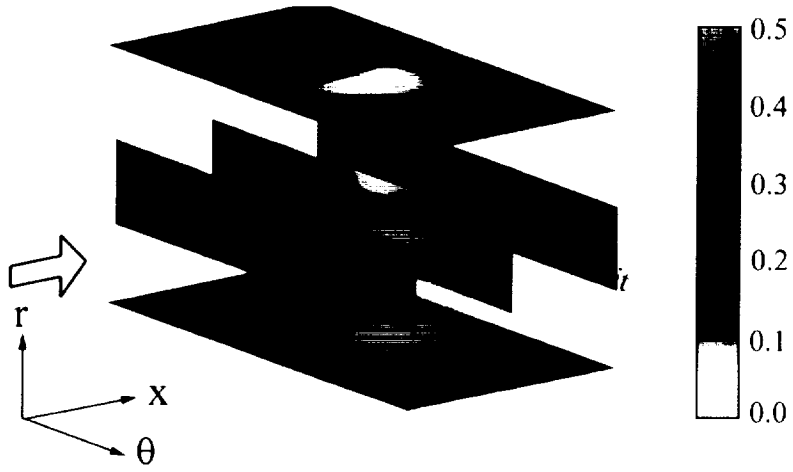

Figure 3.18: Computed flow coefficient contours of a localized stall cell in the first stage of the GE mismatched configuration. A tangential extent equal to 6 blade pitches is shown.

annulus).

2. The size (measured by flow coefficient deficit) of each local stall cell is nearly constant.

Then, the number of stall cells is

$$N_{cell} = \frac{\phi_{unstall} - \phi}{\Delta\phi} \tag{3.1}$$

where the $\phi_{unstall}$ is the flow coefficient in the unstalled portion of the first rotor; $\Delta\phi$ the overall flow coefficient deficit caused by a localized stall cell. A local stall cell in the first stage can also cause a finite decrease of pressure rise, $\Delta\Psi$. For a mismatched compressor with many stable stages, the flow coefficient is mostly determined by the stable stages. Therefore, the number of local stall cells is set by the throttle position. $\Delta\Psi$ due to a spike (local stall cell) is large enough to make room (flow coefficient drop) for another spike in the stage, the compressor could show a sudden drop of pressure rise with many local stall cells in a local stage. The large number of stall cells might then cause sufficient pressure drop, and consequently sufficient flow coefficient drop to put the whole compressor into rotating stall.

The number of stall cells can be estimated based on the above discussion. The pressure rise of the compressor with N local stall cells can be expressed as

$$\Psi = \Psi_{tt,\ stage\ 2-4} + \psi_{tt,\ stage\ 1}(\phi_{unstall}) - N_{cell}\Delta\Psi \tag{3.2}$$

Substituting for N_{cell} gives

$$\Psi = \Psi_{tt,\ stage\ 2-4} + \psi_{tt,\ stage\ 1}(\phi_{unstall}) - \frac{\Delta\Psi}{\Delta\phi}(\phi_{unstall} - \phi) \tag{3.3}$$

ϕ, flow coefficient, can be estimated by equating Ψ to the pressure drop across the throttle, $1/2\ K_t\phi^2$, and then solving the equation for ϕ. Once ϕ is solved, the number of stall cell could be calculated using Eq. 3.1. Fig. 3.19 shows the number of local stall cells calculated by Eq. 3.1 and Eq. 3.3, and also the results from the computation.

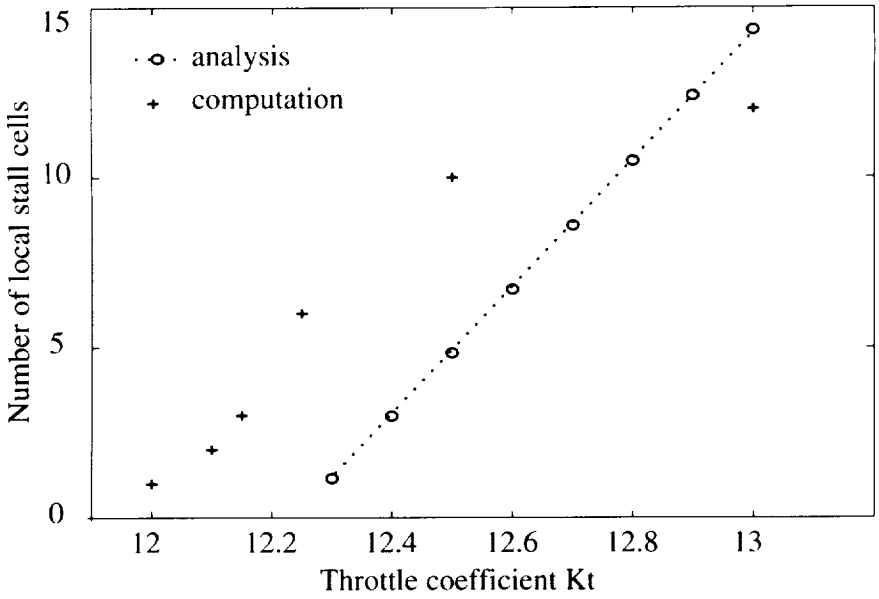

Figure 3.19: A simple analysis gives a good trend of the number of local stall cells in the mismatched GE four-stage compressor.

The trend is well captured by the analysis. As the number of stall cells reaches a certain value (which is ten in this case), the trend of measurement deviates from the original direction. This is due to the fact that the unstalled flow coefficient, $\phi_{unstall}$, in the first rotor could not be held as a constant; since the annulus is filled with local stall cells. Thus the assumptions (the flow coefficient in the unstalled part is a constant value) in the analysis break down as the number of local stall cell becomes large.

The analysis shows the relation between progressive stall characteristic and local stall cells. The gradual decrease of pressure rise is due to increase of number of local stall cells.

3.6 Effects of IGV stagger on Stalling Behavior in the First Rotor

The assessment of the impact of IGV stagger on compressor stalling behavior is motivated by the recent experimental observation of "unique rotor tip incidence" as a spike stall criterion [5]. Camp and Day found that when the IGV stagger angle on a four-stage compressor was reduced by 5°,10°, 15°, and 20° (the corresponding loading on the first rotor went up), the compressor showed spikes as its stall inception type. However, when the IGV stagger angle increased (so the loading on the first rotor decresed), the stall inception switched to a modal type. The most interesting result from their observations is that the rotor tip incidence has a constant value of zero when the compressor showed short wavelength stall inception (Fig. 3.20). Since the rotor incidence angle can be a measure of loading at rotor tip, the unique rotor tip incidence is equivalent to the "unique rotor tip loading".

A similar set of simulations was performed based on the GE compressor for a set of different IGV stagger angles. Since different compressors are compared here, the following two features are the figures of merit of this comparison.

1. The type of stall inception switches when the loading (IGV stagger) of the first rotor changes.

2. A unique rotor tip incidence exists at which the compressor shows stall through short length scale disturbances.

Since the available characteristic of the compressor is for the design IGV stagger angle, the characteristics at other IGV staggers have to be estimated. The way used to estimate the characteristics for different IGV stagger angles (or different inlet flow angles) consists of the following steps:

1. A mean-line method was calibrated to give a correct characteristic at the peak for the design IGV stagger.

2. The calibrated mean-line method was used to calculate the characteristics for

different inlet flow angles (corresponding to different IGV stagger angles). The peaks of these characteristics are recorded.

3. The characteristics were obtained by shifting the measured characteristic to match the peaks obtained from the previous step.

The procedure is not intended to be rigorous since the mean-line method is also based on correlation, however it takes advantages of the available measured characteristics and the existing correlation method. Figure 3.21 shows the characteristics obtained using the procedure for different IGV staggers.

Once the pressure rise characteristics for different IGV staggers are obtained, simulations were performed to determine the stall points and their types. The forcing impulses in these simulations were kept at the same value as before (section 3.4 and 3.5).

Figure 3.21 shows the stall points, their inception types, and their corresponding rotor tip incidences for different IGV stagger angles. The trends are similar to the experimental observation, which is shown in Figure 3.20. First, the stall inception switches from spike to modal as the IGV stagger angle is increased (so the first rotor is unloaded). For the high IGV stagger situations, which correspond to low rotor loading, the stall inception type is of the long wavelength type. For the low IGV stagger situations, where the rotor is highly loaded, the stall inception type is of spike type. The most remarkable feature is that the first rotor tip incidence at which spike stalling occurs remain is $-3.5°$. Therefore two key features were well captured by the model.

One additional observation is that all the modal stall points line up vertically. This is because these stall points are determined by the downstream stages; therefore the stall flow coefficient is fixed by the downstream stages.

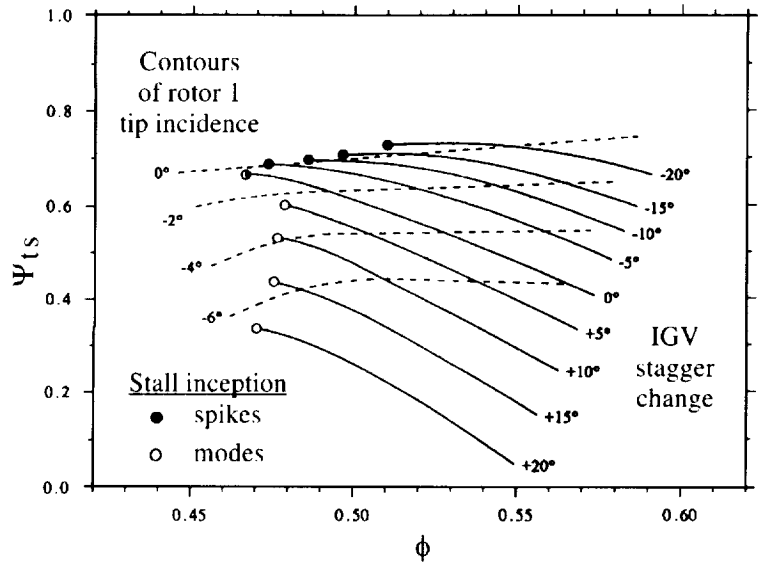

Figure 3.20: First stage characteristics with the stall point and inception type indicated for different IGV staggers. Measured by Camp and Day [11].

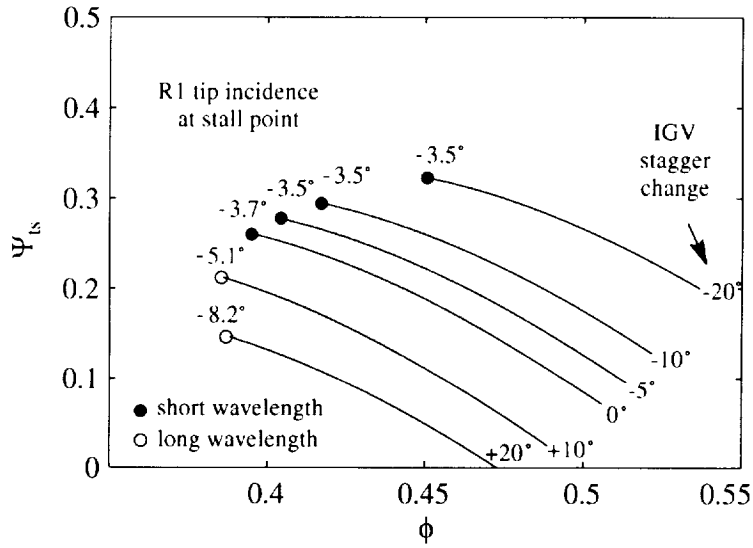

Figure 3.21: First stage characteristics with the stall point and inception type computed for different IGV staggers.

3.7 Summary

The assessment presented in this chapter demonstrated the adequacy of the model for capturing the stalling behavior associated with short wavelength disturbances in a multistage compressor. The key results in this chapter are

1. The model gave an accurate description for the behavior of long wavelength disturbances in multistage compressors.

2. The model captured the key observations associated with short wavelength stalling behavior in a multistage compressor.

Therefore, the smeared-out body force representation is sufficient to describe stalling behavior of both short and long wavelength types. The model is now ready to be used to explore the parametric dependence of stall inception in terms of some design parameters. This will be presented in the next chapter.

Chapter 4

Parametric Studies of the Short Length Scale Stall Inception

The parametric studies considered in this chapter address the following two issues.

The sensitivity of the model to input parameters There are two inputs od which we don't have a quantitative knowledge so far. One is the initial disturbance (amplitude, location, etc). The other is the blade row performance characteristic to the left of the peak. The sensitivity of these parameters will be examined in this chapter.

The effects of design parameters on short wave length stall inception It was decided to focus on blade row gaps only. This parameter is the one that does not require redesign of a blade row. Other parameters (e.g. hub-to-tip ratio, blade radial loading profile, etc.) would require the implementation of the model in conjunction with other design tools, like stream-line-curvature, full three-dimensional code, etc. since the body force for the modified blade row has to be generated through these tools.

To clarify the first issue, the following four parameters will be investigated.

1. Type of disturbances. Three types of initial disturbance are studied: small amplitude disturbance, spike-shaped disturbance at tip, and spike-shaped disturbance at hub.

2. Amplitude of disturbances. The stall point and its type will be calculated for different amplitude of initial forcing. The amplitude effects elucidate the non-linearity of short wavelength stall inception. A specific question to be answered is whether the amplitude threshold of short wavelength stall inception exists.

3. Axial location of disturbances. The simulation is performed for the case that the initial disturbance is inserted in a rear stage, to identify the most unstable blade row in a multi-stage compressor.

4. Left side axisymmetric pressure rise characteristic. The unstable portion of the characteristic cannot be measured, and has not been well calculated. Several simulations are performed for varying axisymmetric pressure rise characteristic to the left of the peak.

The second issue, the impact of gaps on instability behavior, is addressed through varying three intra-blade-row gaps: IGV-R1, R1-S1, and S1-R2 gaps. These gaps reflect the degree of coupling between blade rows, and thus are important design parameters.

4.1 Type of Disturbance

It has been shown that small amplitude long wavelength disturbances lead to modal stall inception, while spike-shaped forcing in the tip region leads to short wavelength stall inception. It is reasonable to ask what will happen if the spike-shaped forcing is located in the hub region. This relates to the question of why spikes usually emerge in the tip region.

A simulation was performed in which the spike-shaped force field was located in the hub region (referred to as hub-spike). The result, along with the result of inserting a disturbance in the tip region (referred as tip-spike), is presented in Fig. 4.1 in which the modal stall point is used as a reference stall point. The decrease in the stall

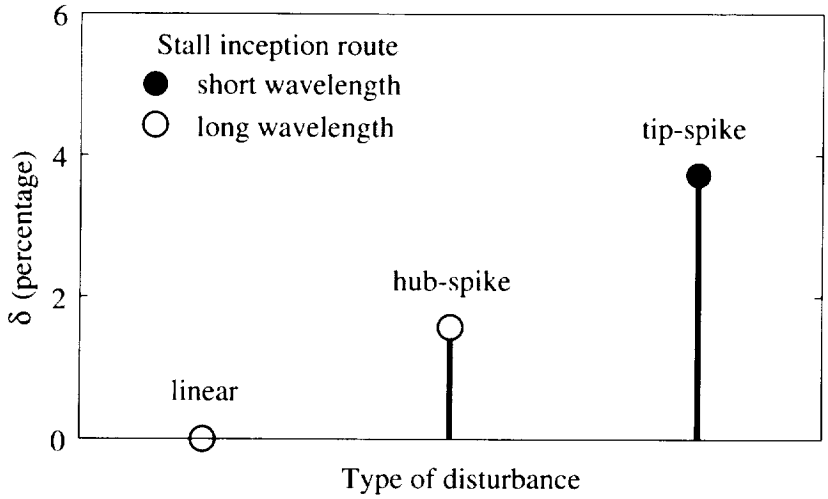

Figure 4.1: Changes in stall point and inception type for different type of inposed disturbances.

margin is defined by the following equation.

$$\delta = \frac{\phi_{stall} - \phi_{modal\ stall}}{\phi_{modal\ stall}} \tag{4.1}$$

The results show that for the same amount of forcing, the tip-spike forcing leads to short wavelength stall inception at a higher flow coefficient, while the hub-spike forcing leads to long wavelength stall inception at a flow coefficient near the modal stall point. The conclusion is that the short wavelength disturbances are better supported by the tip region of this compressor than that by the hub.

The different effects of forcing at the tip and hub are related to the local radial equilibrium and will be further explored in Chapter 5.

4.2 Amplitude of disturbance

It has been shown that the short wavelength stall inception has to be initiated by a spike-shaped disturbance. Experimental observations also show that this type of disturbance exists prior to stall. However, it is hard to extract the source of these localized disturbances and the amplitude of the source, since the nature of these

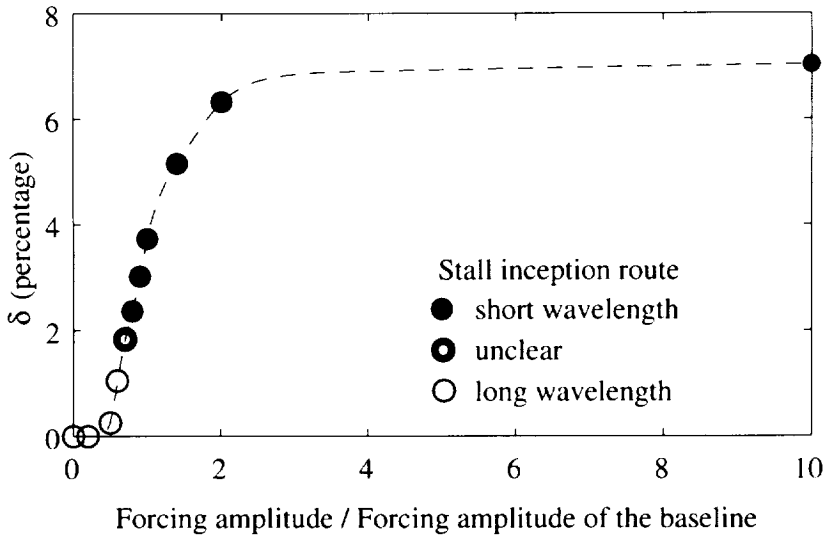

Figure 4.2: Effects of initial spike forcing amplitude on stall point and inception type.

disturbances has not been identified yet. Because the amplitude used in the baseline simulation is somewhat arbitrary, it is necessary to examine the effects of the forcing impulse amplitude on stalling behavior.

The simulations are performed for different forcing strengths at the same location near the tip. The results are plotted in Figure 4.2. The amplitude is normalized by the forcing amplitude used in Chapter 3. For small amplitude forcing, the instability point goes to the modal stall point. There is a transition region where the instability point is sensitive to the forcing amplitude. The transition region corresponds to one with a 20% to 60% (the value of the baseline is 30%) loss on one rotor blade passage pressure rise capability for 0.1 rotor revolutions. It is reasonable to say that typical blade passage events (e.g. tip vortex) cause part of a blade passage to lose it pressure rise capability, therefore these events are expected to have significant impact on the instability point. When forcing amplitude increases further, the forcing seems to saturate the system, and the stalling flow coefficient is not sensitive to these very large forcing amplitudes.

The set of simulations shows that an amplitude threshold exists for instability through short wavelength disturbances to occur, and therefore this type of stall in-

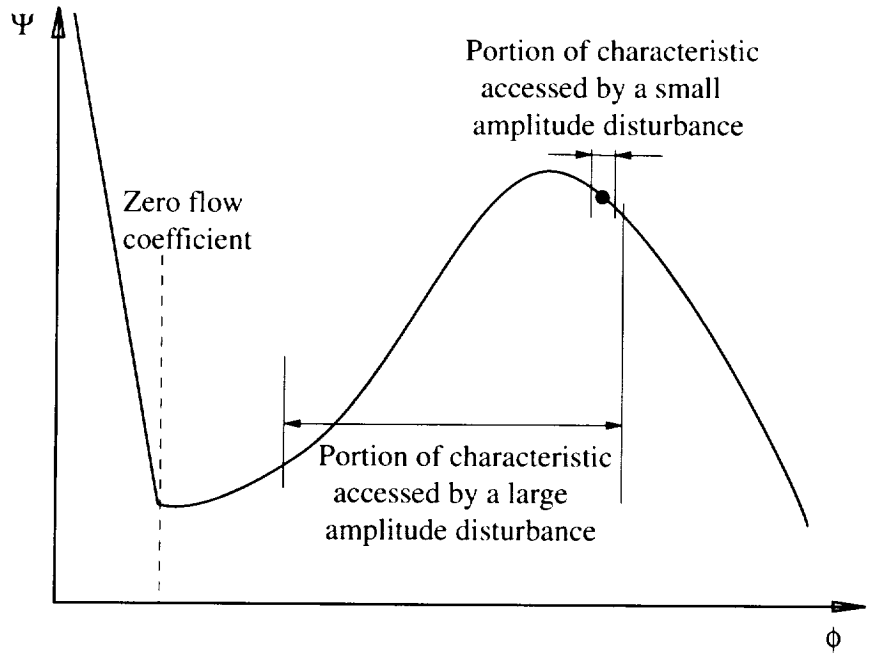

Figure 4.3: Effects of disturbance amplitude. A large amplitude disturbance could cause blade row stall when the overall flow coefficient is in negative sloped region.

ception is nonlinear in nature.

Fig. 4.3 illustrates how a large amplitude disturbance could induce stall at a higher flow coefficient (point to the right of the peak pressure rise point). A small amplitude disturbance can only access a small portion of characteristic; therefore the slope determines the instability. If a disturbance has large amplitude, then a large portion of characteristic could be accessed by the disturbance, so that a large portion of characteristic would play an aggregate role on the instability of the disturbance. As shown in Fig. 4.3, the low flow coefficient region has a lower pressure rise, and the compressor could stall even when the overall flow coefficient is still in the negatively sloped region.

Using the compressor characteristic in Fig. 4.3, we can explain why a spike-shaped forcing cannot increase the stalling flow coefficient further after it reaches a certain amplitude. The resulting disturbance amplitude in velocity is produced by the combined effects of the disturbance forcing and the body force that responds to the velocity disturbance. For the duration that a large forcing is imposed on a rotor,

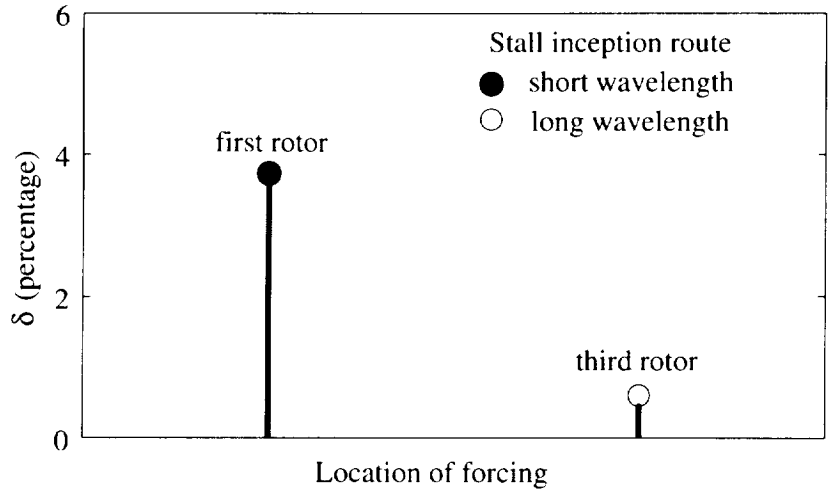

Figure 4.4: Changes in stall point and inception type with location of initial spike.

a velocity deficit is created with increasing magnitude. At the same time, the blade row begins to respond to the velocity deficit. When the flow deficit is large enough so that local flow reversal occurs, the blade row responds to the reverse flow with a steep increase in the magnitude of the forward force (Fig. 4.3), which would offset almost any increasing of imposed forcing. In other words, the amplitude of disturbance created by an imposed forcing is limited by the steep pressure rise characteristic in the reverse flow region, so the flow in the compressor will not respond to further increase in imposed forcing.

4.3 Axial location

For all these previous simulations, the forcing that initiates the disturbances is always located in the first rotor. However, all the four stages are identical. This raises a question whether a spike can emerge from another rotor if the forcing is applied to that rotor. It is thus of interest to examine the situations for which the forcing is inserted in the tip region of a rear stage.

A simulation is performed for the situation where the forcing is applied to the third rotor. The stall point is near the modal stall point and the inception type is

of long wavelength, although the stage performance and the forcing are the same as those for the first rotor, and the V_x profile at the third rotor inlet is similar to that of the first rotor. This does not support the argument by Camp and Day [5] who argued that the reason why spikes usually emerge in the first stage is because the first rotor has a higher loading than the others. The issue will be further explored in the latter part of the chapter.

4.4 Rotor Characteristic to the Left of the Peak Pressure Rise

The instability associated with short wavelength disturbances is non-linear. As illustrated in Fig. 4.3, a large portion of the characteristic participates in the instability process. Further, little knowledge is available for estimating the unstable portion of the characteristic. It is thus necessary to examine the effects of a variation in the portion of the characteristic to the left of the peak pressure rise.

Five rotor characteristics, shown in Figure 4.5, were used to calculate the progressive stall region for the GE mismatched compressor. Characteristic (I) is the baseline that has been used in the previous chapter. Characteristic (II) to (V) all have the same stage characteristic and stable portion of rotor characteristic. Characteristic (II) has a flat portion at very low flow coefficient, and its other portion is essentially the same as the baseline. The simulation yields similar results for Characteristic (I) and (II), especially, their stall points are almost indistinguishable. This indicates that the characteristic in the very low flow coefficient region does not affect the short wavelength disturbance. That is understandable since the disturbance does not reach that far into the region where flow coefficient is below 0.1.

Characteristic (III) extends the fitted stable portion to the zero-slope point. The results show that the stalling flow coefficient of Characteristic (III) is noticeably lower than that of (I)'s, and indicates that the characteristic around the peak has significant impact on the instability. The stall point and its progressive stall characteristic are

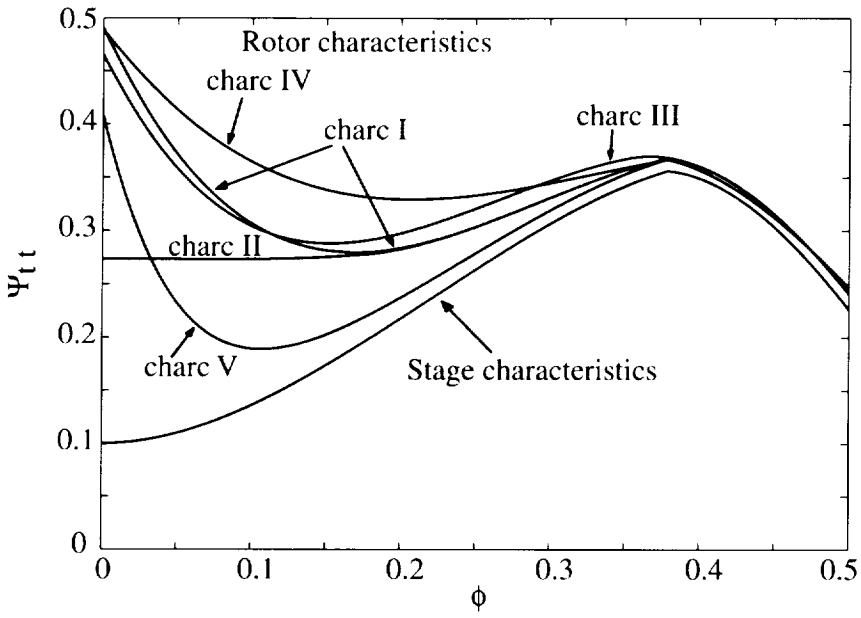

Figure 4.5: Several different left side rotor characteristics was used for the study.

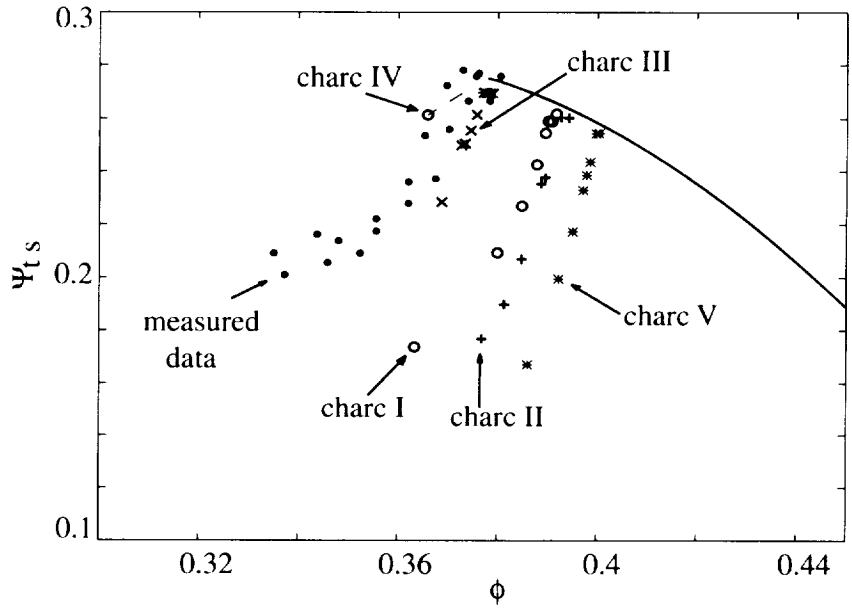

Figure 4.6: Computed results of stall characteristics for mismatched compressor with different left-side characteristics.

also the closest to the measured data among the five chosen characteristics.

Reducing the pressure rise in the unstable portion, Characteristic (V), increases the stall flow coefficient, and makes the progressive stall characteristic steeper. It is proposed that the progressiveness of stall characteristic might disappear (become vertical) if the unstable portion of the characteristic were lower than Characteristic (V).

Characteristic (IV) is nearly flat for the flow coefficient less than the peak point. In this case, a part span stall cell can be sustained only when the flow coefficient is in the positively sloped region in which modal waves would have grown if the downstream stages were not presented. This case indicates that a rotor with a flat characteristic to the left of the peak does not support short wavelength disturbances.

These results show that the unstable portion of the characteristic does impact the instability point of short wavelength disturbances, and that the performance near the peak appears to have the largest impact. Within a wide range, the difference in the characteristic to the left of the peak does not change the nature of short wavelength stall inception. The unstable portion of the characteristic that is generated based on current (though limited) knowledge can thus be used to study the parametric trends of short wavelength stall inception.

4.5 Intra-Blade-Row Gap

Since the short wavelength disturbance has a high decay rate in the axial direction, the intra-blade-row gap, which is considered small for long wavelength disturbance (Dunham, 1964), becomes large for short wavelength disturbances. It is thus likely that the gap size has a strong impact on the stall inception through short wavelength events. Effects of three gaps, IGV-R1 gap, R1-S1 gap, and S1-R2 gap, (Figure 3.7), were examined. The calculations are based on the GE four-stage compressor, matched build, with different intra-blade row gaps, and the forcing imposed on the first rotor is kept the same as the forcing used in Chapter 3. The results on the stability point and its type are shown in Fig. 4.7.

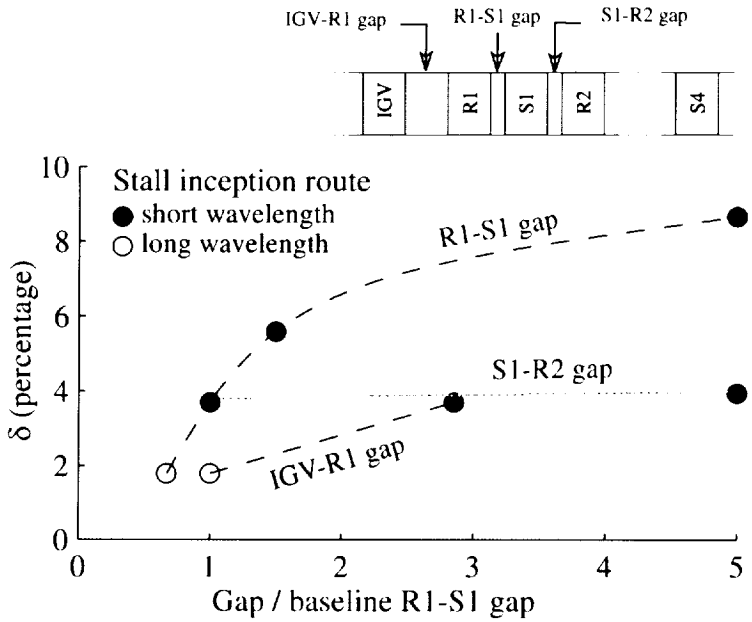

Figure 4.7: Effects of IGV-R1, R1-S1, and S1-R2 gap lengths on stall point and inception type.

Increasing of the R1-S1 gap destabilizes the short wavelength disturbances, while decreasing of the gap stabilizes the short wavelength disturbances. Further decreasing the gap can switch the stability type from short wavelength disturbance to long wavelength disturbance. Varying the IGV-R1 gap shows a similar trend as that of the R1-S1 gap. However, increasing the S1-R2 gap shows no visible effect on the stall point and its inception type.

These trends can be explained by the three-dimensional structure of a local stall cell (Fig. 3.18). The maximum amplitude of a local stall cell occurs at the first rotor exit (i.e. the R1-S1 gap region); it is thus not surprising that the size of the R1-S1 gap has the strongest impact on the instability point and behavior. The size of the S1-R2 gap has minimal impact as disturbances are expected to be damped there.

The above results suggest that the instability caused by short wavelength disturbances be determined by a *component group* that includes a rotor and its neighboring stators. From the component group argument, it is expected that any change of blade rows and gaps in the component group could change the instability of the component

group. The "component group" concept does not give a direct stall criterion, but it is useful to point out the relevant components which directly affect the growth or decay of short length scale disturbances.

4.6 Summary

The influence of several parameters on instability inception has been examined in this chapter. The computed results show that:

1. A spike-shaped disturbance with an amplitude above a threshold is necessary to initiate the short wavelength stall inception. Above the threshold, the value of the initial disturbance does not change the type of inception, however it does change the instability point.

2. A spike-shaped disturbance in the tip region is better sustained by the system than one at the hub.

3. Within a wide range, the unstable portion of characteristic does not change the nature of stall inception, although it can change the instability point.

4. Closing the rotor-stator gap and IGV-rotor gap suppress short wavelength disturbances in the first rotor.

To enable accurate prediction of the instability point using the model, the following inputs have to be available.

- An adequate description of the unstable portion of characteristic
- The typical disturbance type and amplitude.

Such information is not generally available. Without such information, the primary benefit of the model can be viewed as producing an understanding of the controlling trends of the parameters that affect the stall inception through short wavelength disturbances.

The results from assessing the influence of the gaps reveal the importance of the blade row coupling in the instability of short wavelength disturbances. From the observation, a "component group" concept is proposed, which states that the instability for short wavelength disturbances is determined by a component group that includes a rotor and its neighboring stators.

Chapter 5

Additional Physical Aspects of Short Wavelength Stall Inception

The following topics will be addressed in this chapter: (1) clarification of some physical aspects which are not modeled in the calculations, (2) Physical mechanisms associated with short wavelength stall inception are discussed, (3) possible routes to formation of rotating stall cell, and (4) a hypothesis of the link between design flow coefficient and stall inception type based on the observation of the compressor stalling data in public domain.

Some specific questions are:

1. Does swirl sensitivity change the nature of stalling behavior?
2. What is the physical origin of the spike-shaped disturbances?
3. Why do short wavelength disturbances tend to localize in the tip region?
4. Is flow three-dimensionality needed to sustain short wavelength disturbances?
5. What constitutes the simplest model for an adequate description of short wavelength disturbance?

The first section clarifies the effects of swirl sensitivity which is not modeled in the calculation. Section 2 discusses possible physical origins of the imposed spike-shaped disturbances. Section 3 explains the importance of three-dimensionality to

the growth of short length scale disturbances. Section 4 presents arguments to show that the model constitutes the simplest model needed for an adequate description of the short wavelength disturbances. The final two sections propose two hypotheses: (1) there are several routes of rotating stall development after a localized disturbance starts to grow; and (2) compressors with low flow coefficient design tends to stall through localized short length scale disturbances.

5.1 Effects of Swirl Sensitivity

Swirl sensitivity, which is neglected in the simulations for the GE compressor, refers to blade row characteristics being influenced by change of inlet swirl angle. It does not appear to change the nature of the phenomena in the GE compressor. A way to assess effects of neglecting swirl sensitivity is to examine the pressure rise across a blade row with and without swirl sensitivity around a spike-shaped local stall cell in the GE mismatched compressor.

Figure 5.1 shows the flow coefficient distribution and the flow angle distribution at the inlet to the first rotor where localized stall cells are sustained. The disturbance (a localized stall cell) has the strongest amplitude in the tip region; thus if swirl has any impact, it would be in the tip region (Fig. 5.2). A pressure rise characteristic in terms of flow coefficient can be translated into pressure rise vs. relative flow angle of the rotor. The pressure rise due to the inlet flow coefficient can be estimated based on the inlet ϕ (swirl is removed) or the inlet ϕ and flow angle β. The results in Fig. 5.3(a) show the comparison between the pressure rise calculated based on the inlet ϕ and that based on the inlet ϕ and β around a local stall cell. The shapes of the pressure rise distributions are similar, and the error of total pressure rise deficit of the local stall cell caused by ignoring the inlet swirl is about 10% of the total pressure rise deficit caused by the spike-shaped stall cell. The total pressure rise deficit measures the force which sustains a disturbance. It is therefore concluded that the swirl sensitivity will not change the nature of the stalling behavior seen in the GE compressor.

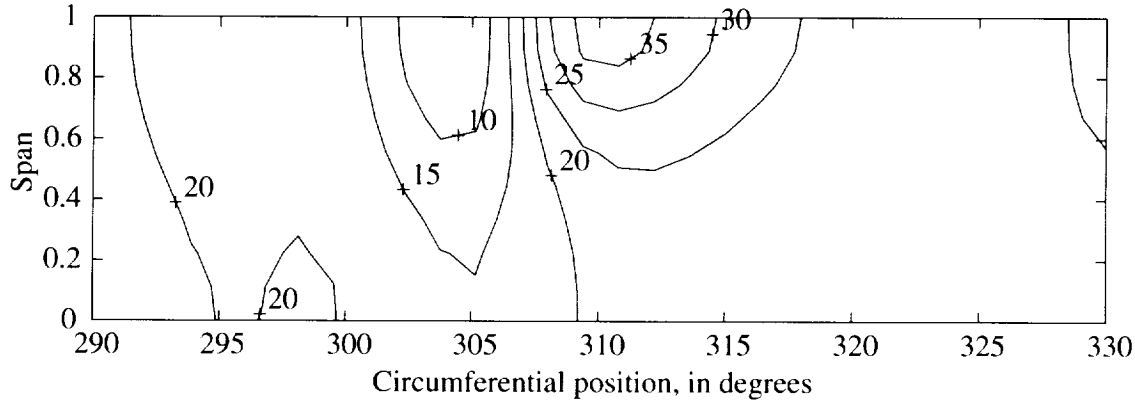

a) Tangential flow angle contours

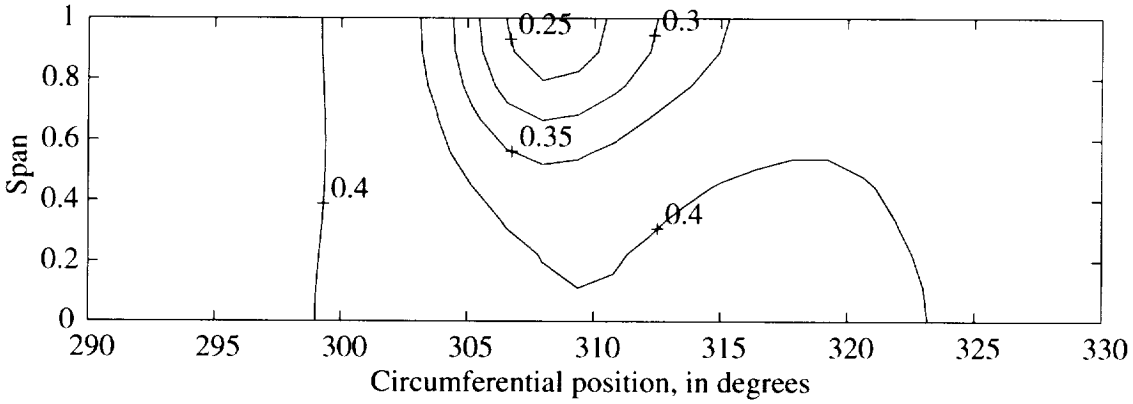

b) Flow coefficient contours

Figure 5.1: Flow coefficient and flow angle distribution at the inlet of the first rotor.

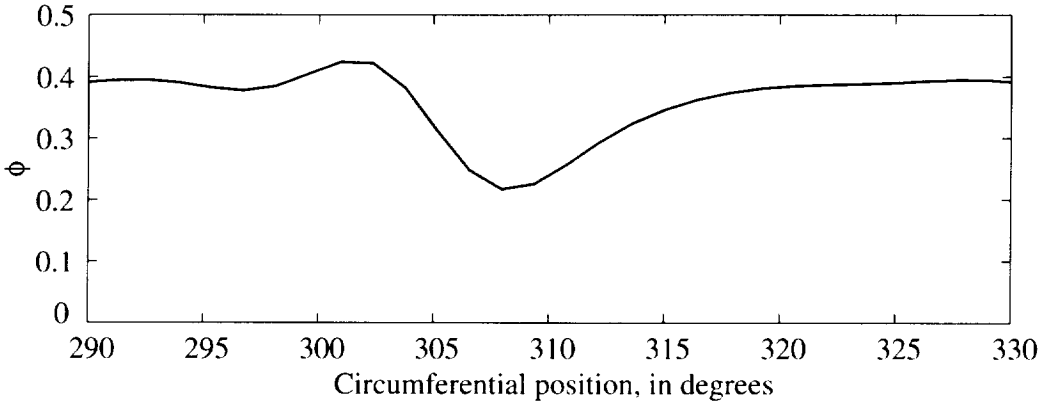

a) Tip ϕ at rotor inlet

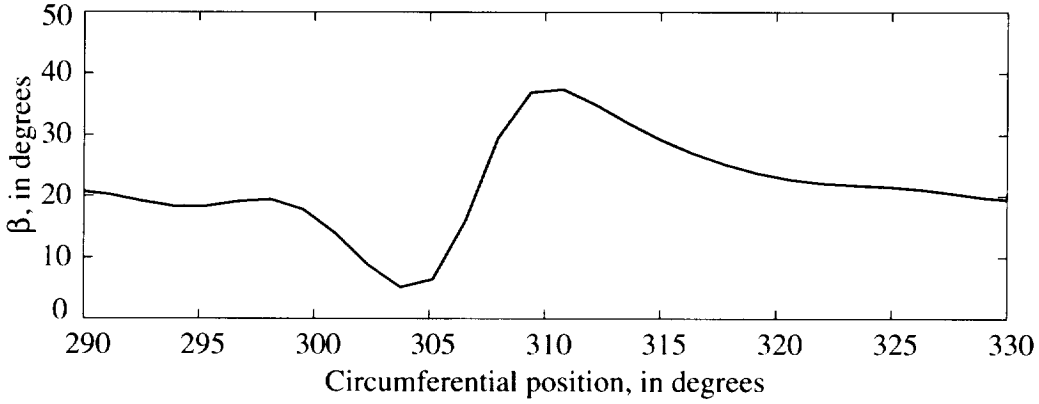

b) Tip β at rotor inlet

Figure 5.2: Flow coefficient and flow angle distributions at tip of the first rotor inlet.

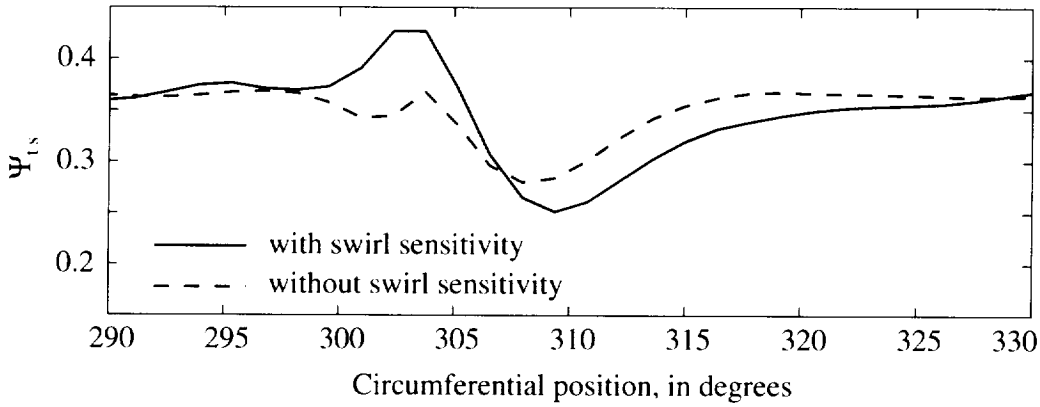

a) Pressure rise rise across the rotor with and without swirl sensitivity

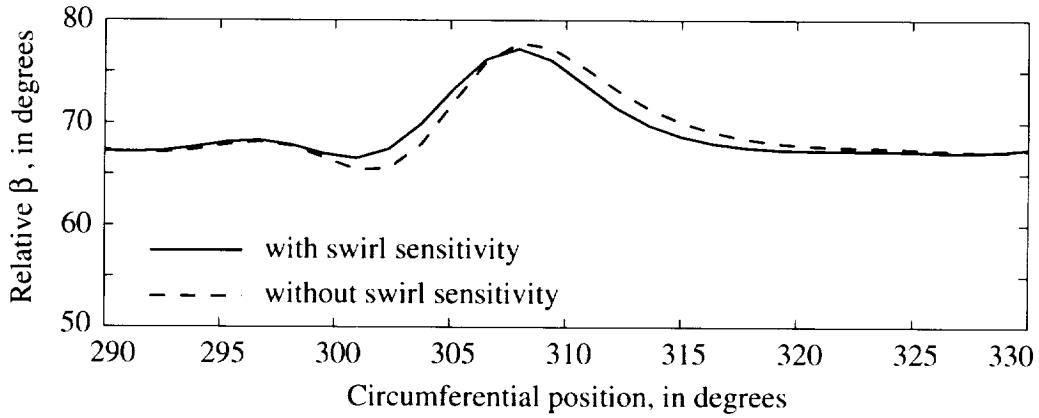

b) Relative flow angle distribution at the rotor inle.

Figure 5.3: (a) Effects of inlet swirl on the pressure rise; (b) Effects of inlet swirl on the relative flow angle.

The reason that the inlet swirl has relatively less effects on the rotor loading can be explained by examining the relative flow angle distribution at the rotor inlet, given by

$$\tan \beta_{relative} = \frac{U - V_x \tan \beta}{V_x}$$

Fig. 5.3(b) shows the relative flow angle distributions calculated using the above equation with a β using actual value and with zero (ignoring the swirl sensitivity). The relative flow angle in the rotor inlet is not sensitive to the inlet swirl, due to the compressor's low stalling flow coefficient, because $\tan \beta_{relative}$ is more sensitive to the denominator (V_x) than the numerator ($U - V_x \tan \beta$) which is dominated by U.

5.2 On the sources of the forcing impulses

The imposed disturbance through forcing is an important part of the model in the sense that a short wavelength stall inception has to be initiated by a finite amplitude spike-shaped disturbance. However, as the forcing is an input during the simulations, its magnitude is somewhat arbitrary. To estimate the appropriate magnitude of the forcing, it is useful to look at its physical origin.

The source of initial disturbance is viewed as the consequence of blade passage events, for example tip vortex behavior. Hoying et al [34] performed isolated rotor simulations at stall which suggested that the motion of the tip vortex in and out of a rotor passage was responsible for producing spike-shaped disturbances. It would seem that discrete blade passage events are the likely sources for short length scale disturbances. If so, then its magnitude would be a fraction of the total blade force of the blade passage.

Park [56] analyzed the data taken by (1) pressure transducers at the casing of the first stage rotor exit, (2) hot-wire anemometers in the tip region of the first stage rotor exit, (3) pressure transducers at the casing of the first stage rotor inlet, and (4) hot-wire anemometers in the tip region of the first stage rotor inlet. He found that the pressure transducer in the tip region of the first rotor exit exhibited short wavelength disturbances earlier than other locations. This seems to indicate that

the blade passage event first occurs (or reaches a measurable amplitude sooner) at the rear part of a blade passage. Postprocessing of numerical simulations have been focused on the flow at the leading edge, and it will be interesting to examine the flow field from the leading edge to trailing edge obtained from N-S simulation.

5.3 Three-dimensionality in the short wavelength stall inception

The purpose of this section is to explain why a three-dimensional model is essential to describe short wavelength stall inception. Two additional physical aspects are included in the current model that are not captured by the two-dimensional analysis. The first is an additional length scale in the spanwise direction, so that the flow disturbances could grow and decay spatially at a faster rate in the blade-free regions as well as in blade row regions, relative to two-dimensional motion. Introducing an additional spanwise length scale reduces the coupling between blade rows, and disturbances can exist locally (around a blade row). A locally unstable blade row, usually a rotor row, could thus stall earlier than the compressor as a whole, so the compressor could stall (through the non-linear mechanism described earlier) in the negatively sloped region of its characteristic. The second is the centrifugal effect (i.e. V_θ^2/r term in the radial momentum equation) on the localization of spike-shaped disturbances in the tip region.

The following two cases are designed to clarify the role of three-dimensionality in the stalling process. In the first case all the radial variation in the governing equation set is removed, and the compressor is represented by multiple rectilinear cascades. The flow in that case is three-dimensional but without the centrifugal effect (V_θ^2/r). The second case is that of a two-dimensional compressor.

5.3.1 Rotating Stall Inception in a Compressor Represented by Multi-rectilinear-cascades

In this case, the governing equations are Euler equations in Cartesian coordinates. The blade rows are represented by rectilinear cascades (Fig. 5.4). Periodic boundary conditions are imposed at the ends of the computational domain in the tangential direction. A compressor using multi-rectilinear-cascade representation does not have any bias in its spanwise direction, therefore the 'hub' and 'tip' have the same response to disturbances. The stall point and its type are indicated in Fig. 5.5, along with the stall points initiated by hub-forcing and tip-forcing (see Chapter 4). The stalling flow coefficient calculated using multi-rectilinear-cascade representation is located roughly half way between the stall points caused by tip-forcing and hub-forcing in the compressor based on blade row by blade row representation presented in Chapter 4. The stall inception type is of long wavelength type.

The multi-rectilinear-cascade representation removes centrifugal effect term, V_θ^2/r, in the spanwise (radial) direction. For a high hub-to-tip ratio compressor, like the GE compressor, the geometry variation along the radius is small and can be ignored. The results thus imply that the centrifugal force causes a bias of the system towards sustaining short wavelength disturbances in the tip region. This explains why the GE compressor always picks up localized disturbances in the tip region.

The multi-rectilinear-cascade representation gives the stalling flow coefficient 2.5% higher than that of modal stall point. The next case, two-dimensional representation of the GE four-stage compressor, will show that finite amplitude localized disturbances are suppressed by the system, and the two-dimensional system stall through modal waves. Therefore the 2.5% increase of stalling flow coefficient is due to the additional length scale in the radial direction.

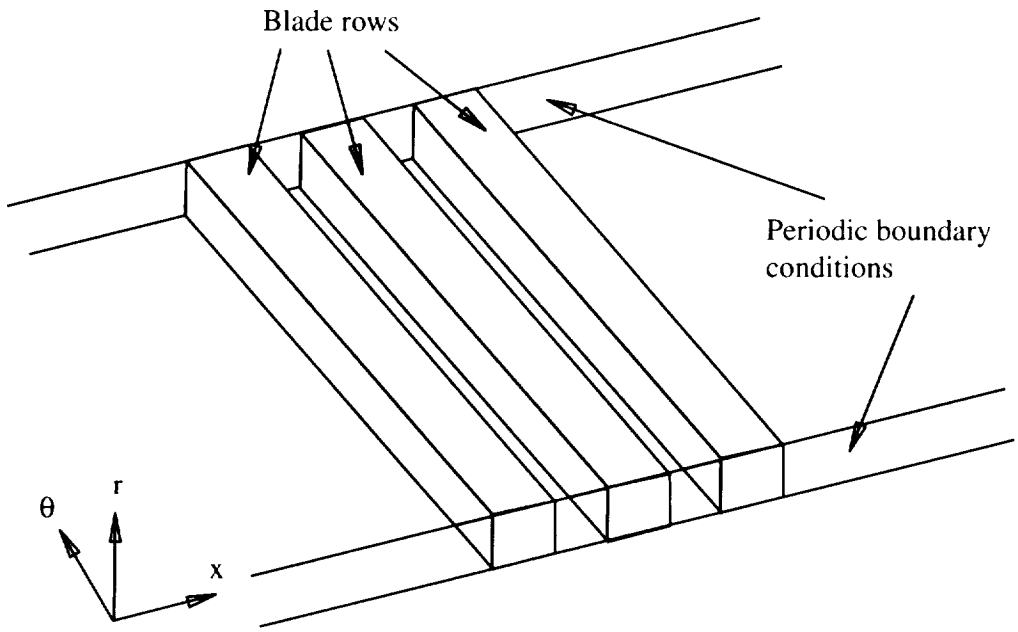

Figure 5.4: An illustration of the multi-rectilinear-cascade representation of a multistage compressor.

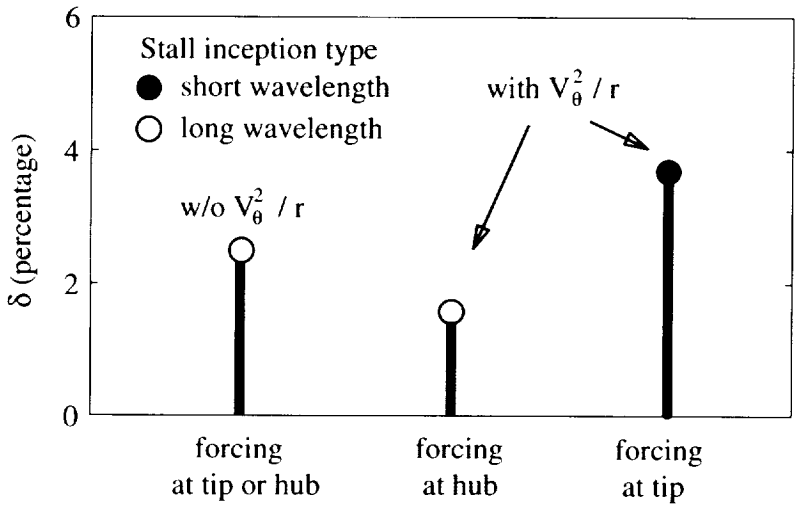

Figure 5.5: The stall point and its inception type of the multi-cascade compressor along with the stall points and their types with hub-forcing and tip-forcing in the GE compressor.

5.3.2 Rotating stall inception in a compressor represented by multiple two-dimensional cascades

The compressor representation was further reduced to remove the spanwise dimension. With this simplification, the GE compressor constitutes nine individual two-dimensional blade rows (or cascades). The spike-shaped forcing has the same shape and amplitude as the forcing in the tip region in the three-dimensional simulations. In the three-dimensional simulation, the forcing is localized in the tip region. The overall effects (on total pressure rise and mass flow of the compressor) of the forcing used in the two-dimensional calculation is more than three times larger than in the three-dimensional calculation.

The computed stall point is indicated in Fig. 5.6, and the stall inception type is modal. Also plotted in the same figure are the stall points initiated by small amplitude disturbances and spike-shaped forcing using the three-dimensional model. The results show that a two-dimensional representation of a compressor stalls through modal waves near the peak of the pressure rise characteristic. Thus short wavelength disturbances cannot be sustained in a two-dimensional system. This again shows the necessity of a three-dimensional model for describing short wavelength stall inception.

It is deduced from the results of the above two cases that: (1) the compressor could stall at the negatively sloped region mostly due to the decoupling of the blade rows, so that a short-length-scale finite-amplitude disturbance could stall a blade row earlier (i.e. at a higher flow coefficient) than would the entire compressor; and (2) the centrifugal effect term, V_θ^2/r, biases the short wavelength disturbance to localize in the tip region.

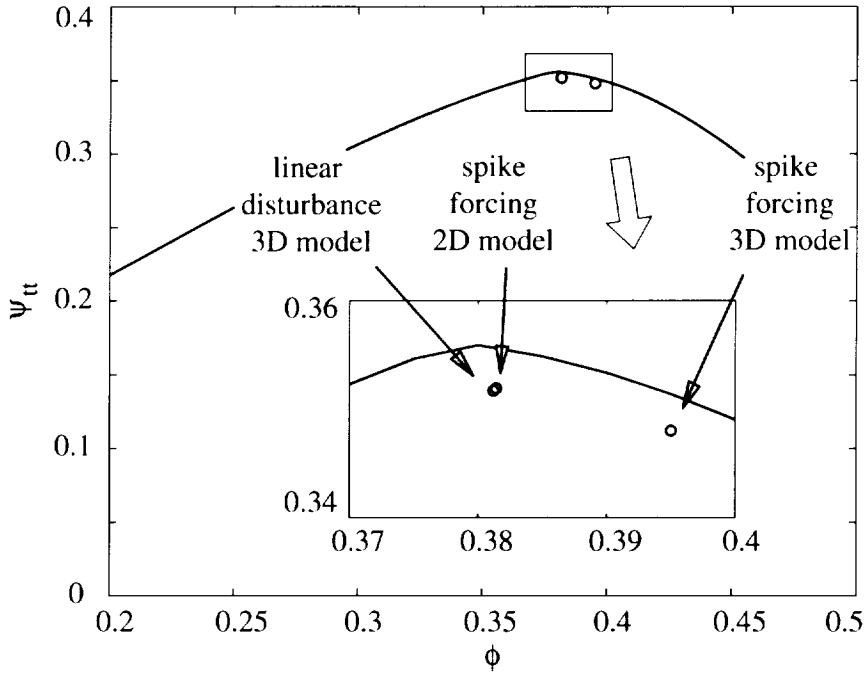

Figure 5.6: Stall point calculated using a two-dimensional row by row representation with finite spike-shaped forcing, and the stall points computed using the three-dimensional model.

5.4 Minimum Requirements in A Compressor Model for Short Wavelength Disturbances

The key ingredients of the model are

1. three-dimensionality, which includes
   (a) blade-row by blade-row representation of compressor
   (b) three-dimensional flow in both blade-free regions and blade rows (composed of infinite number of locally axisymmetric flow fields)
   (c) body force in each blade row region which responds to local simultaneous flow conditions
2. non-linearity of the model, which includes non-linear flow and blade-row non-linear response to the flow
3. spike-shaped forcing impulses as the initiation of short wavelength disturbance.

This type of model constitutes the simplest form that can yield a proper description of short wavelength disturbance in a compressor. This statement is deduced from the following.

1. Experimental observations which have been reviewed in Section 1.3 indicate that short wavelength stall inception is initiated by blade passage events, local to the tip region of a specific blade row.
2. The non-linearity and three-dimensionality of short wavelength stall inception are shown through the following results:
   - the existence of a threshold value of transient forcing below which a compressor does not show short wavelength stall inception (see Section 4.2)
   - the effects of the transient forcing location (see Section 4.1, 4.3)
   - the inability to reproduce short wavelength stall inception using a two-dimensional model (see Section 5.3)

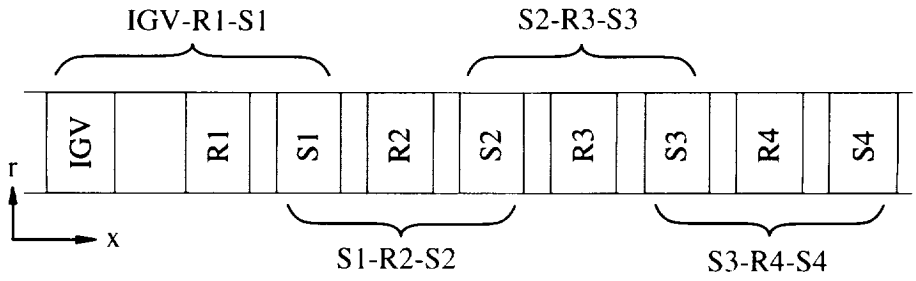

Figure 5.7: There are four component groups in the GE four-stage compressor.

3. Short wavelength stall inception could not be modeled if any of these ingredients were absent.

5.5 Component Group and Its Implications

The concept of "component group" was introduced while assessing the effect of the gap on instability of short length scale disturbances. A component group consists of a rotor and its adjacent stators. It is found that the growth of short wavelength disturbances is determined by the component group where these disturbances appeared. The criterion of instability of a component group is (1) the existence of short length scale disturbances, and (2) the sustenance of the disturbances by the component group. There are multiple component groups in a multi-stage compressor (like the GE compressor shown in Fig. 5.7). The stall point of the entire compressor due to short wavelength disturbances is set by a component group which has the highest stall flow coefficient.

In the GE compressor, the simulations show that the rotor is the most unstable component in a component group, while its neighboring stators have stabilizing effects on the short wavelength disturbances. The growth rate of a disturbance is determined by all these blade rows, and the gaps set the degree of coupling among them.

The most significant effect is that increasing the gap destabilizes the system, a phenomenon which is consistent with observations by Day [12]. This observation can be used to explain why spikes usually emerge in the first stage. For most multi-stage

compressors, the front component group is usually different from other component groups due to (1) the absence of an IGV before the rotor, or (2) the relatively large gap between IGV and first rotor (like the GE compressor), and (3) the fact that the IGV is always lightly loaded. Thus the stabilizing influence from the upstream of the first rotor is relatively weak or absent.

Some deductions from the component group argument on the design are (1) the front stage should have a more stable design (has a relatively low peak flow coefficient); (2) since rotors are usually more unstable than stators, when the operating range of a compressor is limited by the stall point due to short wavelength disturbances, the rotor in the component group should be the first target to be redesigned.

The component group concept does not contradict the "unique rotor tip incidence" as a criterion of short wavelength stall. The component group concept implies that the "unique rotor tip incidence" constitutes a short wavelength stall criterion for a component group. Any changes of characteristics (for instance, gaps, blade stagger) of the component group will alter the value of the "unique rotor tip incidence."

As the type and flow coefficient for compressor instability is sensitive to the intra-blade row gaps, it is not appropriate to intentionally increase these gaps for fitting instrumentation [18], especially when the experiment is used to identify the stall inception types.

5.6 Routes to rotating stall

In this section, several routes of stall development subsequent to the initial growth of a short wavelength disturbance are conjectured based on the available observations and numerical simulations. It is argued that there could be more than one possible route for a short wavelength disturbance to evolve, and this could be due to a difference in the flow coefficient between the short wavelength disturbance stall point and the modal wave stall point. Several possible routes are proposed in the following.

1. A short wavelength disturbance could grow and develop into a large stall cell or surge, like a typical spike-type stall inception (Fig. 1.5). The numerical

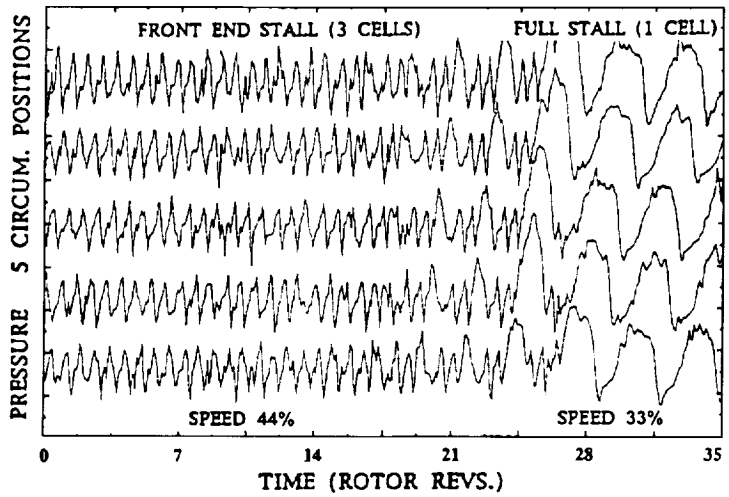

Figure 5.8: Velocity traces show 1.5 times rotor frequency disturbance at the front stage prior to the final stall cell [11].

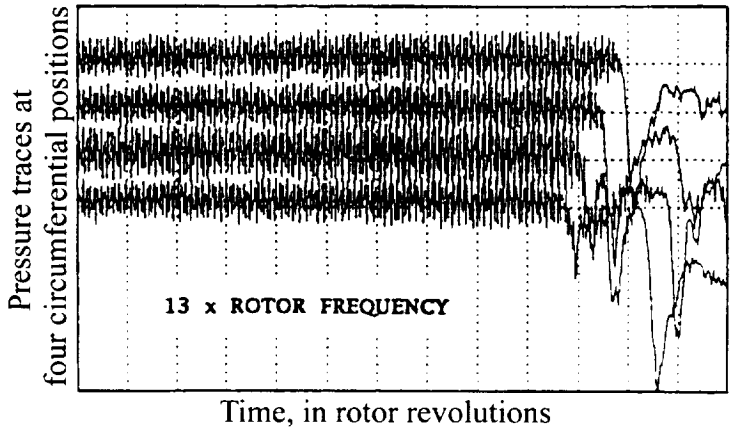

Figure 5.9: Velocity traces show 13 times rotor frequency disturbance at the front stage prior to the final stall cell [11].

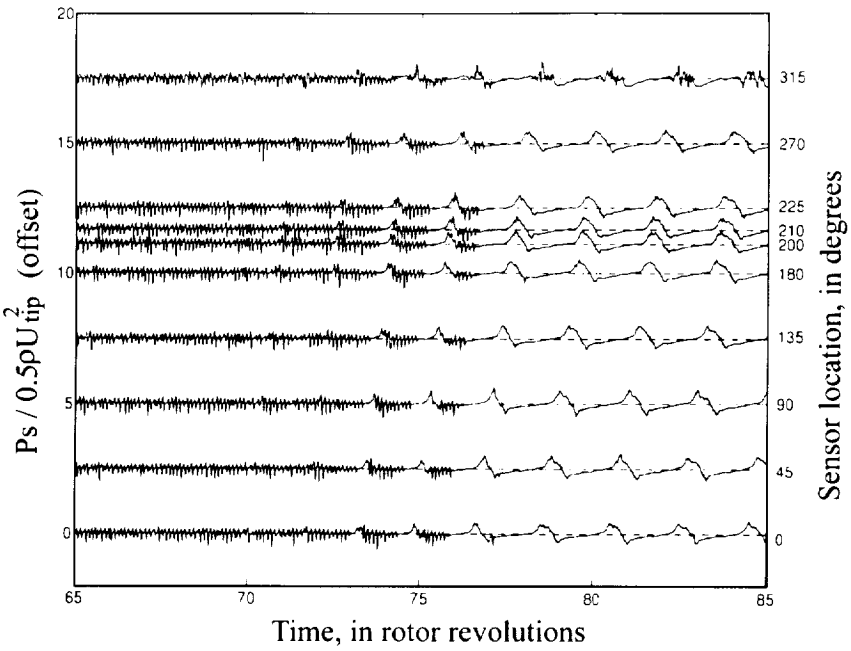

Figure 5.10: Casing static pressure traces at the first stage rotor inlet during the transition from twelve local stall cells to a single stall cell. GE compressor, mismatched build [56].

simulation for the single stage configuration of the GE compressor shows this route to the final single stall cell pattern. This should happen when the stall point for short wavelength disturbances is close to the stall point of the entire compressor, so that the other components in the system do not have much stabilizing effect on the disturbance. Usually, a single stage (except a fan that has a large rotor-stator gap) compressor takes this route to the final rotating stall.

2. A short wavelength disturbance could also cause several or many stall cells to form before a large stall cell is developed. The "Front-end start-up stall" (Fig. 5.8) and "high frequency stall" (Fig. 5.9) [11] might be classified into this type of route. The cause could be the fact that a component group becomes unstable at a flow coefficient where the overall compressor can operate in stable operation, so that each short wavelength disturbance cannot grow into a large

stall cell. However, with the number of small stall cells increasing, the reduction in overall flow coefficient, and a large disturbance, which is superimposed on small stall cells, can cause the formation of a large stall cell. The scenario is due to the mismatch in stalling points between of a local component group and of the entire compressor. The argument is supported by the similar stalling scenario between the "high frequency stall" (Fig. 5.9) [11] and the mismatched build of the GE compressor (Fig. 5.10) [56].

3. The front spike-shaped disturbance could also trigger the long length scale nonlinear three-dimensional disturbance in downstream stages, as is the case in the numerical simulation. In the numerical simulation, the disturbance (mostly its vortical part) in the front stage is transmitted to the downstream stages, and causes the downstream stages to go into rotating stall. There is no measurement to support this route, which is, however, a possible one.

To summarize, the routes of stall cell development could vary in different compressor as well as at different operating points for one compressor. This is because an additional spanwise length scale is introduced into the system, so that the localized disturbances could grow regardless of the operating condition of the overall compressor. The available experimental observations seem to support the above conjectures.

5.7 Effect of design flow coefficient

The hypothesis that a compressor with low stalling flow coefficient tends to stall through short wavelength disturbances is presented in this section based on experimental observations and a simple analysis.

Experimental data presented in [9, 11] appears to indicate that modern compressors tend to show short wavelength stall inception. An overall design feature of a modern compressor is that it tends to have a lower design flow coefficient. Day [8] showed that the stalling characteristic (Fig. 5.11) was related to its design flow coefficient. He found that compressors with high design flow coefficient show typical stall

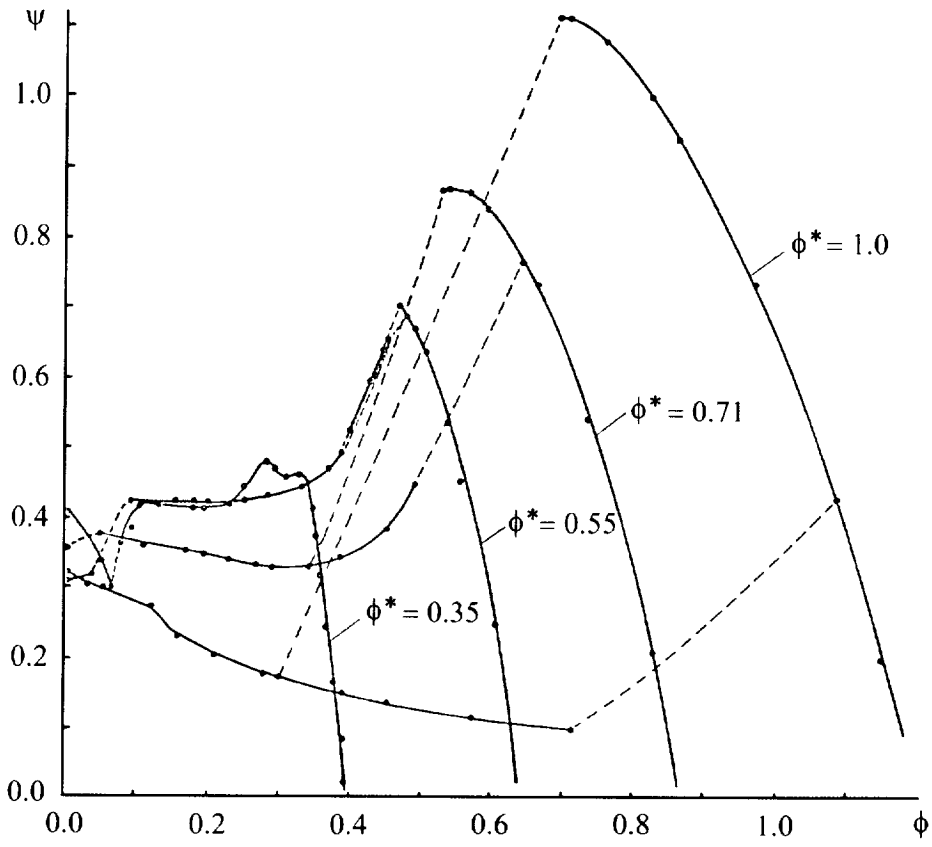

Figure 5.11: Effects of design flow coefficient on the compressor stall characteristic

characteristic with large hysteresis, while compressors with low design flow coefficient show progressive stalling characteristics with little hysteresis but with a multiple stall cell pattern. The phenomena Day described for the compressors with low design flow coefficient are similar to the results of the GE mismatched compressor [60]. One might interpret Day's experimental observation as showing that a compressor with low design flow coefficient tends to be mismatched (even though the geometry of each stage is exactly the same). Here the term "mismatch" is measured by the difference in stalling point among component groups and the entire compressor. When a local component group stalls at a higher flow coefficient than the overall compressor does, the stall inception type is expected to be of short wavelength.

In the following, arguments are put forth to show that for a compressor with low design flow coefficient, a rotor would reach the positively sloped region at a higher flow coefficient than a stage does, thus the rotor is more unstable than the stage (and the compressor); therefore the component group could stall earlier than the entire compressor. The stall inception initiated in a local component group is of the short wavelength type. Although the argument is based on the slope of pressure rise characteristics and the stalling point of a component group cannot be solely determined by the slope, the trend of variation of the slope should reflect the change of instability point.

The argument can be formulated by examining $d\Psi_{ts,\ rotor}/d\phi$ of the rotor at the peak of the stage characteristic (i.e. $d\Psi_{ts,\ stage}/d\psi = 0$). To evaluate the slope of the rotor characteristic, some design parameters have to be assumed. The sole purpose of these curves is to illustrate the trend however, and the exact values of these parameters are not critical to the argument.

The notation of velocity triangles of a stage is illustrated in Fig.5.12. I assume that the stage characteristic reaches the peak at a critical diffusion factor ($D_s = 0.65$ will be used to give numerical results) for both rotor and stator, then the exit flow angle can be calculated from the definition of diffusion factor. The stage pressure rise

can be written as

$$\psi_{ts} = \frac{P_{s\,3} - P_{t\,1}}{\rho U^2} = 1 - \phi \tan \beta_2' - \phi \tan \beta_1 - L_r - L_s - \frac{1}{2}\frac{\phi^2}{\cos \beta_3} \tag{5.1}$$

and the rotor pressure rise as

$$\Psi_{ts,\,rotor} = \Psi_{ts} + L_s + \frac{1}{2}(\phi^2(\frac{1}{\cos^2 \beta_3} - 1 + \tan^2 \beta_2') + 2 \tan \beta_2' - 1) \tag{5.2}$$

where L_r and L_s are the respective loss in the rotor and stator. At the peak of the stage characteristic where $d\Psi_{ts}/d\phi = 0$, the slope of the rotor characteristic is

$$\frac{d\Psi_{ts,\,rotor}}{d\phi} = \frac{dL_s}{d\phi} + \phi(\frac{1}{cos^2 \beta_3} - 1 + \tan^2 \beta_2') + (\phi \tan \beta_2' + 1)\phi \frac{d \tan \beta_2'}{d\phi} + \tan \beta_2' \tag{5.3}$$

The stage characteristic, Eq. 5.1, at the peak (where $d\Psi_{ts}/d\phi = 0$) gives

$$\frac{d(\phi \tan \beta_2')}{d\phi} + \frac{dL_r}{d\phi} + \frac{dL_s}{d\phi} = -\tan \beta_2' - \tan \beta_1 - \frac{\phi}{\cos^2 \beta_3} \tag{5.4}$$

I can express the three terms in the left-hand side as

$$\begin{aligned} \frac{d(\phi \tan \beta_2')}{d\phi} &= n_1 J \\ \frac{dL_r}{d\phi} &= n_2 J \\ \frac{dL_s}{d\phi} &= n_3 J \end{aligned} \tag{5.5}$$

n_1, n_2, and n_3 must satisfy the following relation.

$$n_1 + n_2 + n_3 = 1$$

and

$$J = -\tan \beta_2' - \tan \beta_1 - \frac{\phi}{\cos^2 \beta_3}$$

$n_1 J$, $n_2 J$, and $n_3 J$ represent the fraction of the loss in stage pressure rise due to the rotor deviation, the losses in rotor and stator respectively. The $d\Psi_{ts,\,rotor}/d\phi$ at the

Table 5.1: A list of compressors, their stall flow coefficients, and stall inception types.

No.	Description	Stall flow coefficient	Stall inception type
1	GE four-stage compressor [60]	0.39	spike
2	Deverson 1.2% tip clearance [49]	0.39	spike
3	Deverson 3.0% tip clearance [49]	0.42	modal
4	C106 1.2% tip clearance [9]	0.4	spike
5	Longley [42]	0.49	modal
6	MIT three-stage [30]	0.47	modal
7	MIT one-stage [54]	0.45	modal
8	GE compressor A [44]	0.46	modal
9	GE compressor B [44]	0.56	modal
10	GE compressor D [44]	0.44	spike

peak versus peak flow coefficient can be plotted in Fig. 5.13 including only one of the three factors, and a combination of all three effects. Figure 5.13 shows that the slope of rotor characteristic increases with decreasing peak flow coefficient (so is the design flow coefficient if the stall margin is kept the same). The trend can be stated as follows: the rotor tends to reach the peak of its characteristic prior to that of the stage for a low flow coefficient design. This might explain the relationship between design flow coefficient and stall inception type.

The argument is also supported by the observation that all spike compressors (in the public domain) have their stalling flow coefficients below 0.45 (mostly around 0.4) as shown in Fig. 5.14 and listed in Table 5.1. The number two and three compressors are the same compressor (Deverson) with different tip clearances. The one with tight tip clearance stalls at a lower flow coefficient through spike type, the one with loose tip clearance stalls through long wavelength disturbances at a higher flow coefficient.

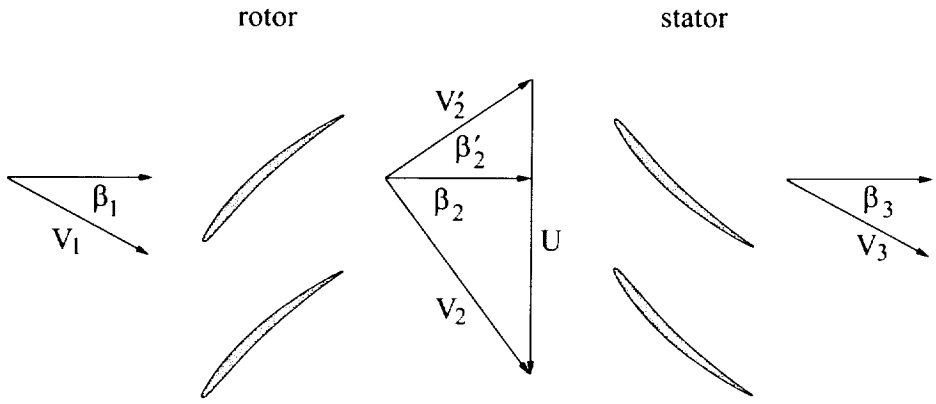

Figure 5.12: Velocity trangle and notation for a compressor stage.

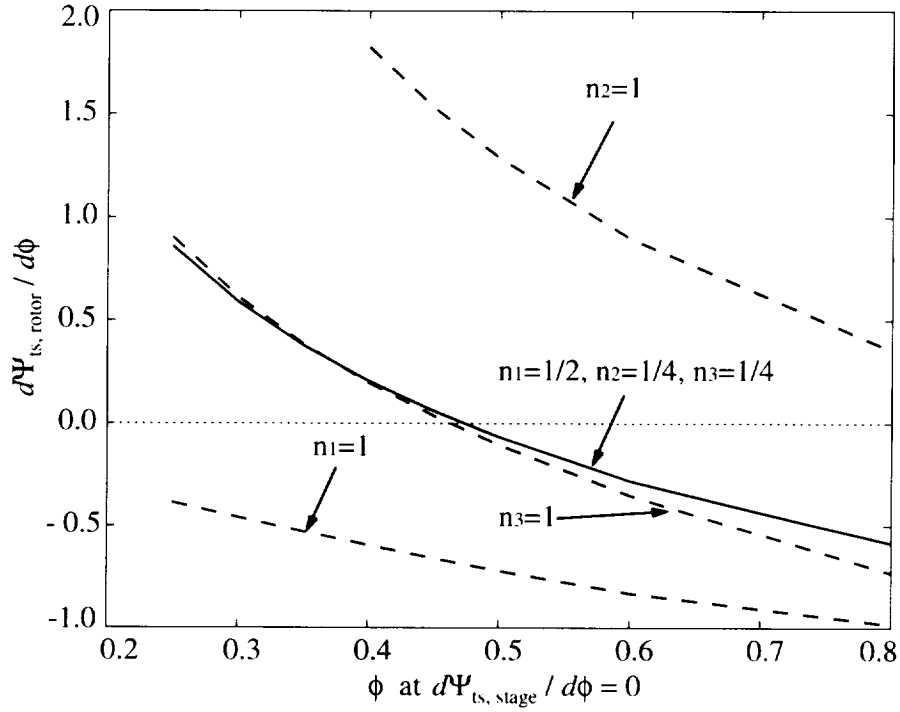

Figure 5.13: Slope of rotor characteristic at the peak of the stage characteristic for different stage peak flow coefficients.

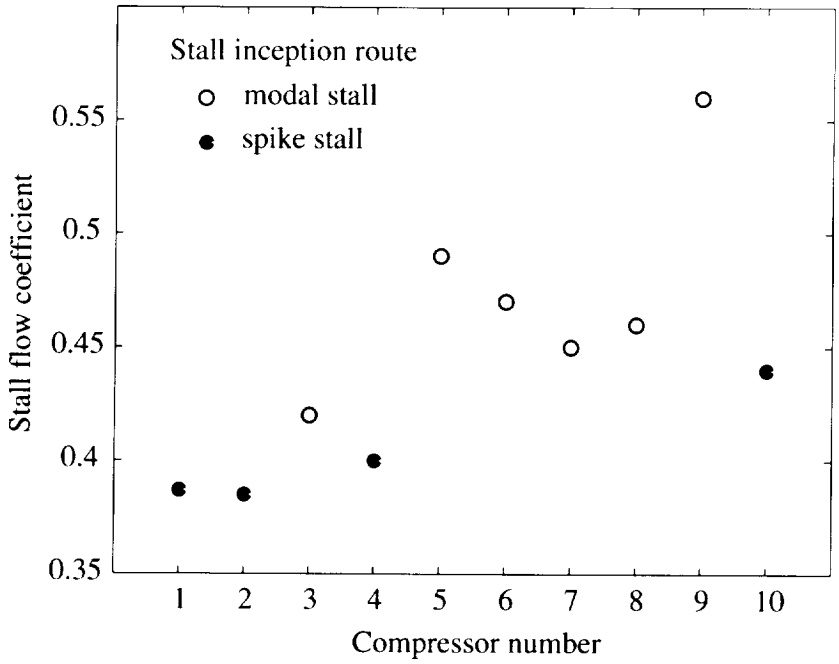

Figure 5.14: The stalling flow coefficient and stall inception type of ten compressors. The compressor and flow coefficient are listed in Table 5.1. The data show that compressors with low stall flow coefficient stall through short wavelength type.

5.8 Summary

Some additional physical aspects of the model are discussed in this chapter. First of all, the swirl sensitivity, which was ignored in the simulations, is shown to have relatively small effects on short wavelength stall inception in the GE compressor. The physical origin of the transient forcing is then discussed and related to the tip vortex behavior observed from a Navier-Stokes simulation for a multi-blade passage situation.

The three-dimensional aspects of the model are further explored in Section 5.3. It is argued that the additional length scale in the spanwise direction de-couples blade rows so that one blade row (usually a rotor) could stall earlier than the entire compressor. The centrifugal effect term, V_θ^2/r, appears to make the short wavelength stall inception more sustainable in the tip region than in the hub region, and this can explain why spikes tend to be localized in the tip region. Based on the observations in experiments and numerical simulations, a model with the elements employed by

the current treatment is the simplest one which can be used to calculate the short wavelength stalling process.

The component group, which is deduced in Chapter 4, is further discussed and its implications are deduced.

Finally, two hypotheses are put forth: (1) the development of short wavelength disturbances could proceed through several different routes, depending upon the degree of mismatch between component groups and an entire compressor; and (2) a compressor with low flow coefficient design (which most modern compressors are) tends to stall through the short wavelength type.

Chapter 6

Computational Flow Model for High-Speed Compressors

A computational model for high-speed compressors will be described in the present chapter. It is a direct extension of the computational model for low speed compressors described in Chapter 2.

The model will be aimed at computing the response of compressor to flow distortion and its instability phenomena under general distorted flow conditions as well as uniform flow condition. As in the low speed compressor model, the high-speed model is developed to describe the non-linear three-dimensional unsteady disturbances in multi-stage compressors. The methodology used to construct the model for high-speed compressors is the same as that described in Chapter 2, which emphasizes the response of a blade row to unsteady three-dimensional non-uniform flow but ignores the detailed flow structure in each individual blade passage.

Compressibility of flow introduces the following additional effects:

1. the loading distribution on each stage in the compressor depends on the rotor speed;

2. phenomena unique to high-speed compressors (e.g. choking, and shock wave) can change the behavior of the system;

3. behavior of acoustic waves need to be considered in the prediction of compressor

instability;

4. blade rows and ducts also act to increase the effective flow capacity of the plenum of a compression system.

In summary, introduction of the flow compressibility increases the complexity of the system.

The objective of this chapter is to demonstrate the methodology rather than to examine specific stability issues in compressors. Thus compressor response to inlet distortions will be presented as numerical examples to illustrate the capability of the model to describe three-dimensional disturbances and blade-row response.

The development of the model, the basic flow equations, and the formulation of body force are first described. Selected numerical examples on compressor response to inlet distortions are then presented as a demonstration of the capability of the model. The chapter is arranged as follows. Section 1 describes the governing equations in blade row regions and blade-free regions; Section 2 discusses the formulation of body force in blade regions; Section 3 shows computational results for a single stage transonic compressor with inlet total pressure and total temperature distortions; Section 4 gives a summary of the results.

6.1 Governing Equations

The flow in ducts and intra-blade-row gaps is described by the three-dimensional unsteady Euler equations for mass, momentum, and energy conservation:

$$\frac{\partial}{\partial t}\begin{bmatrix} r\rho \\ r\rho V_x \\ r\rho V_\theta \\ r\rho V_r \\ r\rho e_t \end{bmatrix} + \frac{\partial}{\partial x}\begin{bmatrix} r\rho V_x \\ r\rho V_x^2 + rp \\ r\rho V_x V_\theta \\ r\rho V_x V_r \\ rV_x(\rho e_t + p) \end{bmatrix} + \frac{\partial}{\partial \theta}\begin{bmatrix} \rho V_\theta \\ \rho V_x V_\theta \\ \rho V_\theta^2 + p \\ \rho V_\theta V_r \\ V_\theta(\rho e_t + p) \end{bmatrix}$$

$$+\frac{\partial}{\partial r}\begin{bmatrix} r\rho V_r \\ r\rho V_x V_r \\ r\rho V_\theta V_r \\ r\rho V_r^2 + rp \\ rV_r(\rho e_t + p) \end{bmatrix} = \begin{bmatrix} 0 \\ 0 \\ -\rho V_\theta V_r \\ \rho V_\theta^2 + p \\ 0 \end{bmatrix} \tag{6.1}$$

In the blade row region, the assumption of infinite number of blades implies that the flow is locally axisymmetric in the blade row reference frame. The equations for blade rows can be derived in exactly the same way as that for the low speed model as presented in Section2.2. The final form of the equations are

$$(\frac{\partial}{\partial t} + \Omega\frac{\partial}{\partial \theta})\begin{bmatrix} r\rho \\ r\rho V_x \\ r\rho V_\theta \\ r\rho V_r \\ r\rho e_t \end{bmatrix} + \frac{\partial}{\partial x}\begin{bmatrix} r\rho V_x \\ r\rho V_x^2 + rp \\ r\rho V_x V_\theta \\ r\rho V_x V_r \\ rV_x(\rho e_t + p) \end{bmatrix} + \frac{\partial}{\partial r}\begin{bmatrix} r\rho V_r \\ r\rho V_x V_r \\ r\rho V_\theta V_r \\ r\rho V_r^2 + rp \\ rV_r(\rho e_t + p) \end{bmatrix}$$

$$= \begin{bmatrix} 0 \\ r\rho F_x \\ -\rho V_\theta V_r + r\rho F_\theta \\ \rho V_\theta^2 + p + r\rho F_r \\ r\rho(\mathbf{F}\cdot\mathbf{V} + \dot{q}) \end{bmatrix} \tag{6.2}$$

where $F_x, F_\theta, F_r, \dot{q}$ are the body force and heat source terms. The units of these terms are force or heat release per unit volume.

If there is no additional heat source in the fluid, the energy transfer between fluid and outside is through the blade force; therefore the source term in the energy equation is the work done by the rotor blade row. The above statement can be expressed as

$$\mathbf{F} \cdot \mathbf{V} + \dot{q} = F_\theta \Omega r$$

where Ω is the rotating speed of the blade row, and F_θ the net tangential body force.

The formulation of body force terms will be discussed in the next section.

6.2 Formulation of Body Force

The general exposition on the concept of body force representation of blade row can be found in the reference by Marble [46]. The current formulation focuses on those aspects that represent the response to unsteady three-dimensional flow, the key feature in the flow situations of interest here. The key idea here is to let body force field respond to local flow properties instantaneously. The body force formulation (i.e. the way body force responds to local flow properties) is determined based on steady flow field. This type of body force formulation has been shown to be adequate for simulation of stall inception through short wavelength disturbances (see Chapter 3 and 4).

6.2.1 A Form of Body Force for Representing a Blade Passage

The force normal to the blade surface is associated with the blade pressure difference between pressure side and suction side; while the force parallel to the blade surface is associated with the viscous shear.

A key aspect of the formulation is to express the body force as a function of local flow properties. This assumed functional dependence on local flow properties has

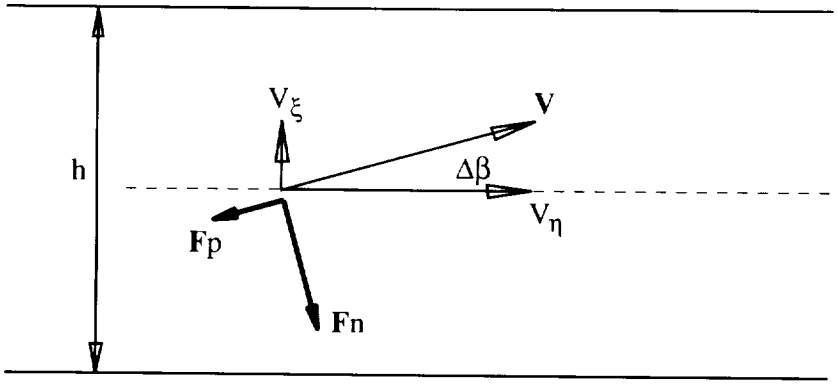

Figure 6.1: The flow in a blade passage is modeled locally as a flow in a straight channel.

been shown to be adequate for simulating flow instability in low speed compressors.

To elucidate the functional dependency of body force on local flow properties, it is useful to examine flow in a straight channel which is, in a first order approximation, similar to flow in a blade passage. A sector of a blade passage is considered as a straight channel, and the flow properties at a particular location are indicated in Fig. 6.1. The force can generally be expressed as

$$\frac{h\mathbf{F}}{\rho V^2} = \mathbf{f}(M, \Delta\beta, Re)$$

where V, M, $\Delta\beta$, and Re are local values, and h is the local spacing of the blade passage (Fig. 6.1). Since the Re effects are relatively small if Re is sufficiently high, therefore an adequate form of the body force is

$$\frac{h\mathbf{F}}{\rho V^2} = \mathbf{f}(M, \Delta\beta) \tag{6.3}$$

Following the analysis of Marble [46], it is useful to split the body force into two parts: one normal to the relative flow direction annotated as $\mathbf{F}_n$, the other, annotated as $\mathbf{F}_p$, parallel to the flow direction in the relative frame. An advantage of splitting the body force representation into these two parts is that each part can be formulated on its own physical basis. Thus $\mathbf{F}_n$ would represent the effects of pressure difference between the pressure surface and suction surface, enabling work exchange between

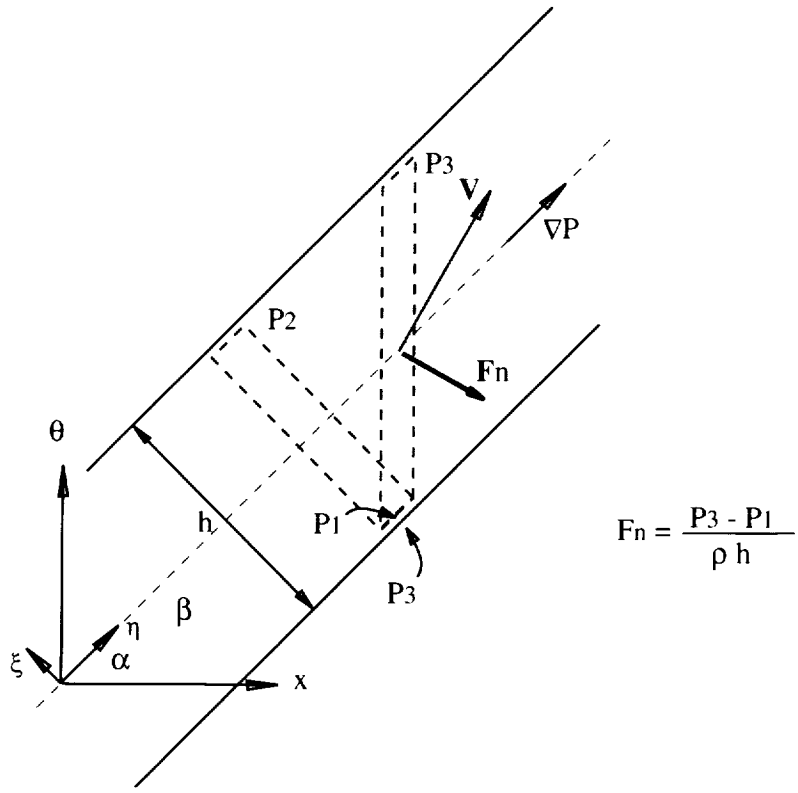

Figure 6.2: The body force due to pressure gradient in a staggered channel. The velocity is along the blade passage; and the pressure gradient is also in the blade passage direction. The pressure gradient has a component in the circumferential direction, so it creates the pressure difference (P3-P1) across the blade.

blade row and fluid. The body force parallel to the flow, $\mathbf{F}_p$, is due to the viscous shear stress. This part of the body force produces losses as well as adds work into the fluid. The functional dependence of the body force can now be written as

$$\frac{h\mathbf{F}_n}{\rho V^2} = f_n(M, \Delta\beta)$$
$$\frac{h\mathbf{F}_p}{\rho V^2} = f_p(M, \Delta\beta) \tag{6.4}$$

The body force formulation thus is reduced to the task of determining f_n, and f_p at every spatial point in each blade row.

It is realized that the pressure gradient in a staggered channel could also produce pressure difference across the blade, as shown in Fig. 6.2. The cause is that the pressure gradient in a blade passage is, to a first order of approximation, in the direction of blade passage. The pressure gradient in a staggered blade passage is different from the axisymmetric assumption which assumes that the pressure (and other flow properties) gradient is in the direction of the meridional plane. The force term which corresponds to the local pressure gradient is

$$F_n = \frac{1}{\rho}\frac{\partial P}{\partial x}\sin\alpha \tag{6.5}$$

6.2.2 A Proposed Body Force Formulation

The purpose of developing this formulation is to enable the model to be applied to situations where detailed measurements are not available.

Body force responding to local deviation

The part of the body force which represents the blade response to the discrepancy between blade metal angle and flow direction, is formulated here. The flow in a blade passage is locally modeled as flow in a straight channel, as shown in Fig. 6.1. η and ξ are the axes in the local blade channel direction and the direction normal to the local blade channel respectively. The body force normal to the flow direction, ξ, is

formulated as follows.

The ξ-momentum equation can be written as

$$V_\eta \frac{\partial V_\xi}{\partial \eta} = F_{n,\xi}$$

Therefore, the normal to blade passage component of the normal body force has the following form

$$F_{n,\xi} \sim \frac{V_\eta V_\xi}{h}$$

In the above expression, h is preferred to the blade chord since h can be defined locally. Using the functional form of Eq. 6.4, the $F_{n,\xi}$ can be expressed as

$$F_{n,\xi} = K_{n,\eta}(\Delta\beta, M)\frac{V_\eta V_\xi}{h} \tag{6.6}$$

An undesirable difficulty associated with above formulation is when $\Delta\beta$ reaches 90°

$$F_{n,\eta} = F_{n,\xi}\tan(\Delta\beta) = K_{n,\xi}(\Delta\beta, M)\frac{V_\xi^2}{h}$$

which has a finite value. This cannot be right since $F_{n,\eta}$ must be zero in this situation. To overcome this, the formulation is modified to:

$$F_n = K_n(\Delta\beta, M)\frac{V_\eta V_\xi}{h} \tag{6.7}$$

The above form is nearly equivalent to the original form when $\Delta\beta$ is small since

$$F_{n,\xi} = \cos\Delta\beta F_n$$

and it will be zero if V_η becomes zero.

Upon applying the above formulation in a blade passage where the local blade passage (a straight channel) is along the local blade metal angle,α (see Fig. 6.3), we

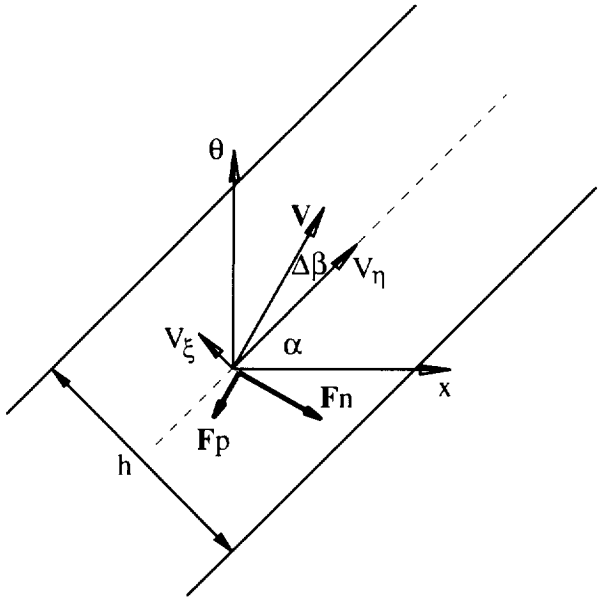

Figure 6.3: The flow in a blade passage in (x, θ) plane.

have

$$\begin{aligned} F_{n,x} &= F_n \sin(\alpha + \Delta\beta) \\ F_{n,\theta} &= -F_n \cos(\alpha + \Delta\beta) \end{aligned} \tag{6.8}$$

These can further be rewritten as

$$\begin{aligned} F_{n,x} &= \frac{K_n(\Delta\beta, M)}{h} \frac{V_\theta}{V} (V_x \cos\alpha + V_\theta \sin\alpha)(V_\theta \cos\alpha - V_x \sin\alpha) \\ F_{n,\theta} &= -\frac{K_n(\Delta\beta, M)}{h} \frac{V_x}{V} (V_x \cos\alpha + V_\theta \sin\alpha)(V_\theta \cos\alpha - V_x \sin\alpha) \end{aligned} \tag{6.9}$$

Body force: viscous effect

The body force associated with viscous shear is against the flow direction, and can thus be written as

$$\begin{aligned} F_{p,x} &= -\frac{K_p(\Delta\beta, M)}{h} V V_x \\ F_{p,\theta} &= -\frac{K_p(\Delta\beta, M)}{h} V V_\theta \\ F_{p,r} &= -\frac{K_p(\Delta\beta, M)}{h} V V_r \end{aligned} \tag{6.10}$$

The resultant force is the vector sum of all these terms in Eq. 6.10, Eq. 6.11, and Eq. 6.5.

The functionality of the above formulation is essentially the same as that described in Section 6.2.1, and provides a convenient way to correlate coefficients against measurements or CFD computations. To demonstrate the methodology, the coefficients have been correlated based on Rotor 35 geometry at the mid-span and tip location, using loss and deviation data from a standard reference [41]. The resultant K_n and K_p are

$$K_n = 4.2 - 3.3 * \alpha$$

$$K_p = 0.04$$

6.3 Numerical Examples: Compressor Response to Inlet Distortions

Numerical simulations were performed based on Stage 35 [58]. Stage 35 is a single stage transonic compressor designed by NASA Lewis Research Center in the late 70's [58]. The compressor features low aspect ratio rotor and stator blades, a high design pressure ratio of 1.82. The design parameters are listed in Table 6.1.

The first example is the compressor response to a square-wave total pressure distortion far upstream. Some of the computed results will be compared against measurements. In the second case, a total temperature non-uniformity is imposed at the location far upstream of Stage 35. The results of the two examples are to show that the model yields an adequate description of a compressor response with finite amplitude distortions. The third case is an abrupt square-wave total pressure distortion far upstream of Stage 35. This case will demonstrate the capability of the model for simulating finite amplitude unsteady disturbances in a compression system.

The computational domain is shown in Fig. 6.4. Near the exit, the flow path is modified to relieve the numerical difficulty associated with the reverse flow at the hub-wall due to the curvature effects. The locations where the results are plotted and

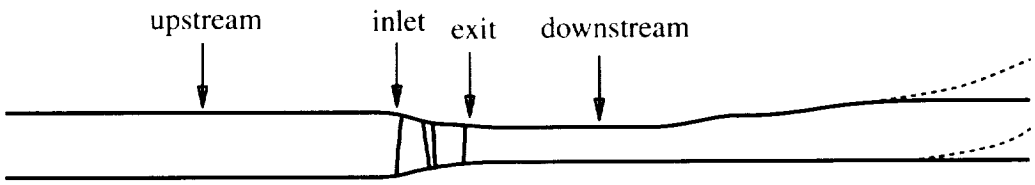

Figure 6.4: The computational domain (solid line) is based on the real geometry except for the exit region denoted by dash line. Flow variables taken at the four indicated locations are used for comparison between measurements and computed results.

Table 6.1: Some design parameters of Stage 35.

Number of rotor blades	36
Rotor rotating speed	1800 rad/sec
Rotor aspect ratio	1.19
Hub-to-tip ratio at rotor inlet	0.7
Solidity of rotor	1.29 at tip 1.77 at hub
Number of stator blades	46
Stator aspect ratio	1.26
Solidity of stator	1.3 at the tip 1.5 at the hub

measured are indicated in the same figure. The computational mesh size is 142(axial) by 200(circumferential) by 10(radial) cells, shown in Fig. 6.5.

The performance map, shown in Fig. 6.6, is computed using the body force formulation developed in the previous section with coefficients K_n and K_p in Eq. 6.10 and Eq. 6.11. On an overall basis, the computed results (Fig. 6.6) agree with the measured performance map (Fig. 6.7) in the region away from the surge line. Along each speedline, the highest mass flow point corresponds to the choking point, which is in agreement with the measured value. The pressure rise is slightly higher than the measured value near the design flow coefficient. This is expected, as the endwall flow effects are not accounted for in the model. The computed performance at the low flow region deviates from the measurements since the body force has not been calibrated in that region. For the same reason, the present work will only confine to demonstrating the utility of the model for assessing compressor response to distortions.

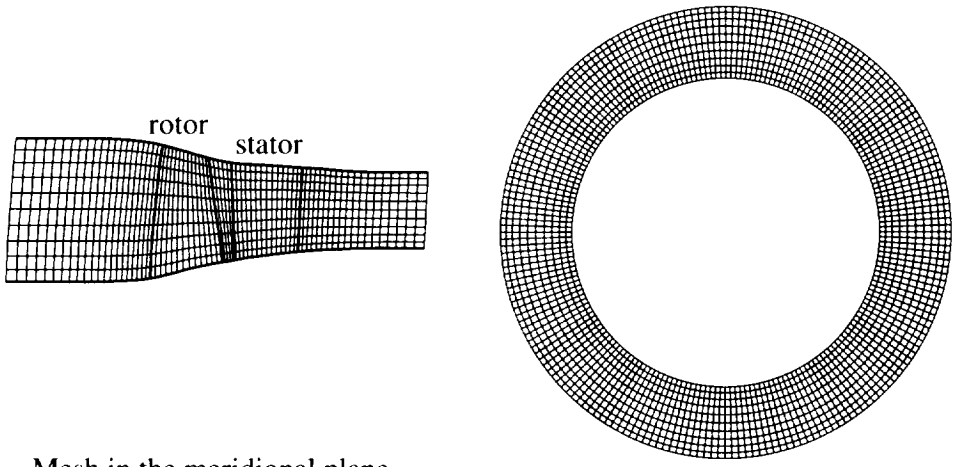

Figure 6.5: The computational mesh around the rotor and stator. The leading edges and trailing edges are indicated by thick lines.

The relative Mach number distribution in the rotor at 100% speed is shown in Fig. 6.8. The Mach number around the leading edge exhibits shock-like distribution. Since there are only 13 cells along the axial direction in the rotor, it is difficult to tell whether there is a shock at the leading edge from Mach number contours. The existence of a shock becomes evident when the relative flow angle distribution and static pressure distribution at the tip are plotted. As shown in Fig. 6.9, the static pressure and entropy go up sharply (within first three points), while the relative flow angle remains relatively unchanged in that region. The importance of capturing shock is that shock is the main mechanism of producing pressure rise and loss in a transonic blade row. The static distribution at the rotor tip shows that the entire pressure rise and half of the entropy rise in the blade passage occurs around the leading edge. The computed loss coefficient of the rotor is shown in Fig. 6.10, and is in agreement with the experimental data. The computed deviation also matches the measurement (Fig. 6.11).

In summary, the methodology with the proposed body force representation of blade row appears to give a fairly good description of the compressor map and the associated flow field.

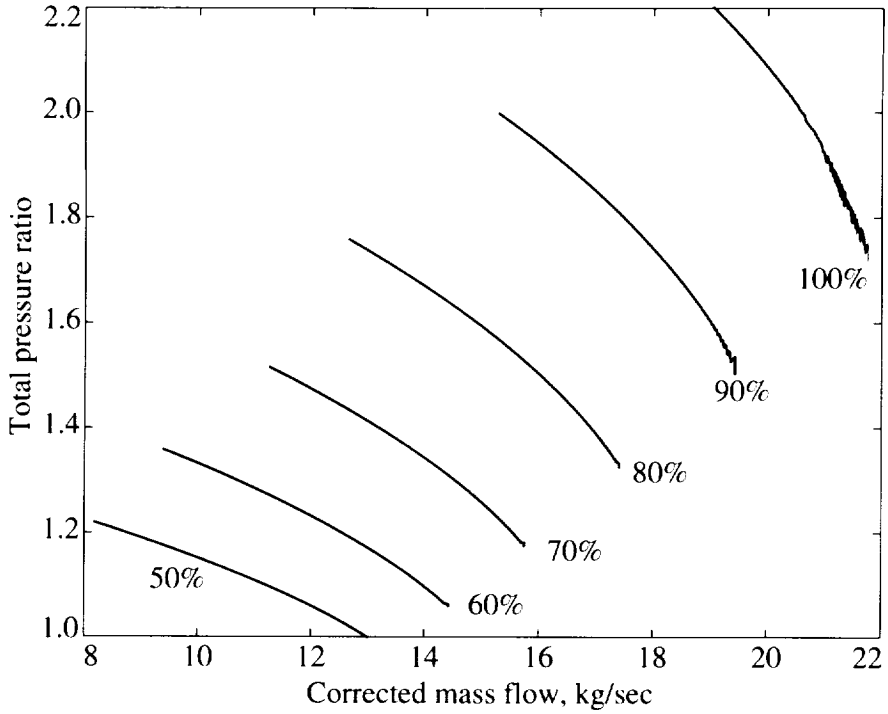

Figure 6.6: The computed compressor performance map of Stage 35.

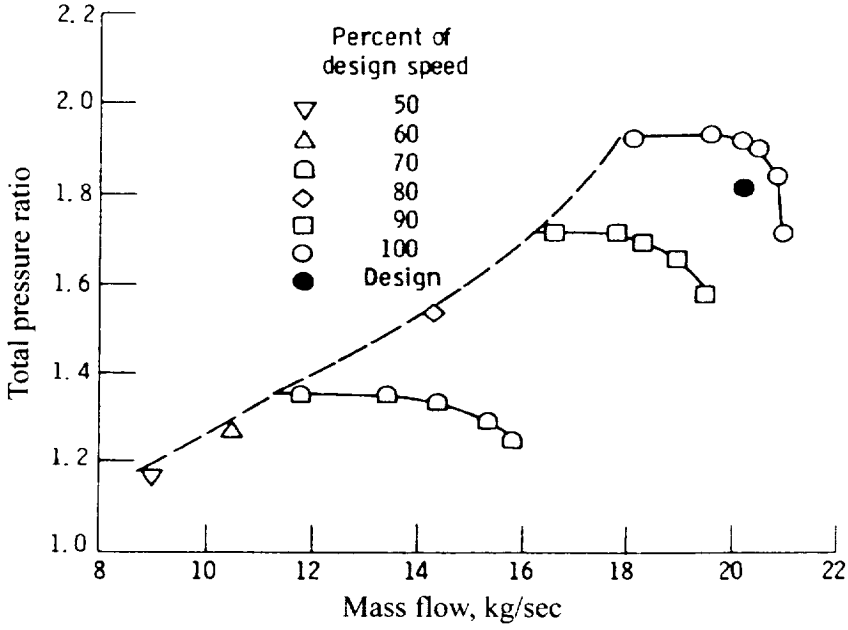

Figure 6.7: The measured compressor performance map of Stage 35 [58]; the filled circle donates the design point.

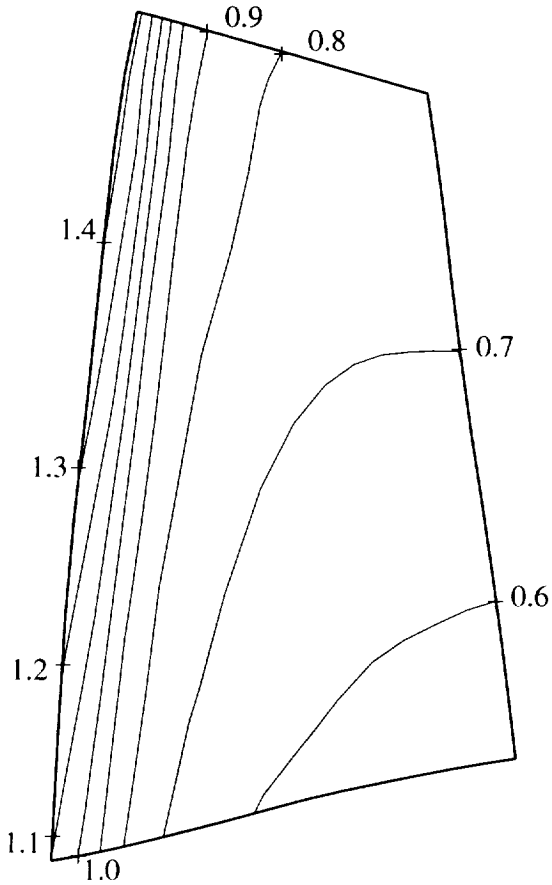

Figure 6.8: Computed Mach number distribution in the rotor. The compressor is operated at 100% design rotational speed and mass flow rate of 20.2 kg/sec. The model captures a shock at the leading edge.

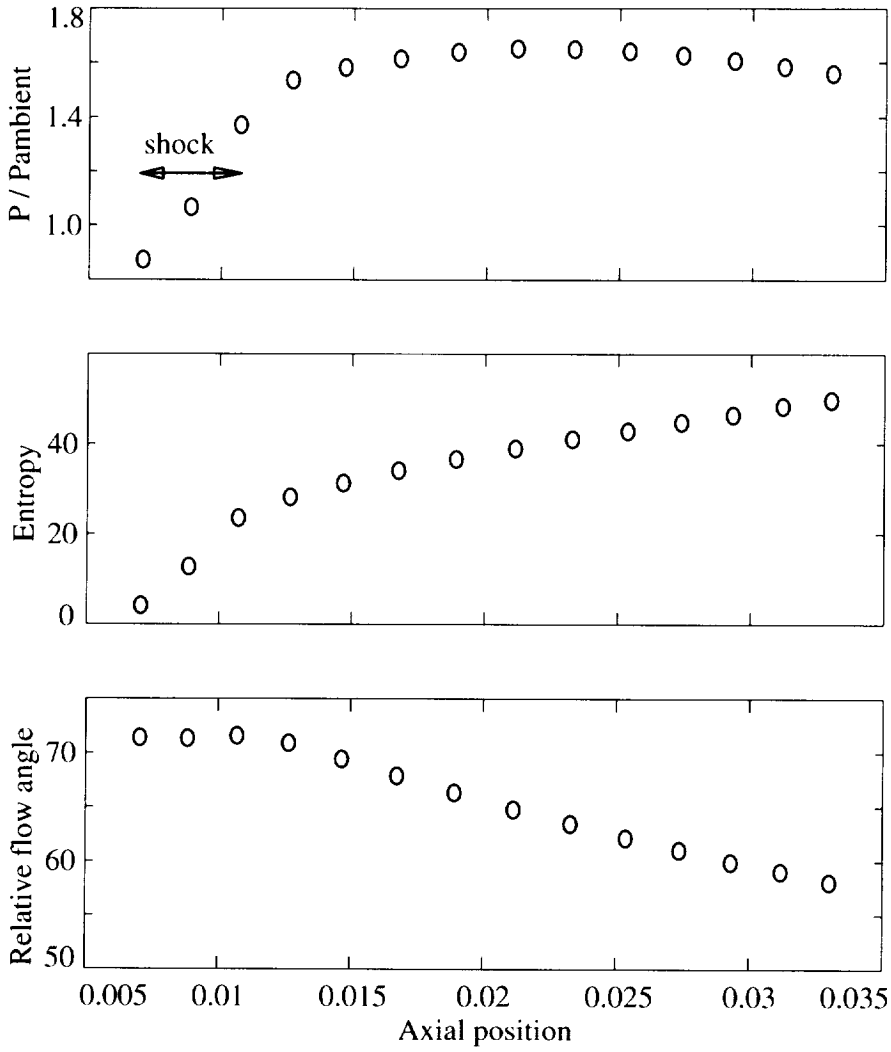

Figure 6.9: The computed static pressure, entropy, and relative flow angle distribution from the leading edge to the trailing edge at the tip region of Rotor 35. The leading edge position is at the first circle symbol, and trailing edge the last one. The results show that a shock is captured at the leading edge in three grid points.

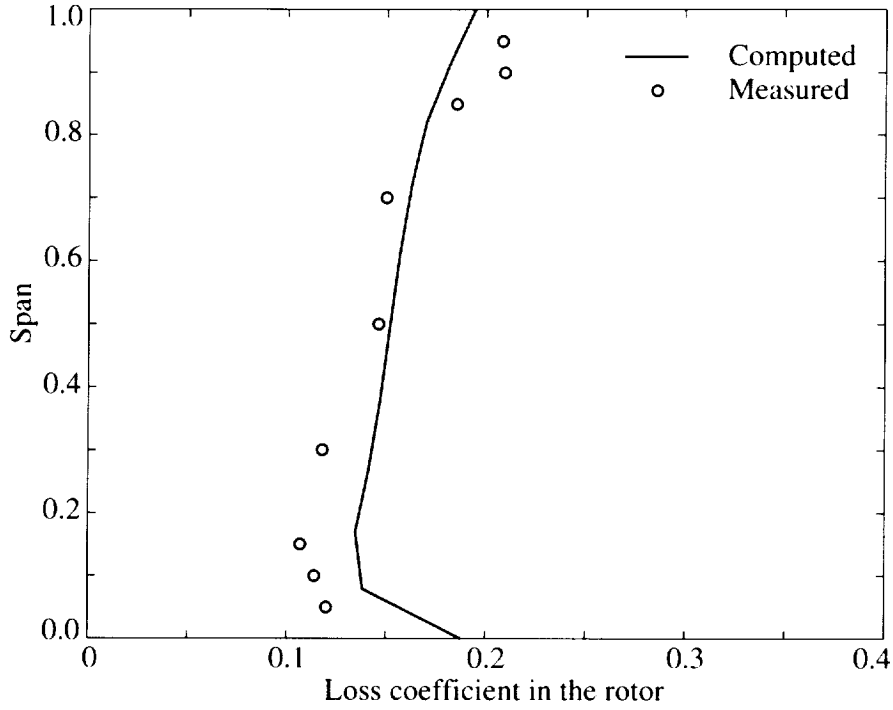

Figure 6.10: The computed and measured [58] loss coefficient profiles of Rotor 35 at 100% rotational speed and 20.2 kg/sec mass flow rate.

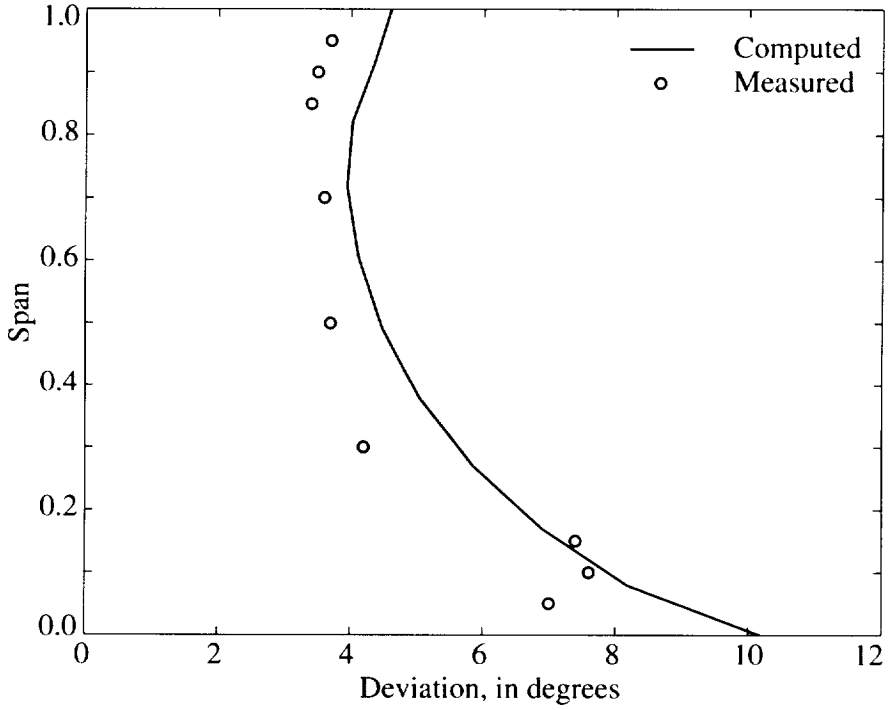

Figure 6.11: The computed and measured [58] deviations of Rotor 35 at 100% rotational speed and 20.2 kg/sec mass flow rate.

6.3.1 Stage 35 Compressor Response to a Steady Total Pressure Distortion

In this section, computed results of Stage 35 response to inlet distortion are presented and compared with available measurements. At the far upstream location, the total pressure distortion is a 120° square-wave with a total pressure deficit of one dynamic head, i.e.

$$\frac{P_{spoiled} - P_{unspoiled}}{\frac{1}{2}\rho V_x^2} = 1.0$$

The total and static pressure distributions at the upstream location (noted in Fig. 6.4) and static pressure distribution at the specified downstream location are plotted in Fig. 6.12. As shown in the figure, the results are in agreement with the measurements. The non-uniform static pressure at the downstream location of Stage 35 is a result of the downstream diffuser (Spakovszky et al [65]). The computed velocity distribution at the specified upstream location also matches the measurement (Fig. 6.13). The good agreement between computed and measured flow field has the implication that the computed results can be used to further examine the flow field in the compressor.

One significant feature of distorted flow field in the compressor is the resulting flow redistribution associated with distortion-compressor coupling. As shown in Fig. 6.15, the flow coefficient distribution at the compressor front face has been significantly altered from that at the upstream location of the compressor. The non-uniformity of flow coefficient has been attenuated by the compressor. The reason for this type of redistribution is that in the low flow coefficient region the compressor has a higher pressure rise than the compressor in the high flow coefficient region. Besides the reduction of the flow coefficient non-uniformity at the compressor inlet, the shape of the flow coefficient distribution has also been shifted in phase. An interesting observation is that the direction of the shift predicted by an actuator disk theory of Hynes and Greitzer [35] is opposite to the direction computed using the current model (shown in Fig. 6.16). The shift in flow coefficient profile at the compressor inlet face in Hynes and Greitzer's model is due to the rotation of the rotor

which transports momentum in the direction of rotor rotation. In the current model, the effects of transporting momentum by the rotor is outweighed by the change in inlet flow angle caused by the flow redistribution, as illustrated in Fig. 6.17. Hynes and Greitzer [35] assume that there is an IGV in front of the rotor, therefore flow angle is set by the IGV exit angle; however Stage 35 does not have an IGV and is a single stage compressor (which implies that rotor rotation effects are relative small), therefore the effects of inlet flow angle change become the dominant mechanism for phase shifting of the flow coefficient profile at the inlet of Stage 35. Thus one may expect that the response of a single stage compressor will be similar to the behavior of Stage 35, while a multi-stage compressor would response in a manner similar to that described by Hynes and Greitzer [35].

The velocity distributions from far upstream to the compressor exit are plotted in Fig. 6.14. The flow is approximately two-dimensional with three-dimensional flow feature (i.e. radial non-uniformity) near the edges of the square-wave. The total pressure distribution (Fig. 6.18) and total temperature distribution (Fig. 6.19) at the compressor exit show that both the total pressure and total temperature are significantly non-uniform even though the distortion at the inlet is a purely total pressure distortion.

Figure 6.20 shows the local operating points at different circumferential positions on the compressor map. It is found that the spoiled sector and the unspoiled sector of the compressor do not operate along the same speedline. The mass flow range around the annulus is larger than the flow range from maximum (choked) to stalling mass flow for the compressor operated at the same speed. The fairly large spread in the computed compressor operating points around the compressor annulus indicates that the compressor is not operating in a manner described by the "compressor in parallel" model. This is because a significant flow angle variation (shown in Fig. 6.21) is induced by the flow redistribution at the rotor inlet as being illustrated in Fig. 6.17; and the induced inlet flow angle deviates the compressor performance from the compressor performance map.

Another effect of the inlet distortion is the resulting non-uniform blade loading

on the blades around the annulus. Figure. 6.22 shows the computed rotor blade force distribution along the circumferential direction. The force variation is more than 40% of the mean value. This information is useful for structural designers for estimating the blade structure integrity under inlet distortions.

To summarize, this example demonstrates the utility of the method for calculating finite amplitude disturbance.

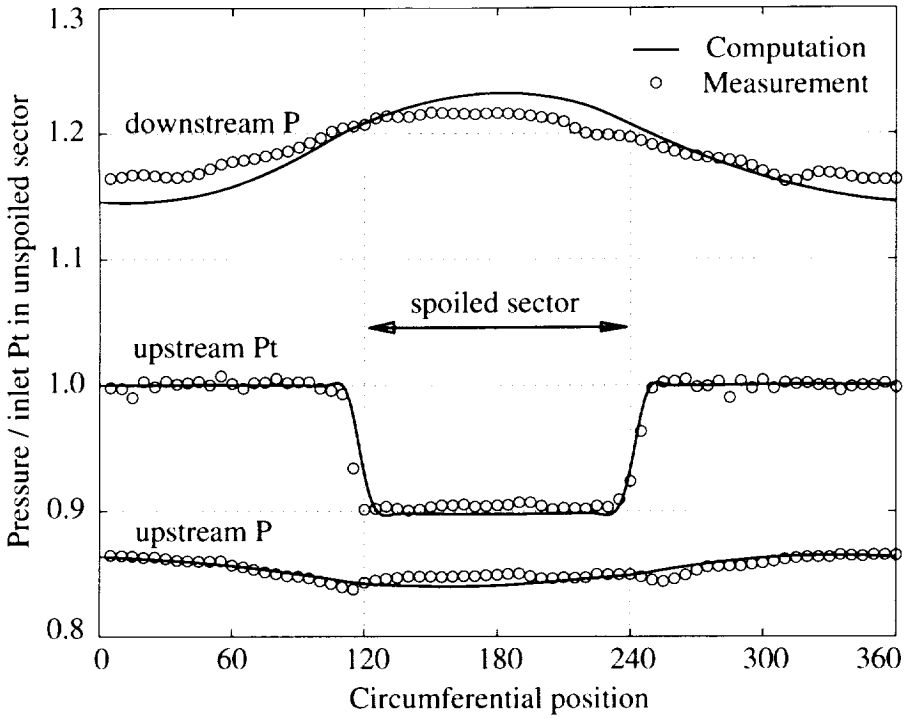

Figure 6.12: The computed and measured [65] total and static pressure at the upstream and downstream locations of Stage 35.

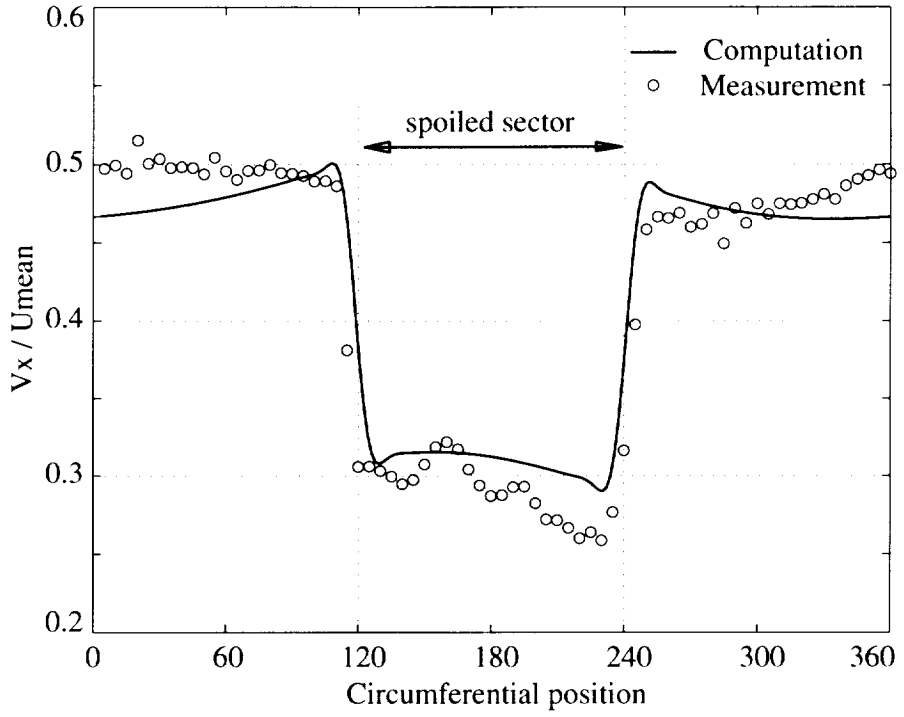

Figure 6.13: The computed and measured [65] flow coefficient at the upstream location of Stage 35.

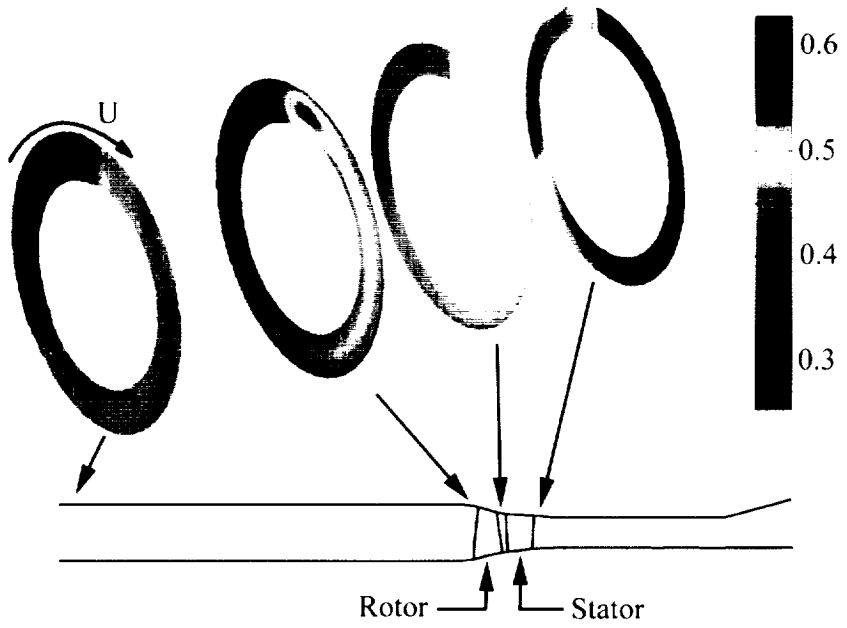

Figure 6.14: The computed axial velocity distributions at the upstream location, rotor inlet, rotor exit, and stator exit. The 120° low P_t sector is imposed far upstream.

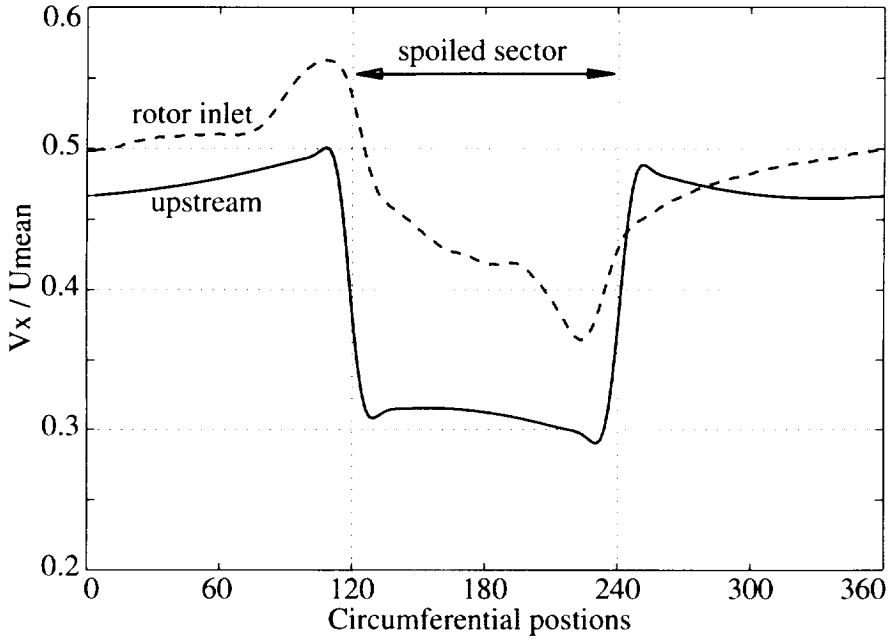

Figure 6.15: Computed flow coefficient distributions at the upstream location and the rotor inlet.

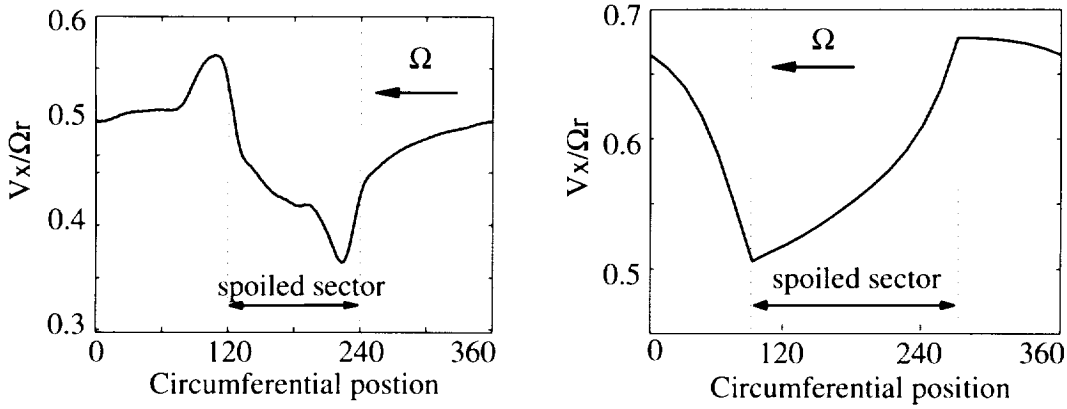

a) Stage 35

b) Hynes-Greitzer compressor

Figure 6.16: Computed axial velocity distribution at the rotor inlet of Stage 35 versus velocity distribution at the rotor inlet of the compressor in Hynes and Greitzer [35].

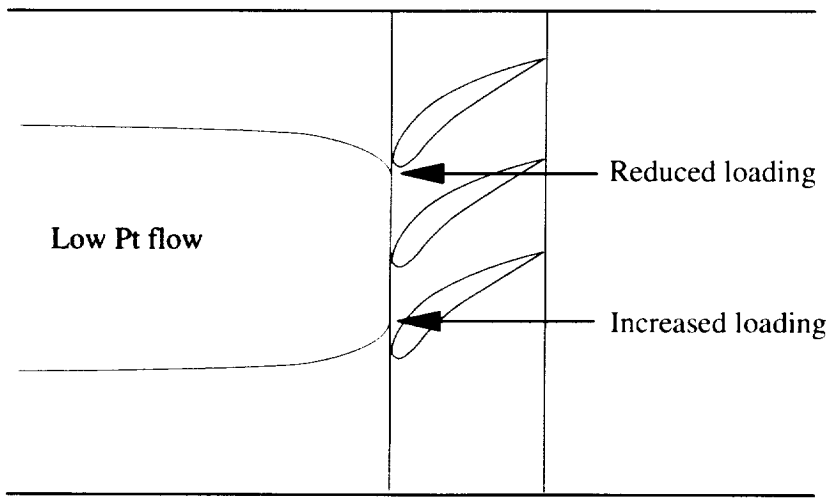

Figure 6.17: The loading on the front rotor is changed due to the induced swirl at the compressor inlet.

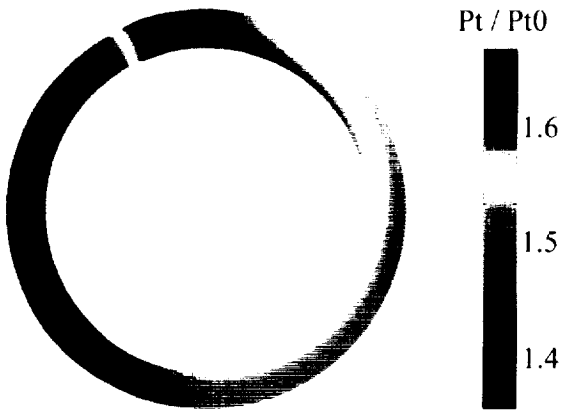

Figure 6.18: The computed total pressure distributions at the exit of the compressor with total pressure distortion upstream.

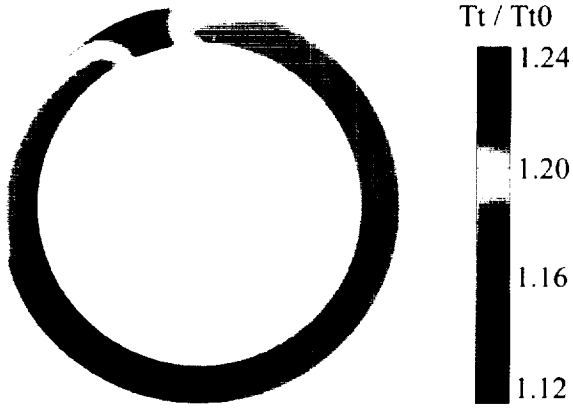

Figure 6.19: The computed total temperature distributions at the exit of the compressor with total pressure distortion upstream.

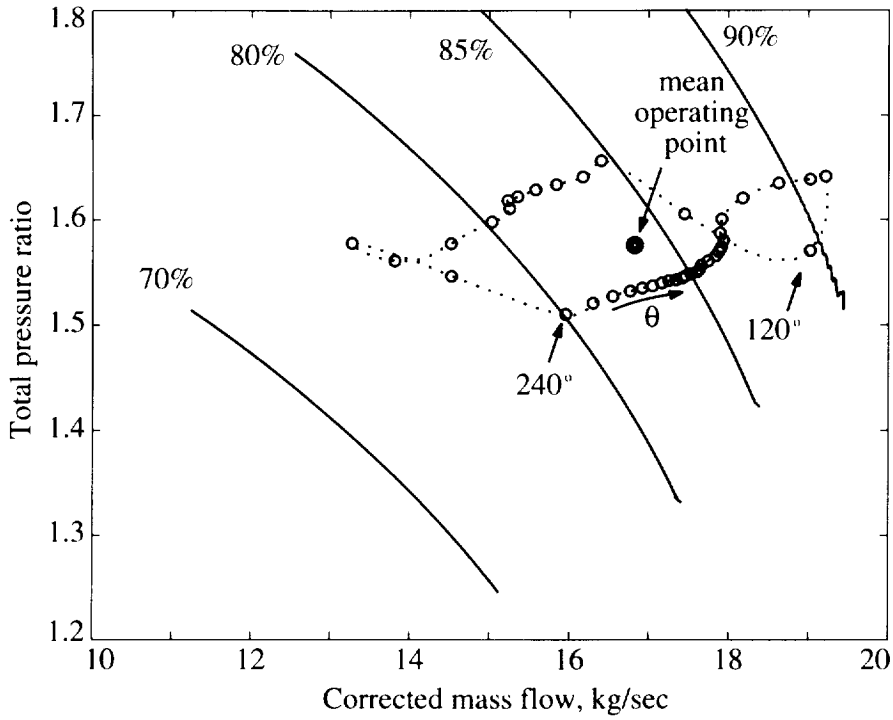

Figure 6.20: The local operating point around the annulus of Stage 35 subjected to a far upstream square wave total pressure distortion.

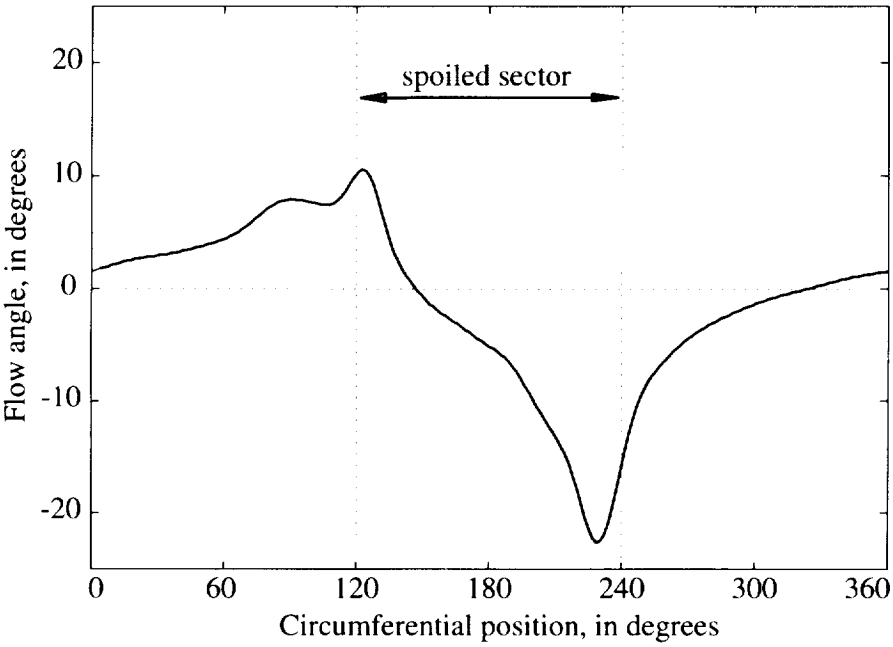

Figure 6.21: The flow angle distribution at the mid-span of the rotor inlet for Stage35 with a total pressure distortion upstream.

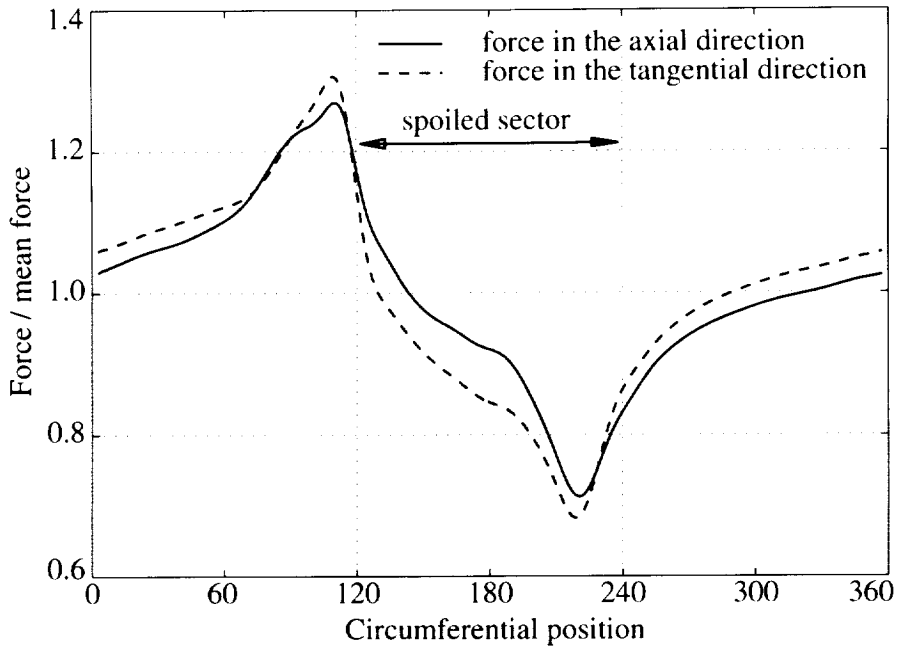

Figure 6.22: The distributions of the aerodynamic force on blades along the annulus.

6.3.2 Stage 35 Compressor Response to Total Temperature Distortion

In this case, a 120° square-wave total temperature distortion is imposed far upstream of Stage 35. The total temperature ratio ($T_{t,distorted}/T_{t,undistorted}$) is 1.47, or the temperature distortion coefficient, $(T_{t,max} - T_{t,mean})/T_{t,mean}$, is 0.16. The temperature non-uniformity can also be measured by $(T_{t,distorted} - T_{t,undistorted})/0.5U^2_{mean}$, which gives 2.5. The spoiled (higher T_t) sector is operated at 70% corrected speed.

The axial velocity distributions from far upstream to downstream of the compressor, shown in Fig. 6.23, reveal the flow redistribution in the compressor. Figure 6.24 shows the change of axial velocity profile from the upstream location to the compressor front face. The flow in high total temperature region is not accelerated as does the flow in low total temperature region. The high total temperature region is thus expanded as the flow approaches the compressor. The compressors-in-parallel model can again be used to qualitatively explain this. The portion of the compressor with high total temperature inlet flow has to operate at an operating point in the low mass

flow region, and the other portion at an operating point of high mass flow, so that the static pressure at the exit is approximately uniform. Therefore, the distorted flow region has to be decelerated, and this leads to the expansion of distorted flow region to satisfy the continuity. Due to the flow redistribution, the swirl is induced at the edges of distorted and undistorted flow. The velocity distributions at the rotor exit and stator exit can be explained by the loading variation caused by the induced swirl. The total temperature distribution at the exit (Fig. 6.25) is consistent with the above explanation. The low total temperature region is reduced at the rotor exit. At the compressor exit, a total pressure non-uniformity is produced by the compressor.

The local operating points on the annulus are plotted in Fig. 6.27. In this case, the"parallel compressor" model appears to be a good approximation (comparing with the case of total pressure distortion). The flow angle variation at the rotor inlet, shown in Fig. 6.28, is about 20% of the variation for the total pressure distortion case (Fig. 6.21); this explains why the "parallel compressor" model is a good approximation for this case.

The distribution of the aerodynamic force on blades (Fig. 6.29) shows a substantial variation caused by the total temperature distortion.

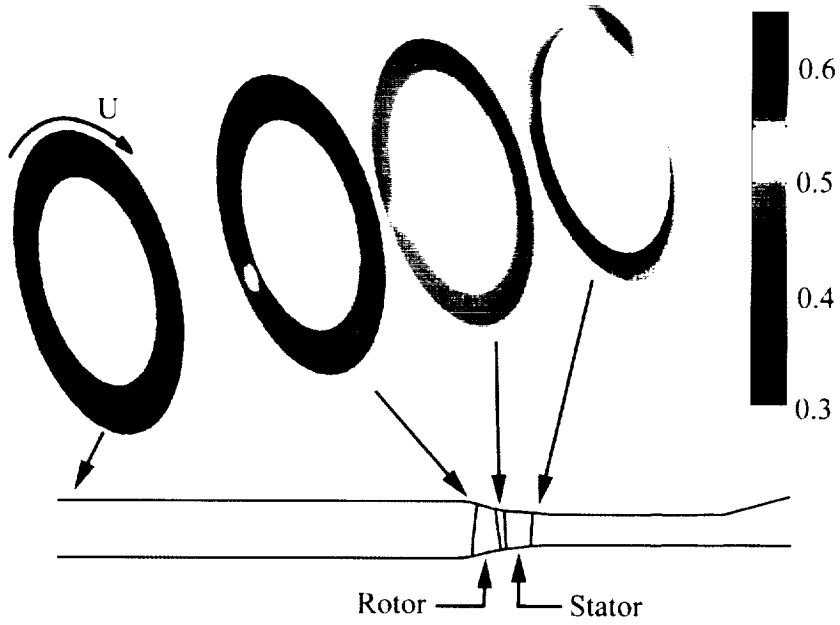

Figure 6.23: The computed axial velocity distributions far upstream, at the rotor inlet, rotor exit, and stator exit. A square wave total temperature is imposed far upstream of the compressor.

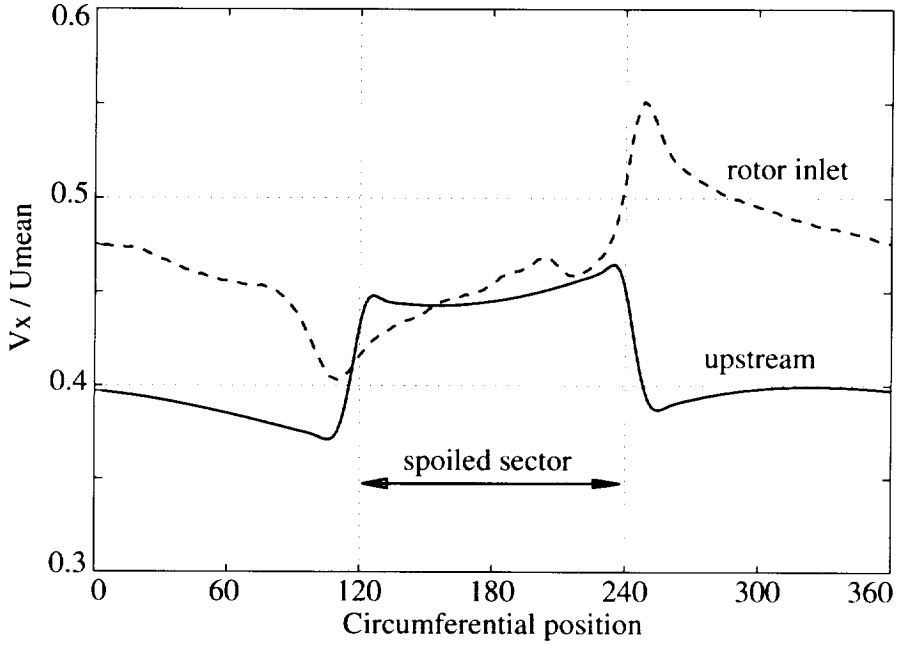

Figure 6.24: The computed flow coefficient distributions upstream and at rotor inlet for Stage 35 with inlet Tt distortion.

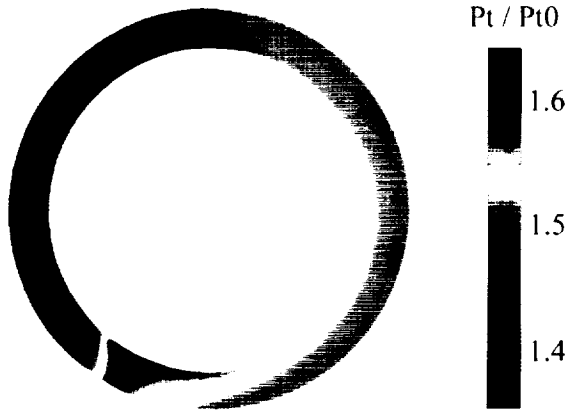

Figure 6.25: The computed total pressure and total pressure distributions at the exit of the compressor with a total temperature distortion upstream.

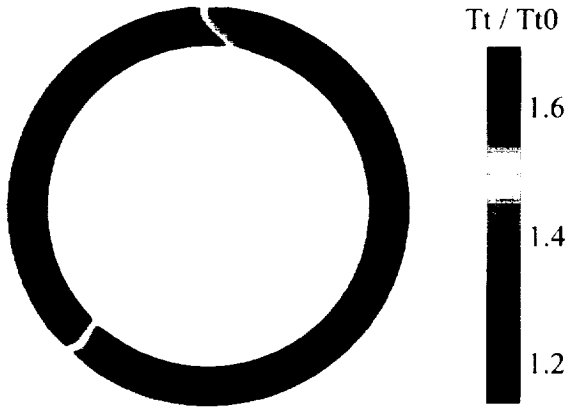

Figure 6.26: The computed total pressure distributions at the exit of the compressor with a total temperature distortion upstream.

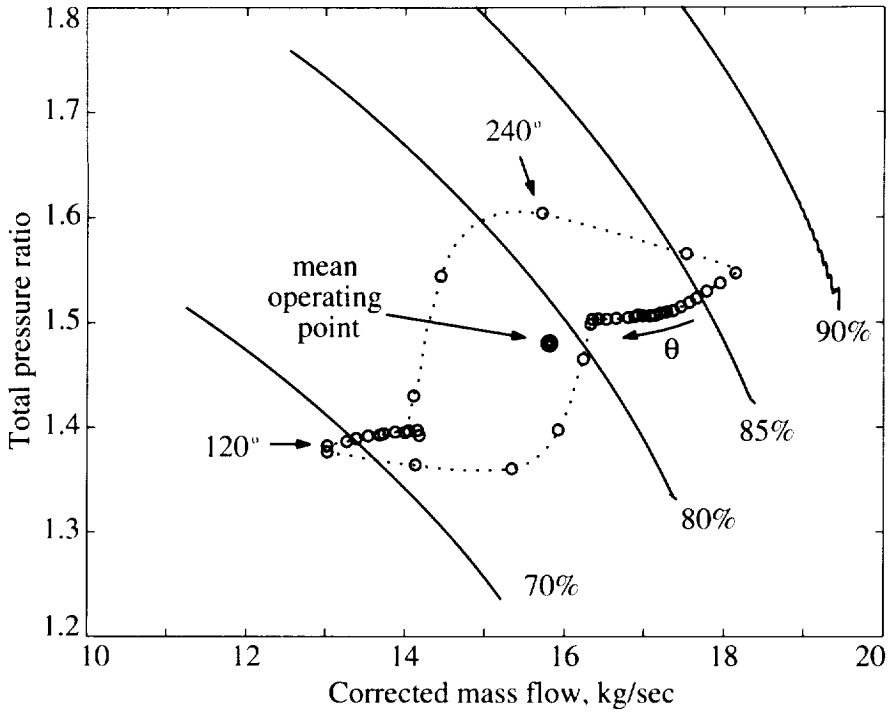

Figure 6.27: The local operating point around the annulus of Stage 35 subjected to a far upstream square wave total temperature distortion.

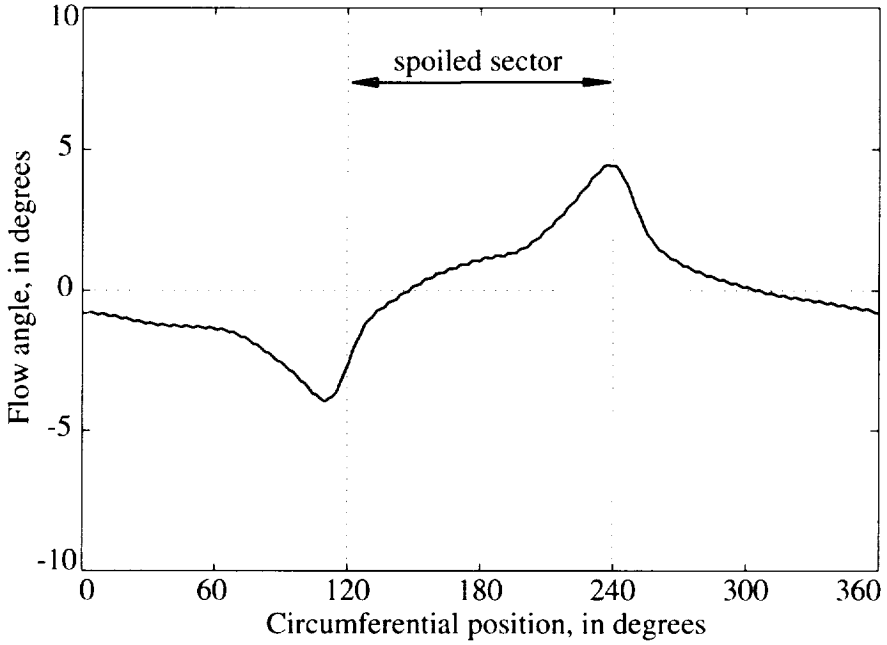

Figure 6.28: The flow angle distribution at the mid-span of the rotor inlet for Stage 35 with a total temperature distortion upstream.

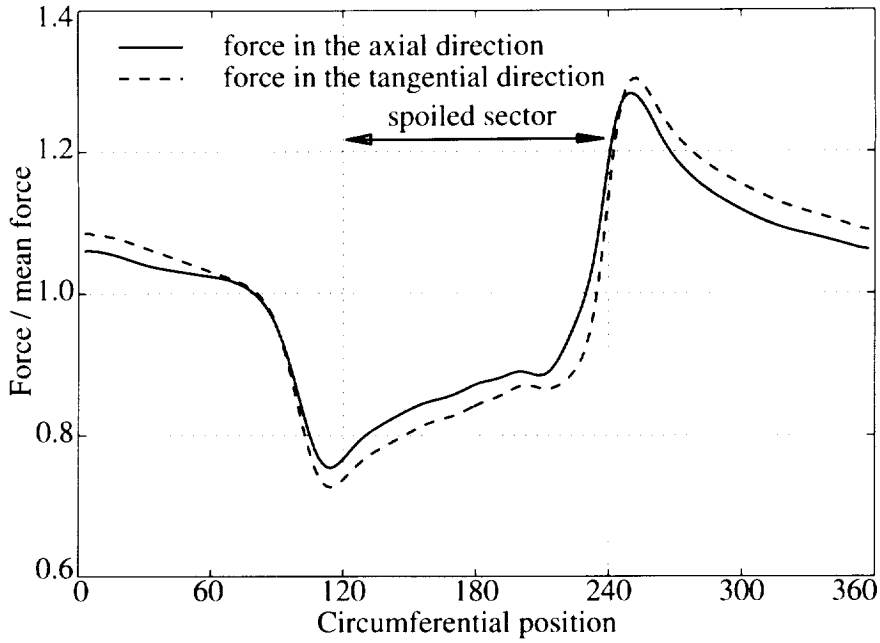

Figure 6.29: The distributions of the aerodynamic force on blades around the annulus.

6.4 Stage 35 response to an abrupt total pressure distortion

A feature of the present model is its ability to simulate the unsteady response of a compressor to non-linear disturbances. To demonstrate this, the response of Stage 35 to an abrupt total pressure inlet distortion is computed. A total pressure distortion, which is the same as that in Section 6.3.1, was imposed at the upstream boundary at time = 0.

The mass flow and static pressure computed at the upstream station, the compressor inlet, compressor exit, and downstream are plotted in Fig. 6.30 and Fig. 6.31. The results clearly show that the pressure wave (expansion wave) propagating downstream. The reduction of mass flow sweeps through the system following the pressure wave. After the first sweep of the pressure wave, the mass flow at the upstream location drops 1.1kg/sec which is about 50% more than the drop in mass flow as the final steady state is reached. The mass flow in blade row region settles to the value of

the final steady state almost instantaneously; this is due to the presence of the compressor which operates in the negatively sloped region, so the one-dimensional mode is suppressed by the compressor. The mass flow at the upstream location increases as the reflected pressure wave from the compressor reaches the upstream location at time = 0.6 revs. Fig. 6.32 shows the flow coefficient profiles at four time instants. At time = 0.33 revs, when the pressure wave reaches the compressor inlet, the flow coefficient is fairly uniform. The flow coefficient at the rotor inlet begins to deform as the low Pt flow reaches the compressor inlet at time = 0.78 revs. The flow pattern at the compressor inlet is roughly established at time = 1.17 revs, only 0.39 revs after the low Pt flow reaches the compressor. The difference between flow coefficient profiles at time = 1.17 revs and equilibrium state (time = infinite) is minimal. So the flow pattern around a compressor is established almost instantaneously for an abrupt inlet distortion.

The results indicate that a steady model is valid for estimating the performance of a compressor with transient inlet distortions. This statement is valid for a compressor operated near its design point, since all the unsteady disturbances are highly damped by the compressor. It is expected that the phenomena can be substantially different when a compressor is operated near its stall point.

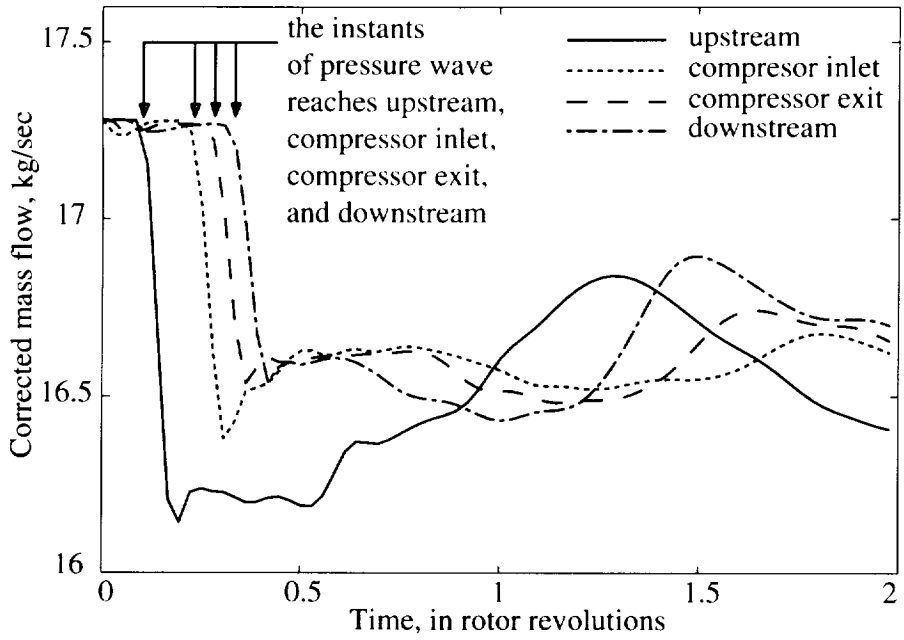

Figure 6.30: The computed mean mass flow traces at the upstream location, compressor inlet, compressor exit, and downstream location. An abrupt inlet Pt distortion is imposed into the system at time = 0 revs.

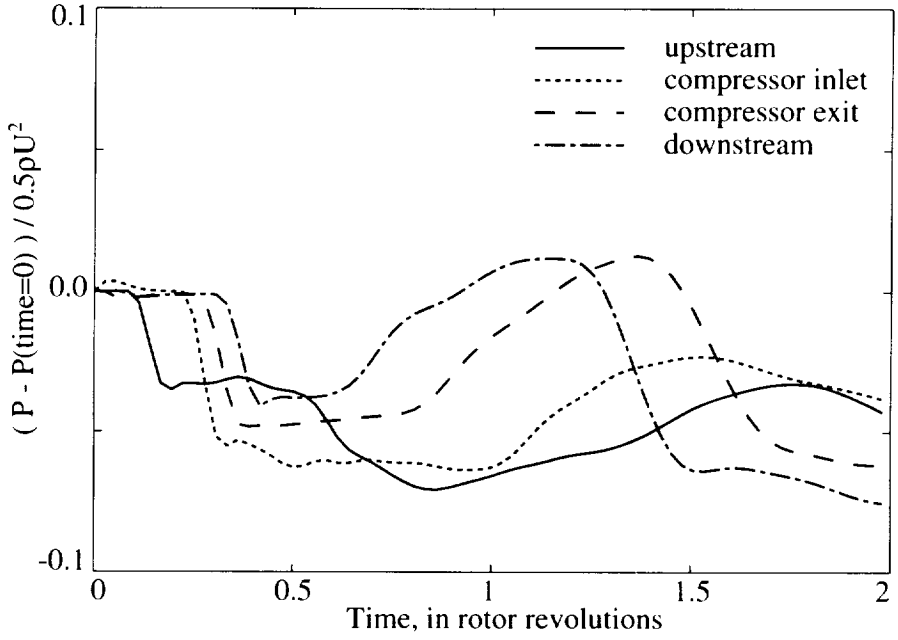

Figure 6.31: The computed mean static pressure traces at the upstream location, compressor inlet, compressor exit, and downstream location. An abrupt inlet Pt distortion is imposed into the system at time = 0 revs.

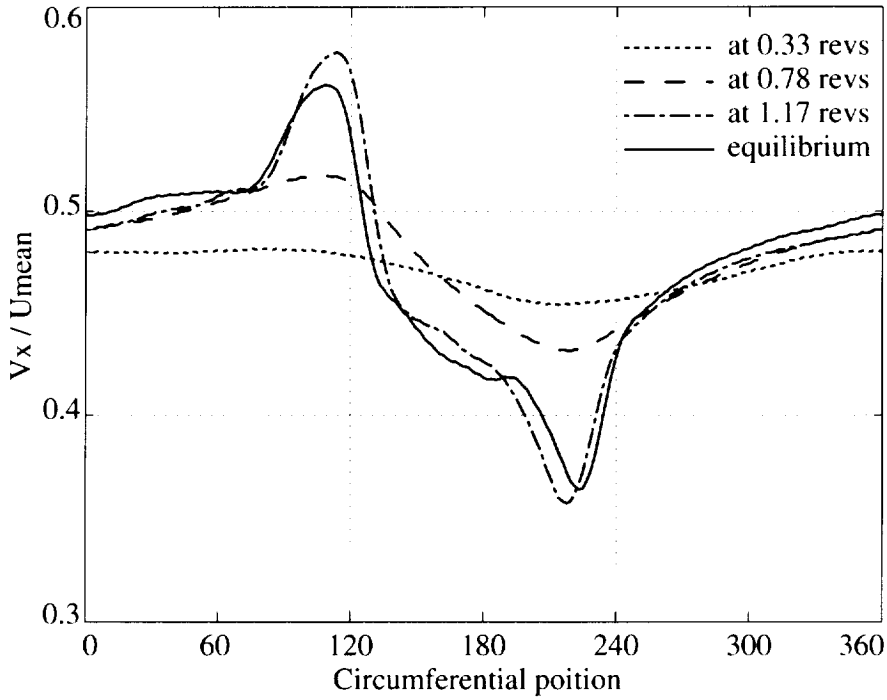

Figure 6.32: The computed flow coefficient profiles at the mid-span of the compressor inlet at four time instants. An abrupt inlet Pt distortion is imposed at the far upstream location at time = 0 revs.

6.5 Summary

1. The methodology developed for low speed compressor is also applicable to high-speed compressor. A new body force formulation has been developed, and is able to capture two unique features associated with high-speed flow: choking and shock waves. The methodology has been shown to be capable of calculating the behavior of compressor response to finite amplitude unsteady disturbances.

2. Computed results for total pressure and temperature distortions show that the use of a simple body force representation gives an adequate description of the flow redistribution in a compressor and the transmission of distortions through the compressor.

3. The response of a compressor to an abrupt Pt inlet distortion was calculated. The results show that the flow pattern around the compressor was established quickly (within 0.4 rotor revolutions after the low Pt flow reaches compressor inlet) when the compressor is operated near its design point. Thus the steady solution for inlet distortion can be used to calculate the flow field and performance of a compressor with transient distorted inlet conditions when the compressor is operated away from its stall point.

4. The results indicate that a compressor under a total temperature inlet distortion can be well described by the "parallel compressor" model, while a compressor with total pressure distortions can only be qualitatively described by the "parallel compressor" model.

5. At compressor exit, both the total temperature and total pressure non-uniformity are significant even though the inlet distortion is merely a non-uniform P_t or a non-uniform T_t.

6. The aerodynamic force on blades along the annulus is computed. It is found that inlet distortion could cause large variation (in the range of 40% of the mean value) of force on blades along the annulus.

Chapter 7

Summary and Conclusions, and Future work

This work is aimed at developing a capability to predict instability onset in multistage compressors with or without inlet distortions. To accomplish this, a computational model has been developed and demonstrated to be capable of describing short wavelength stall inception in a multi-stage compressor. The methodology has further been extended to model high-speed compressor, where it was used to calculate the response of a transonic compressor to different types of inlet distortion. The work will be summarized in this chapter. Several conclusions can be deduced from the computed results presented in this thesis.

7.1 Summary

The thesis presents a complete modeling development process that involves analyzing the experimental observations, conceptualization and development of an adequate physical flow model, followed by its application to seek out specific controlling parameters on short wavelength stalling behavior.

The review presented in Chapter 1 has shown that (1) the rotating stall inception, e.g. short wavelength stall inception, is essentially three-dimensional in many compressors; (2) the short wavelength stall inception, which is initiated by local dis-

turbances, is not just set by local flow condition of one particular blade passage; (3) the rotating speed of short wavelength disturbances can be estimated by the pressure balance (or inertia) method. No available method has the capability of describing the short wavelength stall inception, except a full Navier-Stokes simulation. The goal of the work is therefore to develop a method for describing the rotating stall inceptions in multi-stage compressors.

The computational method (Chapter 2) describes three-dimensional non-linear disturbances in a multi-stage compressor. The key elements of the model are: (1) the row-by-row description of a compressor; (2) the unsteady three-dimensional flow in blade-free regions, and locally axisymmetric flow with body force field in blade row regions; and (3) body force response to the local flow conditions.

It is found that a spike-shaped disturbance (local to the tip region of rotor blade row) is needed to initiate and distinguish the stall inception type of a compressor. The experimental observations also show the existence of this type of localized disturbances prior to stall.

In Chapter 3, the adequacy of the model is assessed by its ability to reproduce the following key features of short wavelength stall inception: (1) relatively high rotating speed, (2) relatively high growth rate, (3) progressive characteristic of stage one in a mismatched configuration of the GE four-stage compressor, (4) the size of the localized stall cell in the mismatched configuration, and (5) the unique rotor tip incidence at the stall point where rotating stall is initiated by short wavelength disturbances.

The following parameters are examined in Chapter 4: (1) initial disturbance type: long wavelength and localized disturbances, (2) radial position of localized disturbances, (3) axial location of initial disturbances, (4) amplitude of initial disturbance, (5) shape of unstable side of characteristic, and (6) effects of inter-blade row gap. The parametric study leads to the following conclusions: (1) the spike-shaped disturbances localized in the tip region of the first stage rotor are the disturbances that initiate the short wavelength stall inception; (2) the amplitude of the disturbance has to be above a threshold value to initiate a short wavelength stall inception;

and (3) reducing the gap around the first stage rotor suppresses short length scale disturbances, while other gaps have no visible effects on the compressor stability.

Additional physical aspects of the results and the model are discussed in Chapter 5. Neglecting the sensitivity of compressor performance to inlet swirl was shown not to change the nature of localized disturbances. Also the source of the initial spike-shaped disturbance could be a result of the tip-vortex behavior. Three-dimensional aspects, more specifically, the additional length scale in the spanwise direction and the centrifugal effect term, V_θ^2/r, and the presence of the finite amplitude disturbances are needed to initiate a short wavelength stall inception in the tip region of a rotor blade row at an operating point in the negatively sloped region of the pressure rise characteristic. The concept of component group and its implication are discussed. Finally, two hypotheses were put forth: (1) there are several routes through which short length scale disturbances could develop into final one large stall cell; (2) a simple analysis is presented to argue that a compressor with low flow coefficient design tends to stall through spike type.

The method is extended to calculate flow disturbances in high-speed compressors. A general form of a body force to represent blade row is given. Based on that general form, a simple body force formulation is derived and used for calculating compressor response to inlet distortions.

7.2 Conclusions

The following conclusions have been deduced from computed results based on the applications of the model:

1. A computational model has been developed for describing general nonlinear three-dimensional disturbances in multistage compressors.

2. The necessary ingredients of the model to simulate short wavelength stall inception entail an unsteady three-dimensional, nonlinear, row by row representation of compressor response to finite amplitude disturbances. The short length scale

stalling process can not be described if any one of these is missing.

3. Localized disturbances of sufficient amplitude (large enough to effect zero pressure rise in the tip) are required to initiate the short wavelength route to rotating stall.

4. The behavior (growth rate, rotating speed, and the shape) of short length scale disturbances can be adequately described without blade discreteness once such a disturbance is imposed onto the system.

5. The computations show instability occurring on the negatively sloped part of the overall compressor characteristic, in agreement with experimental measurements. This is in direct contrast to results based on two-dimensional modal type of analyses in which the instability will occur at the peak of the characteristic.

6. The growth or decay of small length scale disturbances in a rotor is determined by the design characteristics of the isolated component group consisting of the rotor and its adjoining stators.

7. The point at which stall occurs (i.e. propagating asymmetrical disturbances do not decay) via the short wavelength route is set by the most unstable component group where large amplitude spike disturbances are present.

8. Closing the rotor-stator gaps within the most unstable component group suppresses the growth of short wavelength disturbances, thereby improving compressor stability.

7.3 Recommendations for Future Work

Two central issues of short wavelength stall inception are: (1) predicting the compressor stability, and (2) strategies for improving the compressor stability margin. The following work might significantly improve our knowledge of this phenomenon, and the design method for an engine with enhanced stability properties.

1. Incorporating the compressor model developed in this thesis into the existing design tools would provide a viable design method for predicting stall margin. The current method requires substantial amount of input data to describe body force over a large operating range. The body force can be obtained based on other currently available tools (Streamline Curvature calculation, three-dimensional N-S calculation). Building a standard interface between the current model and the Streamline-Curvature or blade passage simulation will represent a substantial advancement of the method in terms of usability.

2. Further study of the controlling parameters on rotating stall initiated by short length scale disturbances would be fruitful. The study would identify these important parameters which have strong impact on the growth of short length scale disturbances, therefore it would provide design guidelines for a compressor which is more tolerant to short length scale disturbances. Some possible controlling parameters are radial loading distribution, axial chord, loading distribution between rotor and stator.

3. Further investigation of the physical origin(s) of the initial disturbances. This would complete the current knowledge of all pieces of the stalling process initiated by short length scale disturbances.

4. It seems of interest to examine the effects of casing treatment as well as tip blowing or suction on short wavelength stall inception. Since the tip region is most sensitive to short length scale disturbances, any modification of the flow structure in the tip region might have significant impact on short wavelength stall inception.

A strength of the model is that the compressor is naturally coupled with unsteady three-dimensional flow, so that the model could be used to investigate the interactions between compressor and other components. Some of these are:

1. Interaction between intake and compressor with inlet distortions (including transient inlet distortions), and its impact on the performance and stability

margin.

2. The behavior of inlet vortex in an intake and engine, and its impact on the performance and stall margin.

3. The hot gas ingestion into an engine, and its impact on the stability margin.

4. The model can be a component in a engine (or even a aircraft) system to model the dynamic behavior of a whole engine under various real situations.

Bibliography

[1] Adkins, G. G., and Smith, L. H. "Spanwise Mixing in Axial Flow Turbomachines," *ASME Journal of Engineering for Power* Vol. 104 (1982), pp.97-110

[2] Bry, P., Laval, P., Billet, G. "Distorted Flow Field in Compressor Inlet Channels," *ASME Journal of Engineering for Gas Turbines and Power* Vol. 107 (1985), pp.782-791

[3] Billet, G., Huard, J., Chevalier, P. and Laval, P. "Experimental and Numerical Study of the Response of an Axial Compressor to Distorted Inlet Flow," *ASME Journal of Fluids Engineering* Vol. 110 (1988), pp.355-360

[4] Camp, T. R. "Aspects of The Off-Design Performance of Axial Flow Compressors," Ph.D. Dissertation, University of Cambridge (1995)

[5] Camp, T. R. and Day, I. J. "A Study of Spike and Modal Stall Phenomena in a Low-Speed Axial Compressor," ASME paper No. 97-GT-526 (1997)

[6] Chue, R., Hynes, T. P., Greitzer, E. M., and Tan, C. S. "Calculations of Inlet Distortion Induced Compressor Flow Field Instability," *International Journal of Heat and Fluid Flow*, Vol. 10 (1989), pp.211-223

[7] Cumpsty, N. A., and Greitzer, E. M. "A Simple Model for Compressor Stall Cell Propagation," *ASME Journal of Engineering for Power* Vol.104 (1982), pp.170-176

[8] Day, I. J., "Axial Compressor Stall," Ph.D. Dissertation, Cambridge University, (1976)

[9] Day, I. J. "Stall Inception in Axial Flow Compressors," *ASME Journal of Turbomachinery* Vol. 115 (1993), pp.1-9

[10] Day, I. J. "Active Suppresion of Rotating Stall and Surge in Axial Compressors" *ASME Journal of Turbonachinery* Vol. 115 (1993) pp. 40-47

[11] Day, I. J., Breuer, T., Escuret, J., Cherrett, M., and Wilson, A. "Stall Inception and The Prospects for Active Control in Four High Speed Compressors," ASME paper 97-GT-281 (1997)

[12] Day, I. J. Personal Communication (1997)

[13] Denton, J. D. "Throughflow Calculations for Transonic Axial Flow Turbines" *ASME Journal of Engineering for Power* Vol.100 (1978), pp.212-218

[14] Dunham, J. "Non-Axisymmetric Flows in Axial Compressors" *mechanical Engineering Science* Monograph No. 3 (1965)

[15] Emmons, H. W., Pearson, C. E., and Grant, H. P. "Compressor Surge and Stall Propagation" *Transactions of The ASME* Vol.79 (1955), pp.455-469

[16] Epstein, A. H., Ffowcs Williams, J. E., and Greitzer, E. M. "Active Suppression of Aerodynamic Instabilities in Turbomachines," *AIAA Journal of Propulsion and Power* Vol. 5 (1989), pp.204-211

[17] Escuret, J. F. and Garnier, V., "Numerical Simulations of Surge and Rotating Stall in Multi-Stage Axial-Flow Compressors," AIAA paper No. 94-3202 (1994)

[18] Escuret, J. F., and Garnier, V. "Stall Inception Measurements In A High-speed Multi-Stage Compressor," ASME paper 95-GT-174, (1995)

[19] Felici, "A Coupled Eulerian/Lagrangian Method for the Solution of Three-Dimensional Vortical Flows," Ph.D. Thesis, Massachusetts Institute of Technology, (1992)

[20] Flitcroft, J. E., Dunham, J., and Abbott, W. A. "Transmission of Inlet Distortion Through A Fan," *Engine Response to Distorted Inflow Conditions* AGARD-CP-400 (1986)

[21] Gallimore, S.J., and Cumpsty, N. A. "Spanwise Mixing in Multistage Axial Flow Compressors Part I: Experimental Investigation," *ASME Journal of Turbomachinery* Vol.108 (1986), pp.2-9

[22] Gallimore, S.J. "Spanwise Mixing in Multistage Axial Flow Compressors Part II: Throughflow Calculations including Mixing," *ASME Journal of Turbomachinery* Vol.108 (1986), pp.10-16

[23] Garnier, V.H., Epstein, A.H., and Greitzer, E.M. "Rotating Waves as a Stall Inception Indication in Axial Compressors," *ASME Journal of Turbomachinery* Vol.113 (1991), pp.290-301

[24] Gordon, K. M. Personal communication, (1994)

[25] Greitzer, E. M., 1976 "Surge and Rotating Stall in Axial Flow Compressors, Part I and II," *ASME Journal of Engineering for Power* Vol. 98 (1976), pp.190-217

[26] Greitzer, E. M., "The Stability of Pumping System The 1980 Freeman Scholar Lecture," *ASME Journal of Fluids Engineering*, Vol. 103 (1981), pp.193-242

[27] Greitzer, E. M., Strand, T. "Asymmetric Swirling Flows in Turbomachine Annuli," *ASME Journal of Engineering for Power*, Vol. 100 (1978), pp.618-629

[28] Hale, A., O'Brien, W. "A Three-Dimensional Turbine Engine Analysis Compressor Code (TEACC) for Steady-State Inlet Distortion," ASME paper 97-GT-124 (1997)

[29] Hawthorn, W. R., Mitchell, N. A., McCune, J. E., and Tan, C. S. "Nonaxisymmetric Flow through Annular Actuator Disks: Inlet Distortion Problem," *ASME Journal of Engineering for Power* Vol. 100 (1978) pp.604-617

[30] Haynes, J. M., Hendricks, G. J., and Epstein, A. H., "Active Stabilization of Rotating Stall in a Three-Stage Axial Compressor," *ASME Journal of Turbomachinery* Vol. 116 (1994) pp.226-239

[31] He, L. "Computational Study of Rotating-Stall Inception in Axial Compressors," *AIAA Journal of Propulsion and Power* Vol. 13, No. 1 (1997) pp.31-38

[32] Hendricks, G. J., Sabnis, J. S., and Feulner, M. R. "Analysis of Instability Inception in High-Speed Multistage Axial-Flow Compressors," *ASME Journal of Turbomachinery* Vol. 119 (1997) pp.714-722

[33] Horlock, J. H., and Marsh, H. "Flow Models for Turbomachines," *Journal Mechanical Engineering Science* Vol. 13 No. 5 (1971)

[34] Hoying, D. A., Tan, C. S., Vo, H. D., and Greitzer, E. M. "Role of Blade Passage Flow Structures in Axial Compressor Rotating Stall Inception," ASME paper 98-GT-588 (1998)

[35] Hynes, T. P., and Greitzer, E. M. "A Method for Assessing Effects of Inlet Flow Distortion on Compressor Stability," *ASME Journal of Engineering for Power* Vol.109 (1987) pp.371-379

[36] Iura, T., and Rannie, W. D. "Experimental Investigations of Propagating Stall in Axial-Flow Compressors," *Transactions of The ASME* Vol. (1954), pp.463-471

[37] Jackson, A. D., "Stall Cell Development in an Axial Compressor," *ASME Journal of Turbomachinery* Vol.109 (1987) pp.492-498

[38] Jameson, A., Schmidt, W., and Turkel, E., "Numerical Solutions of the Euler Equations by Finite Volume Methods with Runge-Kutta Time Stepping Schemes," AIAA paper No. 81-1259 (1981)

[39] Koff, S. G., and Greitzer, E. M. "Axisymmetrically Stalled Flow Performance for Multistage Axial Compressors," *ASME Journal of Turbomachinery* Vol. 108 (1986) pp.216-223

[40] Lambie, D. "Inlet Distortion and Turbofan Engines," Ph.D. Dissertation, University of Cambridge (1989)

[41] Lieblein, S. "Experimental Flow in Two-Dimensional Cascades," *Aeronynamic Design of Axial-Flow Compressors* NASA SP-36 (1965) pp.183-226

[42] Longley, J. P., and Hynes, T. P. "Stability of Flow Through Multistage Axial Compressors," *ASME Journal of Turbomachinery* Vol.112, (1990) pp.126-132

[43] Longley, J. P. "A Review of Non-Steady Flow Models for Compressor Stability," ASME paper 93-GT-17 (1993)

[44] Longley, J. P., Shin, H. W., Plumley, R. E., Silkowski, P. D., Day, I. J., Greitzer, E. M., Tan, C. S., and Wisler, D. C., "Effects of Rotating Inlet Distortion on MultiStage Compressor Stability," *ASME Journal of Turbomachinery*, Vol. 118 (1996), pp.181-188

[45] Longley, J. P., "Calculating the Flowfield Behaviour of High-Speed Multi-Stage Compressors," ASME paper No. 97-GT-468 (1997)

[46] Marble, F. E., 1964 "Three-Dimensional Flow in Turbomachines," *Aerodynamics of Turbines and Compressors, Vol. X of High Speed Aerodynamics and Jet Propulsion*, Hawthorne, W. R., ed. Princeton University Press, Princeton, NJ., pp.83-166

[47] Mazzawy, R. S. "Multiple Segment Parallel Compressor Model for Circumferential Flow Distortion," *ASME Journal of Engineering for Power* Vol.99 (1977) pp.288-296

[48] Mazzawy, R. S. "Surge-Induced Structural Loads in Gas Turbines," *ASME Journal of Engineering for Power* Vol.102 (1980) pp.162-168

[49] McDougall, N. M., "Stall Inception in Axial Compressors," Ph.D. Dissertation, Cambridge University (1988)

[50] Moore, F. K., "A Theory of Rotating Stall of Multistage Axial Compressors: Part I-III," *ASME Journal of Engineering for Gas Turbines and Power*, Vol. 106 (1984), pp.313-336

[51] Moore, F. K. and Greitzer, E. M., "A Theory of Post-Stall Transients in Axial Compression Systems: Part I,II," *ASME Journal of Engineering for Gas Turbines and Power*, Vol. 108 (1986), pp. 68-76, pp. 231-239

[52] Motycka, D. L. "Ground Vortex - Limit to Engine/Reverse Operation," *ASME Journal of Engineering for Power* Vol. 98 (1976), pp.258-264

[53] Motycka, D. L. "Reynolds Number and Fan/Inlet Coupling Effects on Subsonic Transport Inlet Distortion," *AIAA Journal of Propulsion* Vol.1 (1985) pp.229-234

[54] Paduano, J., Epstein, A. H., Valavani, L., Longley, J. P., Greitzer, E. M., and Guenette, G. R. "Active Control of Rotating Stall in a Low Speed Axial Compressor," *ASME Journal Journal of Turbomachnary*, Vol.115 (1993)

[55] Paduano, J. D., and Gysling, D. L. "Rotating Stall in Axial Compressors: Nonlinear Modeling for Control," SIAM Conference on Control and its Applications, Minneapolis, (1992)

[56] Park, H. G., "Unsteady Disturbance Structures in Axial Flow Compressor Stall Inception," Master's Thesis, Massachusetts Institute of Technology (1994)

[57] Reid, C. "The Response of Axial Flow Compressors to Intake Flow Distortion," ASME paper 69-GT-29 (1969)

[58] Reid, L., and Moore, R. D. "Performance of Single-Stage Axial-Flow Transonic Compressor with Rotor and Stator Aspect Ratios of 1.19 and 1.26, Respectively, and with Design Pressure Ratio of 1.82," NASA technical Paper 1338 (1978)

[59] Schalkwyk, C. M., Paduano, J. D., Greitzer, E. M., and Epstein, A. H. "Active Stabilization of Axial Compressors with Circumferential Inlet Distortion," ASME paper 97-GT-279 (1997)

[60] Silkowski, P. D., "Measurements of Rotor Stalling in a Matched and a Mismatched Multistage Compressor," GTL Report No. 221 (1995), Gas Turbine Laboratory, Massachusetts Institute of Technology

[61] Smith, L. H. "The Radial-Equibilibrium Equations of Turbomachinery," *ASME Journal of Engineering for Power*, Vol.88 (1966) pp.1-12

[62] Smith, L. H. "Casing Boundary Layer in Multistage Axial-Flow Compressors," *Proceedings of the Symposium on Flow Research on Blading*, (1969) pp.275-304

[63] Soundranayagam, M., and Elder,R. L. "A Study of Stall in a Low Hub/Tip Ratio Fan," *ASME Journal of Turbomachinery*, Vol.115 (1993), pp.10-18

[64] Spakovszky, Z. S., Weigl, J. D., Paduano, J. D., van Schalkwyk, C. M., Suder, K. L., and Bright, M. M., "Rotating Stall Control in a High-Speed Stage with Inlet Distortion, Part I - Radial Distortion" ASME paper 98-GT-264 (1998)

[65] Spakovszky, Z. S., van Schalkwyk, C. M., Weigl, J. D., Paduano, J. D, Suder, K. L., and Bright, M. M., "Rotating Stall Control in a High-Speed Stage with Inlet Distortion, Part II - Circumferential Distortion" ASME paper 98-GT-264 (1998)

[66] Stewart, M. E. M. "Axisymmetric Aerodynamic Numerical Analysis of a Turbofan Engine," ASME paper 95-GT-338 (1995)

[67] Takata, H., and Nagano, S. "Nonlinear Analysis of Rotating Stall," ASME paper 72-GT-3 (1972)

[68] Tryfonidis, M., Etchevers, O., Paduano, J. D., Hendricks, G. F., and Epstein, A. H., "Prestall Behavior of Several High-Speed Compressors," *ASME Journal of Turbomachinery*, Vol. 117 (1995), pp.62-80

[69] Weigl, H. J., Paduano, J. D., Frechette, L. G., Epstein, A. H. and Greitzer, E. M. "Active Stabilization of Rotating Stall and Surge in a Transonic Single Stage Axial Compressor," ASME paper 97-GT-411 (1997)

[70] Williams, D. D. "Review of Current Knowledge on Engine Response to Distorted Inflow Conditions," *Engine Response to Distorted Inflow Conditions*, AGARD-CP-400 (1986)

[71] Wisler, D. C., "Core Compressor Exit Stage Study, Volume IV - Data and Performance Report for the Best Stage Configuration," NASA CR-165357, NASA Lewis Research Center (1981)

Appendix A

A Procedure of Formulating the Body Force

The body force formulation includes the following two steps: (1) determination of a body force field from a given flow field in a blade row; (2) obtaining a set of manageable expressions of the body force field based on sufficient number of body force fields determined applying the method in the previous step for sufficient number of different operating points.

I will first describe a procedure for determining the body force field which will produce a axisymmetric flow field which is the same as that of the pitch-wise average of a given three-dimensional flow field. The procedure is applied to compute the body forces for different operating points; then the body force expression for each spatial point can be deduced from these body forces for different operating conditions.

A.1 Determination of the body force from a three-dimensional flow in a blade passage

A three-dimensional flow field, which can be obtained from either CFD computation or experimental measurement, is expressed as

$$V_x(x,\theta,r)\ ,\ V_\theta(x,\theta,r)\ ,\ V_r(x,\theta,r)\ ,\ T(x,\theta,r)\ ,\ P(x,\theta,r)\ ,\ \rho(x,\theta,r)\ ,\ ...$$

An axisymmetric flow field can be obtained through pitch-wise stream-thrust average of the flow field. Physically, the stream-thrust average assumes the flow is mixed out locally, so this kind of average is consistent to the body force idea. After the pitch-wise average, the flow field can be expressed as

$$V_x(x,r)\ ,\ V_\theta(x,r)\ ,\ V_r(x,r)\ ,\ T(x,r)\ ,\ P(x,r)\ ,\ \rho(x,r)\ ,\ ...$$

The momentum equations with body force terms for the steady flow in a blade row can be written as the following:

$$\frac{\partial}{\partial x}\begin{bmatrix} r\rho V_x^2 + rp \\ r\rho V_x V_\theta \\ r\rho V_x V_r \end{bmatrix} + \frac{\partial}{\partial r}\begin{bmatrix} r\rho V_x V_r \\ r\rho V_\theta V_r \\ r\rho V_r^2 + rp \end{bmatrix} = \begin{bmatrix} r\rho(F_{nx} + F_{px}) \\ -\rho V_\theta V_r + r\rho(F_{n\theta} + F_{p\theta}) \\ \rho V_\theta^2 + p + r\rho(F_{nr} + F_{pr}) \end{bmatrix} \tag{A.1}$$

The force terms in the above equations are

$$\begin{aligned} F_n &= \frac{V_{rel}^2}{h} f_n(M, \Delta\beta) + \frac{1}{\rho}\frac{\partial P}{\partial x}\sin\alpha \\ F_p &= \frac{V_{rel}^2}{h} f_p(M, \Delta\beta) \end{aligned} \tag{A.2}$$

where V_{rel} is the relative velocity. Effectively, formulating of the body force is equivalent to finding f_n and f_p as functions of the local flow conditions.

Integrating Eq. A.1 on a control volume gives

$$\int_{\delta\Gamma}\left(\begin{bmatrix} r\rho V_x^2 + rp \\ r\rho V_x V_\theta \\ r\rho V_x V_r \end{bmatrix}\hat{x} + \begin{bmatrix} r\rho V_x V_r \\ r\rho V_\theta V_r \\ r\rho V_r^2 + rp \end{bmatrix}\hat{r}\right)d(\delta\Gamma)$$

$$= \int_{\Gamma}\begin{bmatrix} r\rho(F_{nx} + F_{px}) \\ -\rho V_\theta V_r + r\rho(F_{n\theta} + F_{p\theta}) \\ \rho V_\theta^2 + p + r\rho(F_{nr} + F_{pr}) \end{bmatrix} d\Gamma \tag{A.3}$$

where Γ is the control volume, $\delta\Gamma$ the surface of the control volume, $\hat{x}$ and $\hat{r}$ unit vectors in the axial and radial directions. If the control volume is a small mesh cell, the value of the right hand side of the Eq. A.3 can be evaluated assuming the flow properties in the mesh cell to be approximately uniform. Then the above equation set becomes

$$\int_{\delta\Gamma}\left(\begin{bmatrix} r\rho V_x^2 + rp \\ r\rho V_x V_\theta \\ r\rho V_x V_r \end{bmatrix}\hat{x} + \begin{bmatrix} r\rho V_x V_r \\ r\rho V_\theta V_r \\ r\rho V_r^2 + rp \end{bmatrix}\hat{r}\right)d(\delta\Gamma)$$

$$= V_\Gamma \begin{bmatrix} r\rho(F_{nx} + F_{px}) \\ -\rho V_\theta V_r + r\rho(F_{n\theta} + F_{p\theta}) \\ \rho V_\theta^2 + p + r\rho(F_{nr} + F_{pr}) \end{bmatrix} \tag{A.4}$$

where V_Γ is the volume of the control volume. F_x, F_θ, and F_r can be computed using the above equation set; and their components normal and parallel to the relative velocity can be calculated. Finally, f_n and f_p can be calculated using their definition in Eq. A.2.

A.2 Deducing f_n and f_p as Functions of Local Flow Properties

In the previous section, f_n and f_p at each mesh cell can be calculated for a given three-dimensional flow field. I label these f_n and f_p as

$$f_{n,(j,k)} \ , \ f_{p,(j,k)}$$

where (j, k) is the index of a mesh cell (Fig. A.1). A simple way of formulating these f_n and f_p is to express them as polynomials, such as

$$\begin{aligned} f_{n,(j,k)} &= C_{n0,(j,k)} + C_{n1,(j,k)}\beta + C_{n2,(j,k)}\beta^2 + C_{n3,(j,k)}M + C_{n4,(j,k)}M^2 \\ f_{p,(j,k)} &= C_{p0,(j,k)} + C_{p1,(j,k)}\beta + C_{p2,(j,k)}\beta^2 + C_{p3,(j,k)}M + C_{p4,(j,k)}M^2 \end{aligned} \tag{A.5}$$

where C_{n0}, ... C_{p4}, are coefficients to be determined. If a sufficient number of f_n and f_p have been computed for different operating points using the method described in the previous section, then C can be determined to have the best fit for these f_n and f_p.

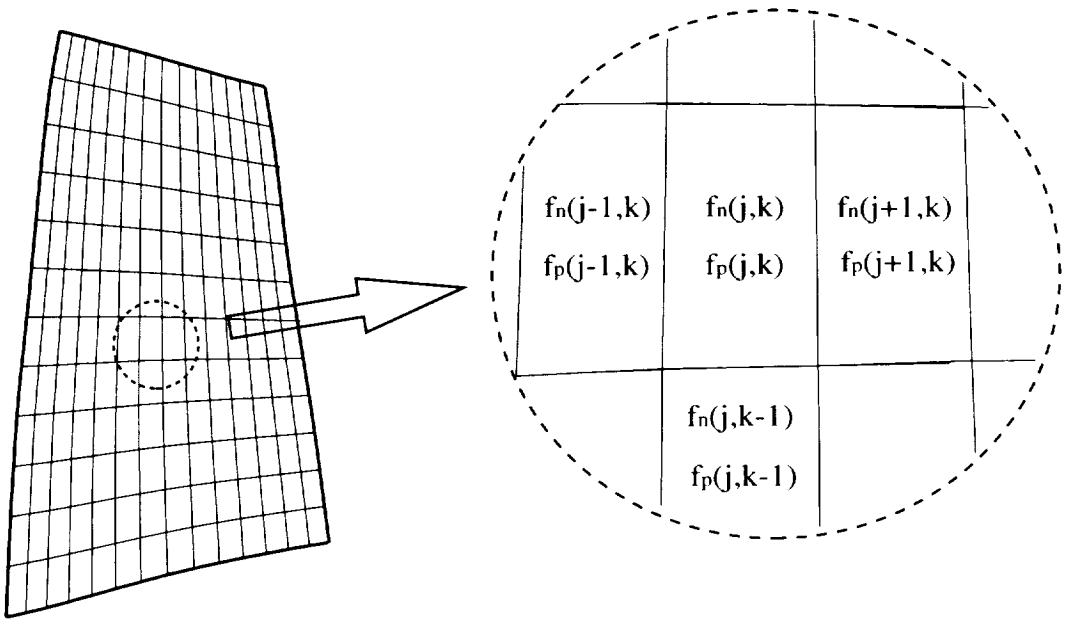

Figure A.1: The f_n and f_p are defined on each cell of the pre-generated mesh.

THREE-DIMENSIONAL AERODYNAMIC INSTABILITIES IN MULTI-STAGE AXIAL COMPRESSORS

Part II: Effect Of Changes In Pressure Rise Characteristics On Short Length Scale Stall Inception And Development Of Rational Procedure For Body Force Representation Of Blade Row

I. Introduction

A computational model for simulating axial compressor stall inception and development via disturbances with length scales on the order of several (typically about three) blade pitches have been developed and this was described in Part I of the report. The model was designed for multi-stage compressors in which stall is initiated by these ``short wavelength" disturbances, also referred to as spikes. The inception process described is fundamentally nonlinear, in contrast to the essentially linear behavior seen in so-called ``modal stall inception". Each blade-row was represented by a body force distribution evaluated in real time using the blade-row characteristics and local flow conditions. The model was able to capture the following experimentally observed phenomena: (1) development of rotating stall via short wavelength disturbances, (2) formation and evolution of localized short wavelength stall cells in the first stage of a mismatched compressor, (3) the switch from long to short wavelength stall inception resulting from the re-staggering of the inlet guide vane, (4) the occurrence of rotating stall inception on the negatively sloped portion of the compressor characteristic. Parametric investigations indicated that (1) short wavelength disturbances were supported by the rotor blade row, (2) the disturbance strength was attenuated within the stators, and (3) the reduction of inter-blade row gaps can suppress the growth of short wavelength disturbances. It is argued that each local component group (rotor plus neighboring stators) has its own instability point (i.e. conditions at which disturbances are sustained) for short wavelength disturbances, with the instability point for the compressor set by the most unstable component group.

However there remain two issues that need to be re-examined. First the use of the computational model for simulating axial compressor instability requires the specification of compressor pressure rise characteristics including the portion of the characteristics to the left of the peak of pressure rise characteristics. This is the portion of the characteristics that one would measure if the compressor were prevented from stall for operating points past the peak. As such this information is not readily available. Thus it would be of engineering interest to assess the sensitivity of the stall inception process and its subsequent development to the portion of the pressure rise characteristics that is to the

left of the peak, which will be referred to as LPSC for brevity. Second only a rudimentary procedure used for representing each blade-row as a body force distribution that was evaluated in real time using the blade-row characteristics and local flow conditions. Thus there is also a need to develop a procedure whereby the body force representation of a blade row can be implemented directly using the best available CFD solution of isolated single blade passage. This part of the report describes the work done toward addressing the two issues delineated in the above for the period January 2000 to December 2000 under NASA GRC Grant NAG3-2051.

A stall inception process through short wavelength in a multistage compressor can be roughly described as the first appearance of localized short length scale disturbances (which can be one or multiple, and begin to manifest hundreds or more rotor revolutions before compressor stalls). Under the appropriate operating conditions, one of the localized disturbances will eventually grow to result in a full span stall cell that extends axially throughout the compressor. To understand this stalling process in a multistage compressor, the following three questions need to be answered:

(1) What set the conditions under which the localized disturbances will form?

(2) What is needed to sustain the localized disturbances around a local blade row?

(3) What are the conditions under which the localized disturbances can grow to result in a fully developed stall cell?

The answer to each of the above three questions reflects the flow phenomena at three different physical level of length and time scale that one has to deal with. The first question is related to the flow phenomena on a blade passage level, the second to the blade row behavior, while the third one is mostly determined by the behavior of the overall system.

The work on addressing the first issue is aimed at answering the second question. In this regard, the importance of the LPSC can be understood through the following argument. The short wavelength stall inception is determined by the manner a compressor responds to localized finite amplitude disturbances. The flow coefficient distribution associated with the localized finite amplitude disturbances covers a finite portion of compressor

characteristic as illustrated in figure 1. It can thus be seen that the slope of the characteristic, while proved adequate in linear stability model (Moore-Greitzer's model), becomes inadequate for describing a compressor instability inception to finite amplitude disturbances.

The second part of the work is an effort to implement the developed methodology for modeling compressor instability in a practical design-oriented environment. The proposed procedure would consist of four steps: (1) extract body force from CFD solutions; (2) formulate the body force based on the extracted body force fields; (3) replace the blade passage region with the formulated body force field; and (4) embed the body force distribution within a standard flow solver in manner that it can be evaluated in real time using the blade-row characteristics and local flow conditions

Key results are presented to provide quantitative illustrations of the effects of changes in LPSC on the short wave length instability and stalling flow coefficient Progress toward developing the procedure for extracting the body force representation from the existing CFD results are described as well.

II. Sensitivity of Stall Inception and Development to Uncertainties in LPSC

The specific goal here is to quantify the shape of LPSC on compressor stalling behavior as measure in terms of the stalling flow coefficient. This is accomplished by implementing a set of stability calculations for a multistage compressor measured unstalled pressure rise characteristics and assumed LPSC that varies by changing the characterizing parameters delineated in the next section.

Procedure for Determining Stalling Flow Coefficient

The calculations and the results to be described here are based on the low speed compressor employed in [1]. It is a mismatched GE 4-stage compressor [2] in which the second to the forth stages have lower peak flow coefficient than that of the first stage. A

consequence of the mismatched configuration is that the first stage shows progressive stalling behavior while maintaining the same stalling flow coefficient. Eight LPSCs (Fig. 2), labeled as baseline, C1, to C7, are investigated. The LPSC shape has a trough between the peak and the zero flow coefficient point; this generic featured has been rationalized to some extent in [1], though concerns have been expressed on the fact that LPSC might not be smooth or continuous. The shape of the LPSC can essentially be characterized in terms of the following parameters: (1) the depth of the bottom of the trough, and (2) the location where a steep drop of pressure rise occurs.

The computational procedure, which has been described by Gong (1998) in details, can be summarized in the following:

(1) At a selected throttle position, a steady (axisymmetric) solution is obtained through running the simulation code (based on the computational model of the compressor) under its axisymmetric mode.

(2) Based on the obtained steady solution, a simulation is then performed by introducing a localized impulse (0.1 rotor revolutions in the actual simulation) to generate a finite amplitude disturbance at the first stage rotor blade row (or other selected blade rows) every two rotor revolutions. The subsequent behavior of disturbances, which might either decay or grow, determines whether the compressor is stable or not. If the compressor is unstable at a particular throttle position, then its final equilibrium state (which can consists of multiple localized stall cells, one large stall cell, or one-dimensional oscillation) determines the type of instability such as stall, or surge.

(3) The stall/surge flow coefficient is determined by the minimum flow coefficient via searching the compressor instability behaviors at various throttle positions. The accuracy of the stalling flow coefficient documented in this report is not exceeding 0.1% of stalling flow coefficient of the baseline case.

Results

The sensitivity of the compressor stalling behaviors to changes in LPSC are quantified in terms of : (1) the change of stall flow coefficient, which is measured as

$$\frac{\phi_{stall} - \phi_{stall,baseline}}{\phi_{stall,baseline}} \times 100\% ,$$

and (2) the shape of localized stall cell, which is reflected in the distribution of flow field at the rotor exit.

The compressor characteristics with eight different LPSC are shown in Figure 2. Three dimensional instability simulations show that all these cases result in progressive stall characteristic due to the mismatched configuration. The shape of stall cells is illustrated using the flow coefficient distributions in the tip region of stage one rotor exit. Shown in Figure 3 to Figure 10 are the first rotor exit flow coefficient distributions corresponding to each of the eight cases. These computed results indicate that the shape of the stall cells is similar in all these cases. In light of the large variation in the LPSC used in these simulations, it can be inferred from these results that the shape of localized stall cells is not sensitive to the variation in LPSC. This is consistent with the measurements reported in[2], [3] and [4]. This observation is in essential agreement with the concept of component group proposed in [1], which yield the result that the growth of localized disturbances is determined by a stator-rotor-stator system. Therefore the geometry, more specifically, the blade chord and inter-blade gap, set the size of localized stall cells.

The stalling flow coefficient of the baseline case is 0.383, which is higher than the flow coefficient of 0.374 at the peak of the prescribed total-to-static pressure rice characteristic of the first stage. The results shown in Figure 11 to 16 serve to illustrate the effects of changing LPSC on the stalling flow coefficient through the following observations:

(1) Figure11 shows the change in stalling flow coefficient for all seven characteristics, and the results show an 8 percent variation in the computed stalling flow coefficient.

(2) Figure12 shows the stalling flow coefficient changes for LPSC that involve a steep drop of pressure rise with the trough at a fixed value of pressure rise. The stalling flow coefficient decreases (hence system stability improves) as the steep drop of the pressure rise occurs at a lower flow coefficient. The results shown in Figure 13 shows a similar trend for LPSC with the trough at a different pressure rise from those in figure 12.

(3) Figure14 shows the stall flow coefficient change for LPSC with different depth of the trough. Figure 15 is similar to Figure14 but with a different location where the steep drop of pressure rise occurs. The results in these two figures indicate that the depth of the trough does have a measurable effect on the stalling flow coefficient. The effect appears to be more significant as the steep drop of the pressure rise occurs at higher flow coefficient.

(4) Figure16 shows the effects of the shape of the characteristic near the peak (from 0.8 to 1 peak pressure rise flow coefficient) on the stalling flow coefficient. The results show that a flattened LPSC tends to stabilize the compressor (i.e it has a higher stalling flow coefficient).

In summary while the stall cell shape is insensitive to the changes in LPSC, the LPSC does appear to change the value of stalling flow coefficient by an amount that would be of concern to a compressor designer in terms of quantifying the stall margin. The characteristic near the peak appear to have a much larger impact on the value of stalling flow coefficient than the portion near the zero flow coefficient.

III. Flow Field Associated with A Localized Stall Cell

Computed flow field associated with the presence of a localized stall cell is presented to show that detailed flow structures recently measured in [4] can also be captured by the present computational model [1]. Ref [4] measured the detailed flow field around localized stall cell in a single stage compressor rig with an IGV, and two more stators at upstream and downstream of the compressor. Computed static pressure and axial velocity

field at the casing around a localized stall cell are shown in Fig.17 and Fig.18. The static pressure is high at the side that lead the stall cell, and low on the trailing side. The computed static pressure distribution is similar to what is observed in the measurements reported in [4]. The phenomena can be explained as a potential flow field around a blunt body (the blockage produced by a stall cell), around which the front side of the blunt body has a higher static pressure while the side of the blunt body has low static pressure.

IV. Stability modeling for high-speed compressors

The second part of the work under this grant is on the stability modeling for high-speed compressors. The goal is to implement this new methodology in a practical design-oriented environment. The major activities include (1) transfer of the modeling technology to researchers in NASA GRC, and (2) develop a procedure to extract source terms from three-dimensional Navier-Stokes solutions to enable the use of the Navier-Stokes solvers at NASA GRC to simulate compressor instability inception and development.

This portion of the grant activities involved technical collaboration between Dr. Gong of MIT and Dr. Chima of NASA GRC. The activities include (1) delivering the stability simulation codes for low-speed and high-speed compressors, and (2) transferring the methodology for incorporation into a Navier-Stokes solver at NASA GRC.

V. Summary

This report documents the work done during year 2000 on the multi-stage compressor stability modeling. The efforts include stability simulation of multi-stage compressor with various LSPCs, and the development of a procedure to extract body force from Reynolds-averaged Navier-Stokes solution for incorporating into an Euler code to represent the blade row. The key results are

(1) LSPC has a finite quantitative impact on stalling flow coefficient of a multi-stage compressor. The further study on the shape of LPSC would certainly be necessary to improve the capability of compressor instability prediction.

(2) The shape of the characteristic near the peak has the strongest impact on the stalling flow coefficient.

(3) The depth of the trough has relatively less impact on stalling flow coefficient,

(4) The size of localized stall cell is not sensitive to the shape of LSPC,

(5) The flow field at upstream of the stall cell is similar to the measurements in [4],

(6) A procedure to implement the computational model for use in design-oriented environment is under further development and refinement.

Reference

[1] Gong, Y., "A Computational Model for Rotating Stall and Inlet Distortions in Multistage Compressors," GTL Report #230, 1999

[2] Silkowski, P. D., "Measurements of Rotor Stalling in a Matched and a Mismatched Multistage Compressor," GTL Report #221, 1995

[3] Day, I. J. "Stall Inception in Axial Flow Compressors," ASME Journal of Turbomachinery, 1993, pp.1-9

[4] Inoue, M., etc., "Propagation of Multiple Short-Length-Scale Stall Cells in an Axial Compressor Rotor," ASME Journal of Turbomachinery, 2000, pp. 45-54

[5] Chima, R., personal communation.

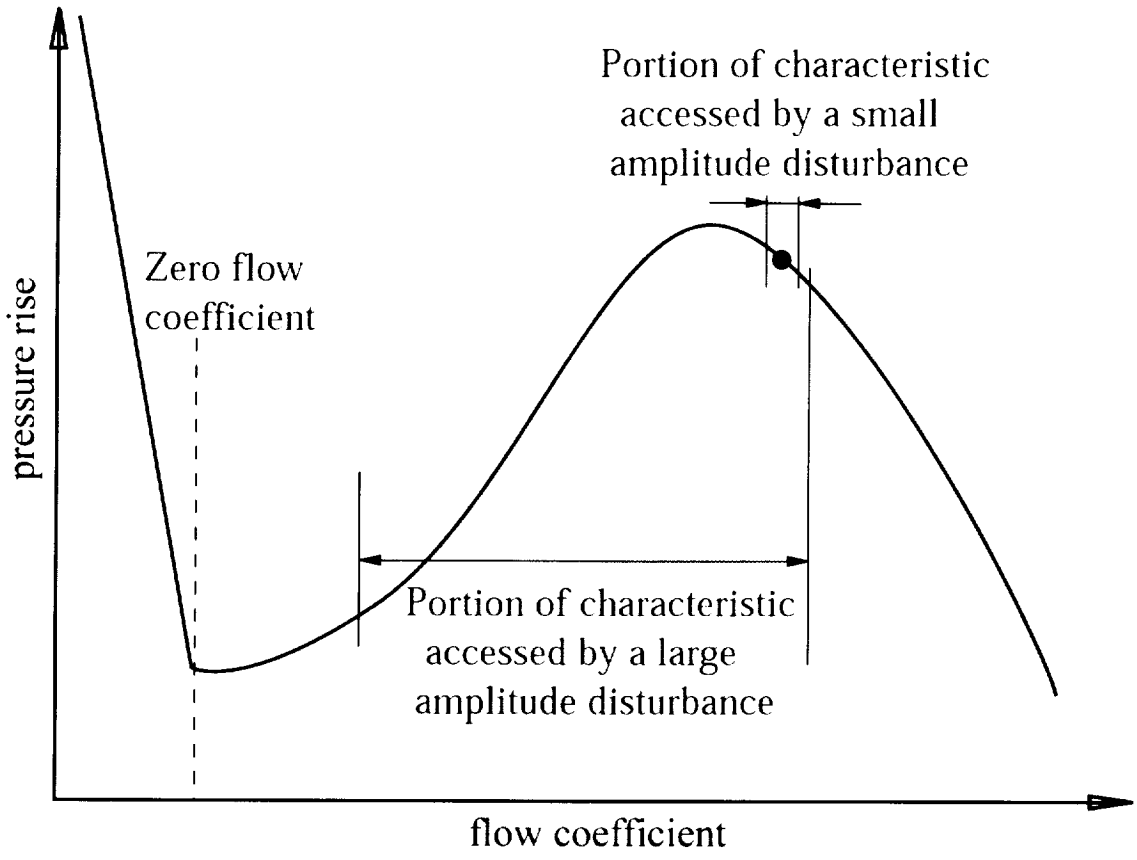

Figure 1 An illustration of the portion of pressure rise characteristic is accessed by a finite amplitude disturbance and a disturbance with infinitesimal amplitude.

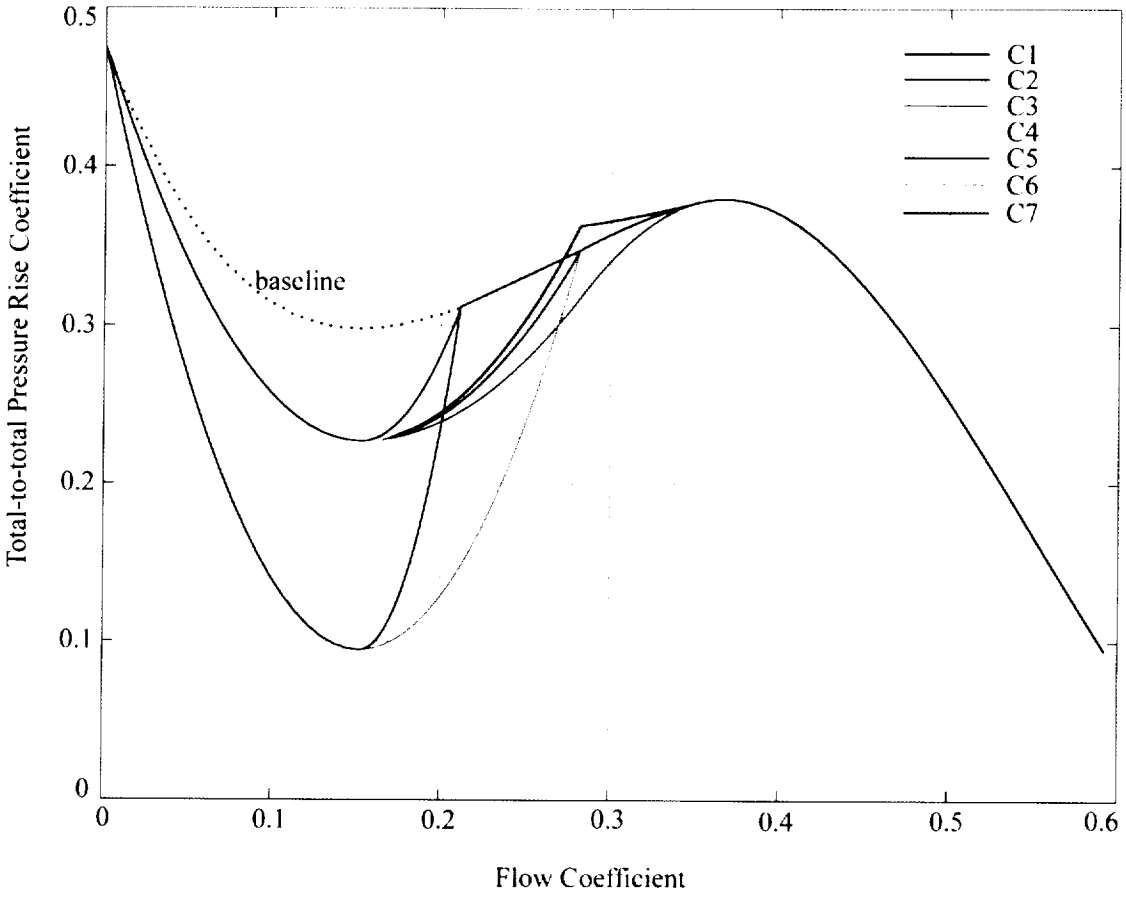

Figure 2 Eight Characteristics used in the investigation

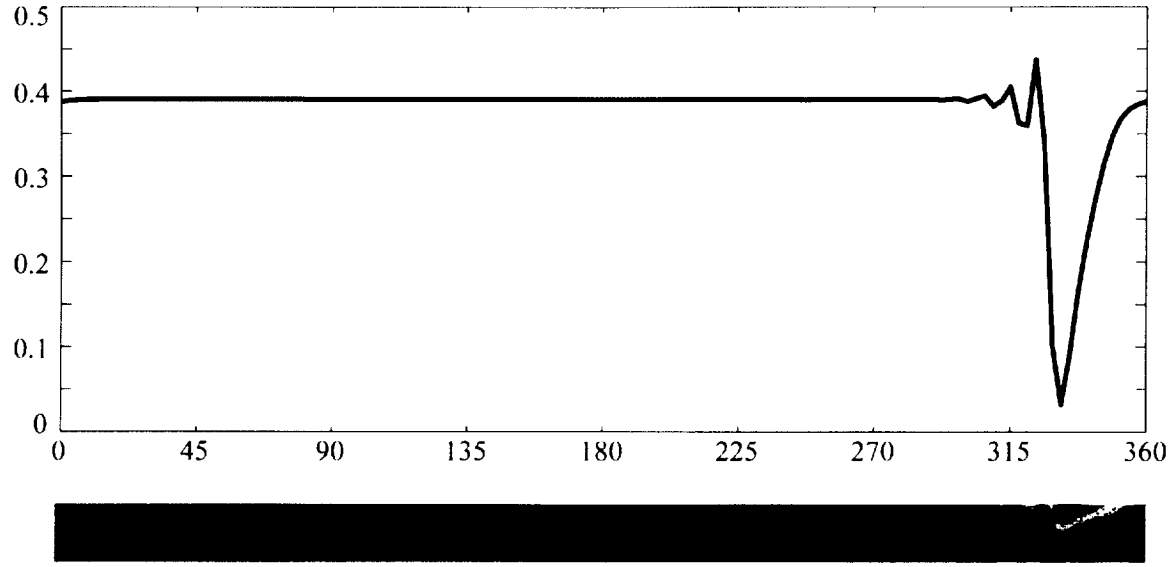

Figure 3 The flow coefficient distribution at rotor 1 exit (baseline). The top figure shows the flow coefficient around the annulus at the casing. The bottom plot shows the flow coefficient contours at the rotor 1 exit. The contours range from 0 (blue) to 0.5 (red).

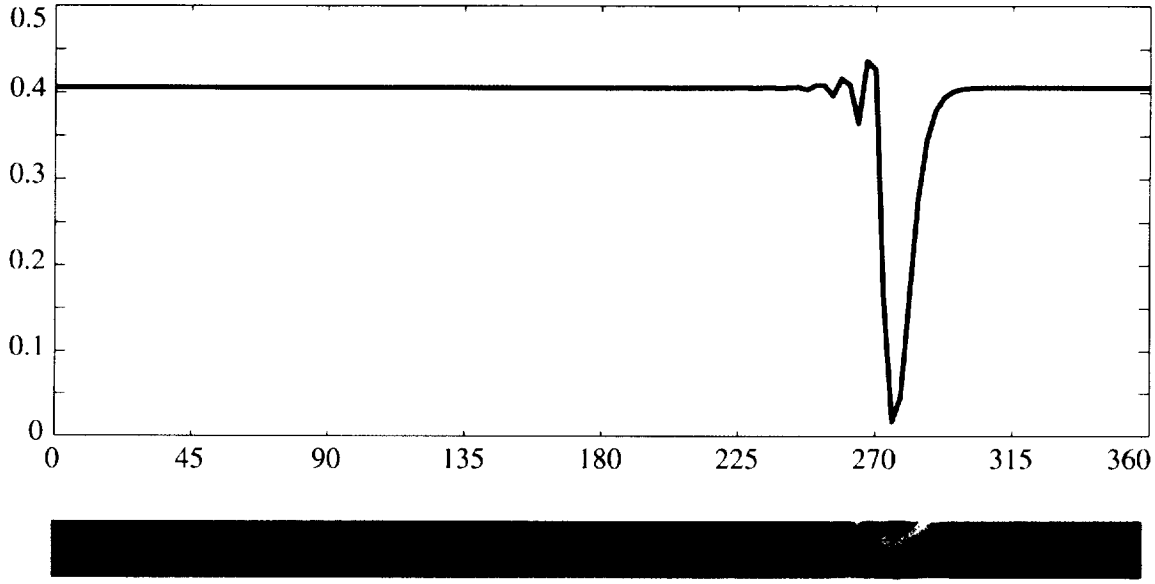

Figure 4 The flow coefficient distribution at rotor 1 exit (characteristic C1). The top figure shows the flow coefficient around the annulus at the casing. The bottom plot shows the flow coefficient contours at the rotor 1 exit. The contours range from 0 (blue) to 0.5 (red).

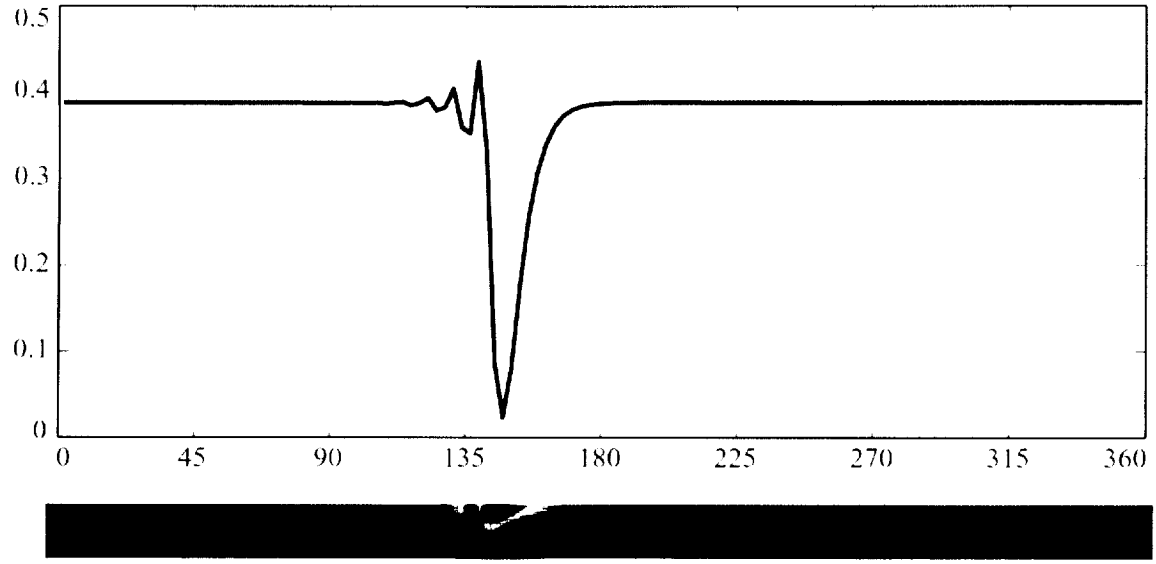

Figure 5 The flow coefficient distribution at rotor 1 exit (characteristic C2). The top figure shows the flow coefficient around the annulus at the casing. The bottom plot shows the flow coefficient contours at the rotor 1 exit. The contours range from 0 (blue) to 0.5 (red).

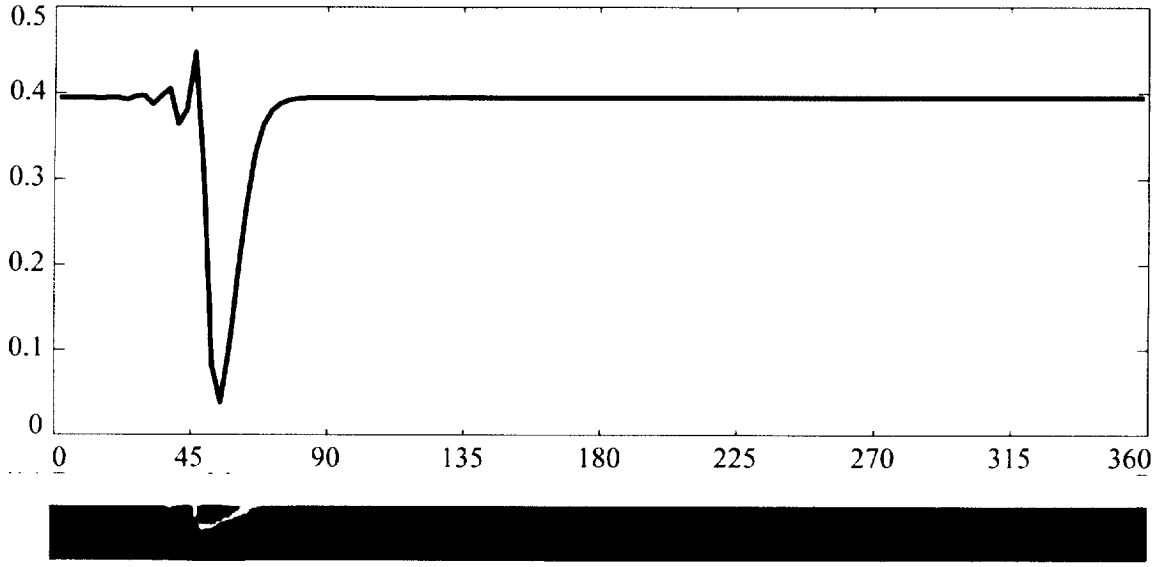

Figure 6 The flow coefficient distribution at rotor 1 exit (characteristic C3). The top figure shows the flow coefficient around the annulus at the casing. The bottom plot shows the flow coefficient contours at the rotor 1 exit. The contours range from 0 (blue) to 0.5 (red).

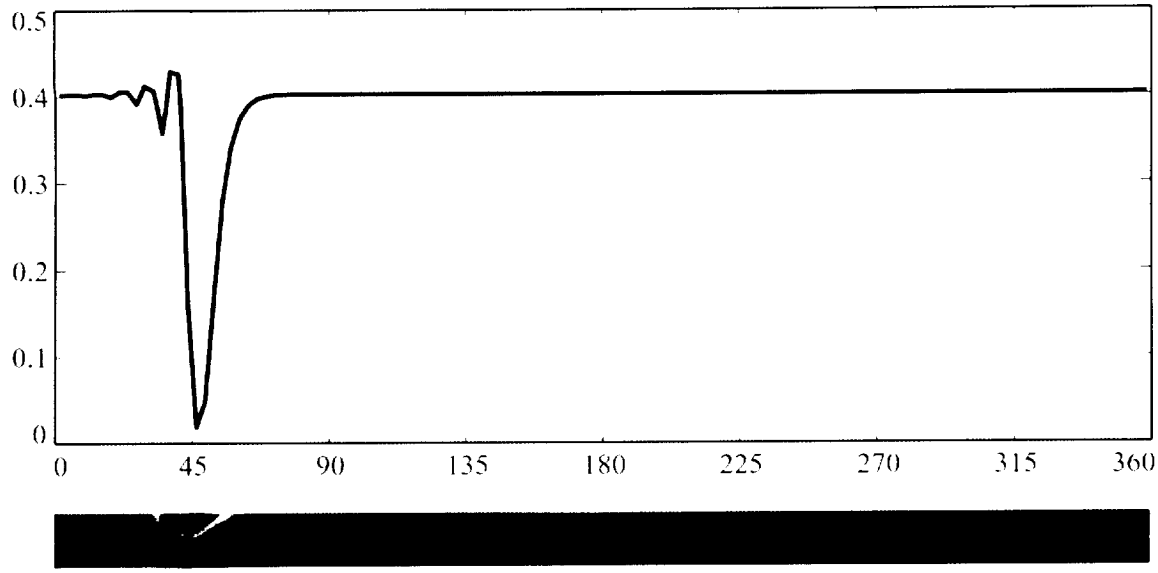

Figure 7 The flow coefficient distribution at rotor 1 exit (characteristic C4). The top figure shows the flow coefficient around the annulus at the casing. The bottom plot shows the flow coefficient contours at the rotor 1 exit. The contours range from 0 (blue) to 0.5 (red).

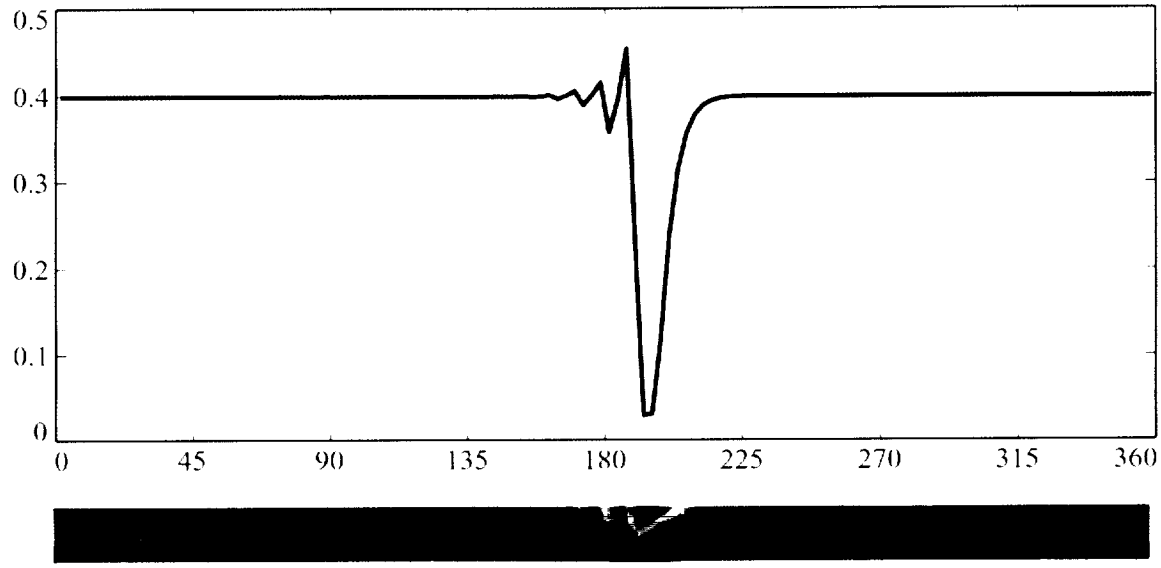

Figure 8 The flow coefficient distribution at rotor 1 exit (characteristic C5). The top figure shows the flow coefficient around the annulus at the casing. The bottom plot shows the flow coefficient contours at the rotor 1 exit. The contours range from 0 (blue) to 0.5 (red).

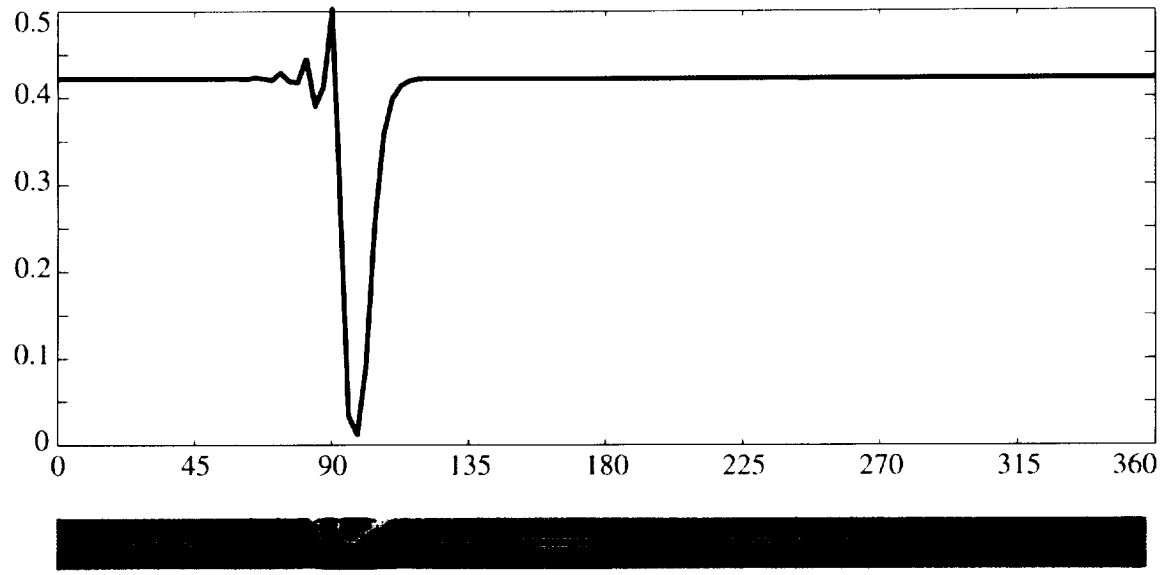

Figure 9 The flow coefficient distribution at rotor 1 exit (characteristic C6). The top figure shows the flow coefficient around the annulus at the casing. The bottom plot shows the flow coefficient contours at the rotor 1 exit. The contours range from 0 (blue) to 0.5 (red).

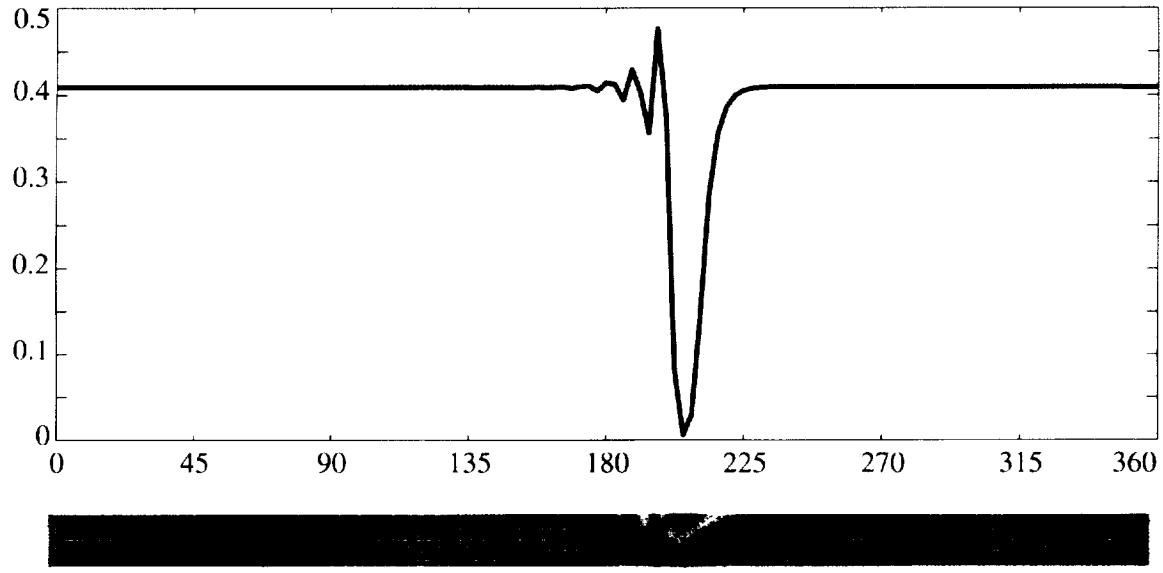

Figure 10 The flow coefficient distribution at rotor 1 exit (characteristic C7). The top figure shows the flow coefficient around the annulus at the casing. The bottom plot shows the flow coefficient contours at the rotor 1 exit. The contours range from 0 (blue) to 0.5 (red).

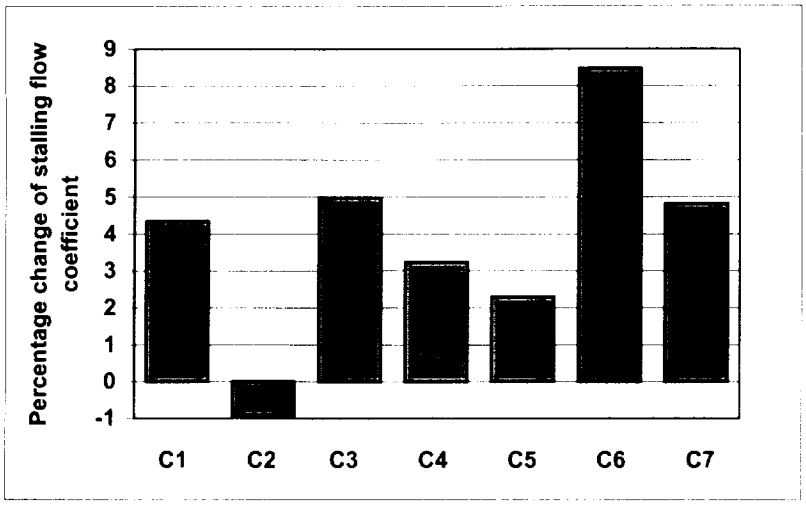

Figure 11 Change of stalling flow coefficients from the baseline for all seven characteristics used in the investigation

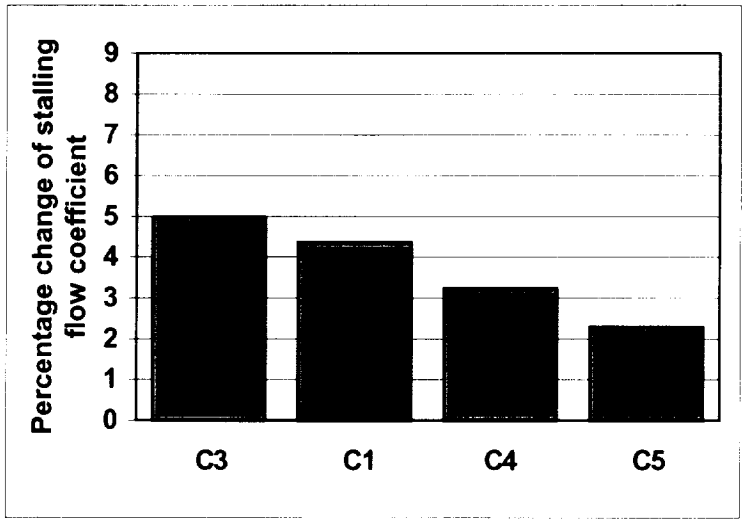

Figure 12 Change of stalling flow coefficient for the characteristic of C3, C1, C4, and C5, with the trough at a total-to-total pressure rise coefficient of 0.23

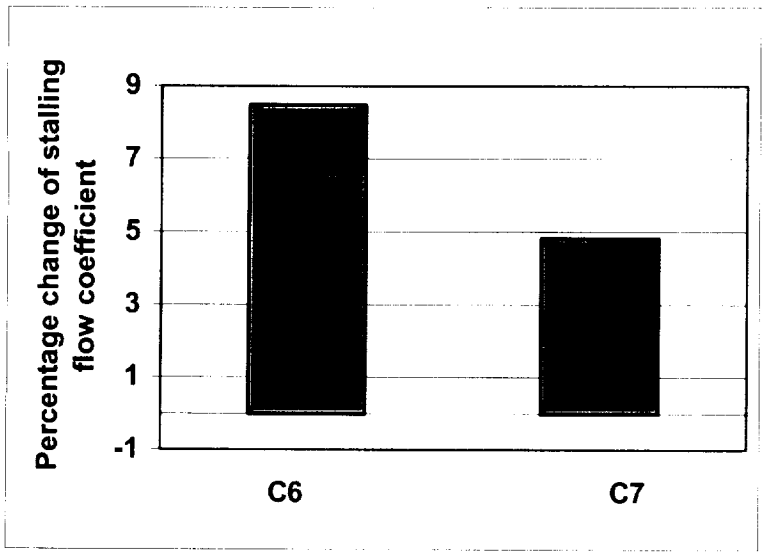

Figure 13 Change of stalling flow coefficient for the characteristic of C6, and C7 with the trough at a total-to-total pressure rise coefficient of 0.1.

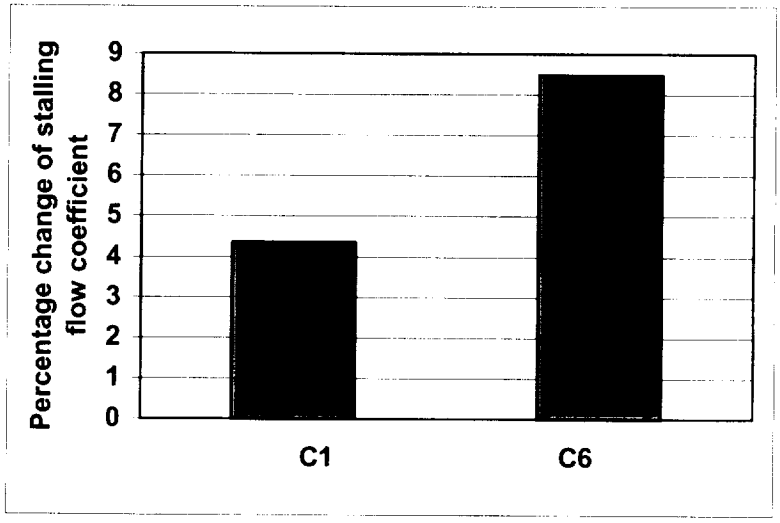

Figure 14 Change of stalling flow coefficient for the characteristic C1 and C6 with different trough depth and with steep drop occurring at flow coefficient of 0.28.

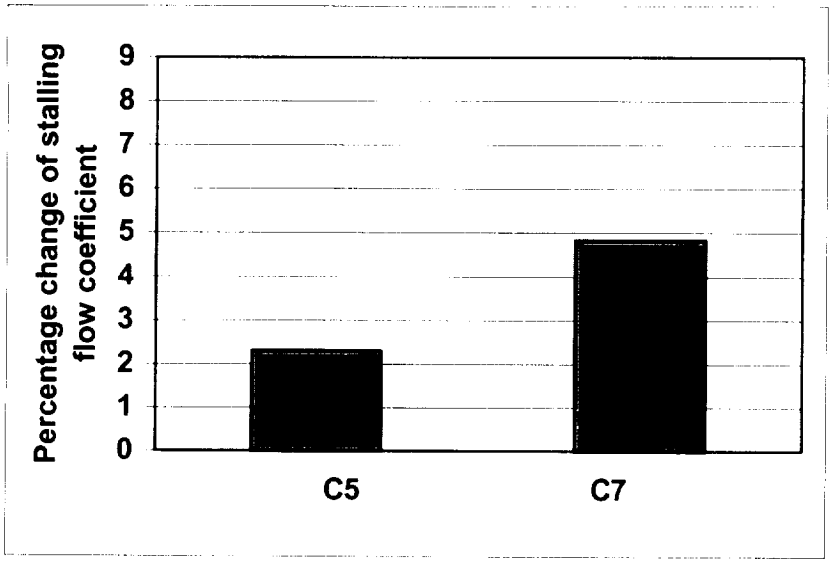

Figure 15 Change of stalling flow coefficient for the characteristic of C5 and C7 with different trough depth and with steep pressure drop occurring at flow coefficient of 0.21.

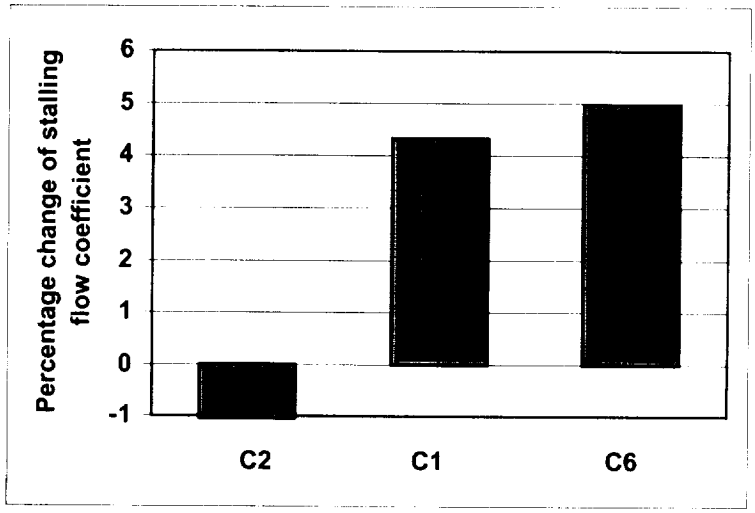

Figure 16 Change of stalling flow coefficients for the characteristic of C2, C1, and C6 with different slope near the peak, and with the trough at pressure rise coefficient of 0.23.

Figure 17 Casing static pressure distribution associated with a localized stall cell.

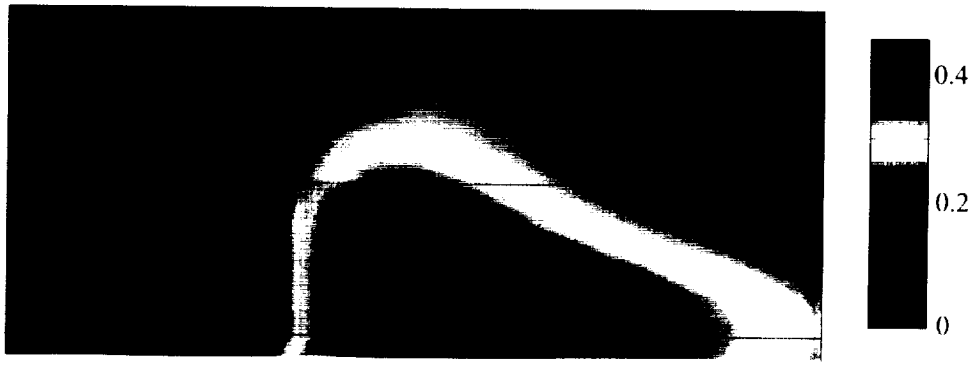

Figure 18 Casing flow coefficient distribution associated with a localized stall cell.